Phase Composition and Dynamical Studies of Lithium Iron Phosphate

Thesis by

Joanna L. Dodd

In Partial Fulfillment of the Requirements

for the Degree of

Doctor of Philosophy

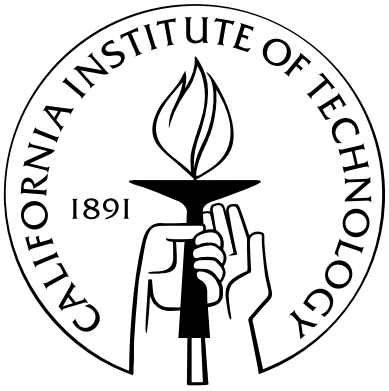

California Institute of Technology

Pasadena, California

2007

(Defended March 14, 2007)

To my parents, for all of their love and support through the years...

Acknowledgements

I would like to thank a number of people for their support throughout my Ph.D. studies. First of all, I would like to thank Brent Fultz, for all of his guidance and advise. I also thank Rachid Yazami for his guidance and insights as an electrochemist. I admire both of your enthusiasm for science, and hope to carry it on in my career.

I have had the privilege of working with many great people through the years in the Fultz lab. Channing, thank you for all of your help in the lab and also for your insights on energy and conversations about various topics. Itzhak, I enjoyed your time here at Caltech, and am glad I was able to learn from you in our high-pressure experiments. Sonjong, thanks for your help and your always-friendly demeanor. I would also like to express gratitude to those from our lab: Yvan, Yasunori, Olivier, Ryan, Tabitha, Jiao, Matt, Mike and Hongjin. Thanks for your help and for lively conversations. Other fellow students and friends: Anne, Mary Laura, Lisa, Houria, Angelique, Rebecca, Max, Peter, I have always enjoyed the lunch times and other fun times, and I hope to keep in touch. You have all made my graduate studies more enjoyable!

I would like to thank a number of collaborators and colleagues, including Atsuo Yamada and Shin-ichi Nishimura from Tokyo Institute of Technology, and also Khalil Amine and Ilias Belharouak from Argonne National Lab. I also thank Mikito Nagata and Hisashi Tsukamoto from Quallion LLC for their support while I began my Ph.D. at Caltech. Thank you also to the US Department of Energy for financial support.

Lastly, I would like to express my gratitude to my family, for their support during all of these years. Mom and Dad, thank you for your love and support! Emily, Cecile, and Li, I look forward to many more opportunities to hang out, with no more classes or thesis writing to do! Finally, Jason, thank you for your constant support these past years.

Abstract

The olivine phase of lithium iron phosphate (Li_xFePO_4) is a promising cathode material for lithium-ion batteries. Some of its advantages are that it is nontoxic, highly stable, and inexpensive, but its low intrinsic electrical conductivity is a major disadvantage. Li_xFePO_4 has generally been described as a two-phase system as lithium is removed from or inserted into the material. However, the mechanism of lithium removal and the system's phase composition is still not fully understood, and is an area of interest.

The two low-temperature phases, heterosite and triphylite, have previously been shown to transform to a single-phase disordered solid solution at temperatures above 200 °C. Here, the phase diagram for Li_xFePO_4 has been determined for different lithium concentrations and temperatures. This disordered phase is stable at relatively low temperatures. The proposed phase diagram resembles a eutectoid system, with eutectoid point at around x = 0.6 and 200 °C. The kinetics of mixing and unmixing transformations, including the hysteresis between heating and cooling, will be shown. The enthalpy of this transition is at least 700 J/mol. Further thermostability studies of the material up to temperatures of 800 °C will also be discussed.

Solid solution regions have also been indicated near the end compositions of $x = 0$ and 1 at room temperature. Measurements of the entropy ($\Delta S(x)$) and enthalpy ($\Delta H(x)$) of lithiation were performed, indicating the ranges of solid solution regions to be $x < 0.05$ and $x > 0.85$. In addition, the entropy of lithiation in between ($0.05 < x < 0.85$) changes gradually with x. This is unexpected, since $\Delta S(x)$ should be constant in a two-phase region. There are several alternatives which could be causing this result. Further clarification of this topic could give additional information about the phase transformation occurring as $LiFePO_4$ is delithiated.

The topic of dynamics in Li_xFePO_4 is also very relevant, especially since this material is now touted as an important high-rate capability cathode. The electronic and ionic conductivity of the new disordered solid-solution phase has generated widespread interest. The local electronic structure around iron ions in $Li_{0.6}FePO_4$ was studied by ^{57}Fe Mössbauer spectrometry at temperatures from 25 to 240 °C. The equilibrium two-phase triphylite plus heterosite material was compared to a disordered solid solution that was obtained by quenching from a high temperature. Substantial electronic relaxations were found in the disordered solid solution compared to the two-phase material at temperatures of 130 °C and above. Fluctuations in the electric field gradient and the isomer shift showed activation energies of 335 ± 25 meV and 600 ± 100 meV, respectively. It is suggested that these spectral relaxations are caused by the motions of Li^+ ions. The activation energies from the isomer shift can be related to the material conductivity, giving values of 10^{-6} to 10^{-4} S/cm; 3 to 5 orders of magnitude higher than the measured value of 10^{-9} for fully lithiated $LiFePO_4$. A slight relaxation at 180 °C in 10% of the two-phase material can be attributed to defects in the heterosite and triphylite phases. Overall, the disordered solid-solution phase shows faster electronic dynamics than the two-phase material.

Additional studies on the dynamics of the disordered solid solution, along with attempts to stabilize this phase at lower temperatures, should be a topic of further work.

Contents

List of Figures

List of Tables

Chapter 1

Lithium Battery Overview

1.1 Background on Batteries

With the development of new electronic devices, our society has become more and more dependent on electricity, and with portable devices comes the need for portable electricity. With their widespread uses, batteries have become a staple in meeting these needs for portable electricity. Batteries are devices which convert the energy released by spontaneous chemical reactions to electrical work. A battery is composed of one or more electrochemical cells that are connected in series or in parallel to provide a required voltage and capacity.

Battery applications include portable electronics, such as cell phones, laptop computers, or MP3 players such as the iPod. These applications require a high energy density, since consumers desire smaller, lighter, longer-running devices. The development of new medical devices, such as neurostimulation and cardiovascular devices, requires an extremely safe, reliable battery. Batteries for implantable devices require operation at 37 °C, as well as good cycle life and calendar life, so the system can last for at least ten years. Satellites are another battery application requiring high reliability and long life. Power tools require high power capability. The development of batteries for either fully electric or hybrid electric vehicles is also a hot topic due to environmental concerns. Electric vehicles can reduce our reliance on oil, and reduce polluting emissions. All in all, the applications for batteries are very diverse.

There are two categories of battery cells: primary and secondary. Primary batteries are non-rechargeable, for a single usage, while secondary batteries are rechargeable, and can be

reused many times. Different cell chemistries are preferred, depending upon the application, but for most of the applications mentioned above, especially for rechargeable battery applications, lithium-ion batteries are becoming the system of choice. The development of lithium-ion batteries has enabled smaller, lighter devices, due to lithium's high energy density and light weight. The low atomic mass of lithium metal results in a specific capacity of 3860 mAh/g. In addition, lithium batteries use a non-aqueous electrolyte, allowing higher voltages than aqueous electrolyte-based battery systems. Aqueous systems are limited to voltages lower than 1.23 V, due to the thermodynamic limitation of water at 25 °C. The voltages of lithium batteries are also much higher than those of lead-acid and nickel-metal hydride cells because lithium is the most electropositive element found in nature [1]. Table 1.1 gives a comparison of several major rechargeable battery systems.

Battery Type	Anode	Cathode	Nominal Voltage (V)	Specific Energy (Wh/kg)	Energy Density (Wh/L)
Lead-acid	Pb	PbO_2	2.0	35	70
Nickel-cadmium	Cd	Ni oxide	1.2	35	100
Nickel-hydrogen	H_2	Ni oxide	1.2	55	60
Nickel-metal hydride	MH	Ni oxide	1.2	75	240
Silver-zinc	Zn	AgO	1.5	105	180
Lithium-ion	Li_xC_6	$Li_{1-x}CoO_2$	4.1	150	400

Table 1.1: Summary of different battery systems, indicating anodes and cathodes as well as voltage and powers for practical batteries [2].

1.2 Electrochemical Cells

1.2.1 Summary

An electrochemical cell converts chemical energy into electrical energy through a controlled exothermic chemical reaction. The elements of an electrochemical cell include a cathode, anode, separator, and electrolyte. The cathode, also referred to as the positive electrode, is an oxidizing electrode, which accepts electrons and is reduced during the electrochemical discharge reaction. The anode, or negative electrode, is a reducing electrode, which gives up electrons and is oxidized during the same reaction. These processes occur during discharge

of the cell, when electrical energy is generated by the cell (see figure 1.1). During charging of a cell, the opposite occurs; the cathode is oxidized and the anode is reduced.

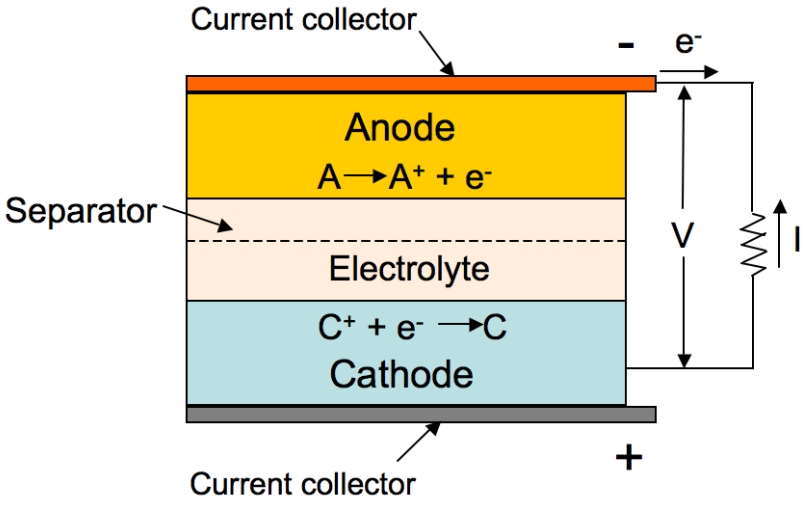

Figure 1.1: Elements of an electrochemical cell, shown during discharge.

1.2.2 Thermodynamic principles

The first law of thermodynamics requires a conservation of energy. Thus, $\Delta U = \Delta Q + \Delta W$ (where Q and W are heat and work, respectively). With W_e the electrical work done by an electrochemical cell, and S and V the entropy and volume, we can express ΔU as:

$$\Delta U = T\Delta S - P\Delta V + W_e. \tag{1.1}$$

We can see that W_e is directly related to the Gibbs free energy, ΔG, since ΔG is the difference between the reaction enthalpy, $\Delta H = \Delta U + P\Delta V$ and the entropic term, $T\Delta S$:

$$W_e = \Delta U - T\Delta S + P\Delta V = \Delta H - T\Delta S = \Delta G. \tag{1.2}$$

By electrostatics, electrochemical work is related to the cell potential, ΔE_0, by the following expression:

$$W_e = -nF\Delta E_0. \tag{1.3}$$

Therefore, the cell potential is related to the Gibbs free energy of the system by the expression:

$$\Delta E_0 = \frac{-\Delta G}{nF}, \tag{1.4}$$

where F is Faraday's constant, the number of Coulombs in a mole of electrons (F = 96,485 C mol^{-1} = 26.8 Ah mol^{-1}), and n is the number of electrons exchanged in the reaction (for lithium cells, $n = 1$).

The standard potential of a cell (ΔE_0) is determined by the thermodynamics of the system by its relationship to ΔG. The free energy is related to the chemical potentials μ of the reactants i, as

$$\Delta G = \sum_i \nu_i \mu_i, \tag{1.5}$$

where ν_i are coefficients of the ith reactants in the electrochemical reaction. For substances formed, ν is positive, and for substances consumed ν is negative. Since

$$\Delta E_0 = -\frac{1}{nF} \sum_i \nu_i \mu_i, \tag{1.6}$$

the cell voltage is thus obtained from the chemical potentials of the reactants in the cell.

1.3 Lithium-Ion Cells

In a lithium-ion cell, during discharge lithium ions are deintercalated from the anode material and transported through an electrolyte across an ionically-permeable membrane, the separator. The lithium is reinserted into the cathode material. Electrons are transferred through an external circuit, delivering electric energy to the device load. During charge, current is forced in the opposite direction, and lithium is extracted from the cathode and intercalated into the anode material.

The cathode and anode are usually in intimate contact with current collectors, which are usually thin foils with high electrical conductivity, and which can withstand the potentials of the anode and cathode of the cells. A common current collector for lithium-ion

cathodes is aluminum; for anodes it is copper. The electrolyte used in lithium-ion cells is an organic solvent (common solvents include ethylene carbonate, diethylene carbonate, dimethyl carbonate and propylene carbonate) with a lithium salt, such as $LiPF_6$, $LiClO_4$, or lithium bis(oxalato)borate (LiBOB). The separator is usually a microporous film composed of polyethylene or polypropylene or a combination of the two. It is important that the separator be ionically conductive but electrically insulating. For lithium-ion cells, it is also important that the separator has safety features. A common safety feature is a shutdown of the pores through separator melting if excessive heat is generated in the battery (at around 120 °C). The closing of separator pores is designed to slow down short circuits and avoid thermal runaway of the cell and battery rupture.

For rechargeable cells, to ensure a reversible reaction it is important that reactions involving charge and discharge of the cell do not require large changes in intercalation host materials. Intercalation reactions are topotactic. As a result, the structure of the host is changed only by atomic displacement, with no diffusive rearrangement of host atoms. Numerous cathode and anode materials have been discovered, which enable lithium intercalation or insertion with minimal structural changes. Typical electrodes have a layered structure with open channels for diffusion and storage of the lithium. Cathode and anode materials will be discussed in more detail in sections 1.3.1 and 1.3.2.

1.3.1 Cathode material overview

Work on the first rechargeable lithium battery was published by Whittingham in 1976 [3]. He showed the reversible intercalation of lithium in a TiS_2 cathode. Several families of cathode materials have been developed for lithium batteries since then. The most common material at this time still remains $LiCoO_2$, which was first studied in Goodenough's laboratory in 1980 [4]. Due to the high cost of cobalt, and also the instability of Li_xCoO_2 for $x < 0.5$, several other $LiMO_2$-type cathodes (where M = Co, Ni, Mn, or V) have also been developed. Many different combinations of transition metals have been tested. Two promising varieties include $LiNi_{0.80}Co_{0.15}Al_{0.05}O_2$ and $LiNi_{0.33}Co_{0.33}Mn_{0.33}O_2$, with both showing good cycle characteristics, but the latter having better safety characteristics [5]. The manganese spinel system, $LiMn_2O_4$, has also been thoroughly studied due to is safety

characteristics, high-rate capabilities and low cost. It is of interest as a possible high-power battery for hybrid electric vehicles [6].

Olivine-type cathodes ($LiMPO_4$, with M = Fe, Mn, Co) are also of major interest, especially $LiFePO_4$, due to its high safety, and environmental and good cycle life characteristics. $LiFePO_4$ is also a cheaper alternative to $LiCoO_2$ due to its substitution of cobalt with iron. This material is the focus of this thesis, so a more detailed overview on its structure and operation is given in chapter 2.

Another phosphate material which could become more popular in the future is monoclinic $Li_3V_2(PO_4)_3$. Two moles per functional unit can be reversibly removed and inserted, giving a capacity of 130 mAh/g at an average voltage of 3.8 V vs. Li/Li^+. The extraction of the last lithium takes place at 4.6 V, and it appears to be energetically unfavorable, exhibiting a large overvoltage. However, it is possible to remove all three Li atoms, giving 175 mAh/g. If the kinetics and cyclability of this reaction could be improved, this could be a promising cathode [7].

Table 1.2 gives a summary of cathode types, along with specific capacities and energy densities.

Material	Average E (V)	Reversible Range x	Capacity (mAh/g)	Energy Density (Wh/kg)
Li_xCoO_2 [8]	4.0	$0.5 < x < 1.0$	137	548
Li_xNiO_2 [9]	3.8	$0.5 \leq x \leq 1.0$	137	521
$Li_xNi_{0.80}Co_{0.20}O_2$ [10]	3.9	$0.4 \leq x \leq 1.0$	164	640
$Li_xNi_{0.33}Co_{0.33}Mn_{0.33}O_2$ [11]	3.8	$0.3 \leq x \leq 1.0$	200	760
$Li_xMn_2O_4$ [12]	3.0	$1.0 \leq x \leq 2.0$	143	428
Li_xFePO_4 [13]	3.5	$0.0 \leq x \leq 1.0$	170	595
$Li_xV_2(PO_4)_3$ [7]	3.8	$0.0 \leq x \leq 3.0$	175	665

Table 1.2: Cathode materials, with specific capacities and energy densities

1.3.2 Anode material overview

Lithium metal was the first anode used in a lithium battery, and for good reason; its specific capacity is 3860 mAh/g. However, in rechargeable, liquid electrolyte batteries, metallic lithium is not a safe choice. Lithium is chemically reactive with the non-aqueous electrolyte. This reactivity results in a passivating layer on the metallic lithium anode,

which leads to a non-uniform plating of lithium during charging. Thus, lithium dendrites can form and can grow through the separator, causing the risk of cell failure due to short circuiting [14].

Today, the most widely used anode in lithium-ion batteries is graphitic carbon. Graphite was found to reversibly intercalate lithium in a polymer electrolyte in 1983 [15]. Graphite is a layered structure, allowing lithium intercalation between the layers with a theoretical specific capacity of 372 mAh/g corresponding to a LiC_6 stoichiometry.

A spinel material, $Li_4Ti_5O_{12}$ is under consideration for an anode in high-power cells, since its charging potential is around 1.55 V vs. lithium, so there is no danger in lithium metal deposition, which could happen when cycling graphitic anodes at high rates. However, use of this material as an anode would reduce the overall cell voltage, and the capacity of this material is only 160 mAh/g [16].

Other candidate anodes include lithium binary alloys (Li-Al, Li-Si, Li-Sn, Li-Ge), which all have higher specific capacities than graphite (Li-Si, at $Li_{22}Si_5$ has a capacity 4200 mAh/g and Li-Ge at $Li_{22}Ge_5$ has a capacity 1600 mAh/g). However, these compounds undergo crystallographic phase changes and also large volumetric expansion when alloyed with lithium. Therefore, only nanosized particles or films have been successful, and cycle life has been limited. Graetz et al. developed amorphous nanosized thin films, having 2000 mAh/g and 1700 mAh/g, for Si and Ge films, respectively, for over 50 cycles [17, 18]. However, extended cycling has not been studied sufficiently.

Composites of graphite and nano-Si can result in good cycle life, while also maintaining a relatively high capacity. For example, Holzapfel et al. were able to cycle a 20% nano-silicon/80% graphite composite with little capacity fade with a capacity of around 1000 mAh/g for over 100 cycles [19]. In such a composite, the graphite matrix serves as a structural support for the nano-Si. This may be a good compromise to increasing the anode capacity while still retaining good cycle life characteristics.

Chapter 2

Overview of $LiFePO_4$

2.1 Overall Characteristics

Lithium iron phosphate ($LiFePO_4$) is an olivine-type material with the triphylite structure, which is a phosphate mineral found in the earth. However, it had not been investigated electrochemically until Padhi et al. did so in 1997 [13]. They were able to electrochemically extract and insert lithium into the lattice, achieving 100 to 110 mAh/g capacity, compared with the theoretical value of 170 mAh/g. They showed that it was a promising electrode, but that it would require efforts to improve on rate capability and to approach the theoretical capacity. This capacity corresponds to one Li mole insertion and deinsertion, according to the equation:

$$LiFePO_4 \longleftrightarrow Li_xFePO_4 + (1-x)Li^+ + (1-x)e^-, \quad 0 < x < 1, \tag{2.1}$$

where at room temperature Li_xFePO_4 is composed of two phases, a lithiated triphylite phase, $LiFePO_4$, and a delithiated heterosite phase, $FePO_4$:

$$Li_xFePO_4 \equiv xLiFePO_4 + (1-x)FePO_4. \tag{2.2}$$

$LiFePO_4$ cycles versus lithium at a potential of 3.4 V, which is slightly lower than metal oxide $LiMO_2$ cathode materials (M = Co, Ni, Mn), but is still a reasonably high potential. Other homologous lithium transition metal phosphates, $LiMPO_4$ (M = Co, Ni, Mn, Cu) are also possible cathode materials for lithium-ion batteries. Both $LiMnPO_4$ and $LiCoPO_4$ have

higher potentials vs. lithium (4.1 V and 4.8 V, respectively) [13, 20], which could result in higher energy densities than $LiFePO_4$, but neither has been electrochemically cycled with as high specific capacity as $LiFePO_4$ electrodes due to poorer rate capabilities.

$LiCoO_2$ is still the most commonly used cathode material in lithium-ion batteries. Advantages of $LiFePO_4$ as a cathode material include it being environmentally benign, nontoxic, and also inexpensive. The replacement of Co or Ni by Fe is especially advantageous, since Fe is a much more common element, and is therefore comparatively inexpensive. In fact, the growing number of lithium batteries used in the world has itself increased the demand for Co and its price.

$LiFePO_4$ is also especially favorable for its safety and thermostability characteristics. Differential scanning calorimetry (DSC) experiments of charged Li_xFePO_4 electrodes in the presence of electrolyte showed much smaller exothermic reactions, compared to a Li_xCoO_2 electrode charged to a similar specific capacity of 170 mAh/g [21, 22, 23]. The onsets of these exotherms were between 250 and 350 °C, with the variation between experiments possibly attributable to different electrolyte compositions. In any case, the reduced heat evolution from $LiFePO_4$ upon heating, compared with the abrupt and much larger heat generation from metal oxide cathodes such as $LiCoO_2$, $LiNiO_2$ and $LiMn_2O_4$ [24], suggests that $LiFePO_4$ would be a much safer cathode material. This is especially important for larger batteries, or even for smaller batteries designed for medical applications where safety is of utmost importance.

The stability of $Li/LiFePO_4$ cells at elevated temperatures also makes the $LiFePO_4$ cathode desirable for high temperature applications, such as implantable medical applications (37 °C) or even hybrid electric vehicle applications (up to 60 °C). The thermostability of Li_xFePO_4 phases is a topic covered in this work (see chapter 5). In fact, both a higher reversible capacity and a higher rate capability can be achieved at 60 °C compared to room temperature [21, 25]. This is due to higher lithium mobility and also higher electrical conductivity in the $LiFePO_4$ crystals at higher temperatures, allowing increased specific capacity.

At ambient temperature and temperatures of 60 °C and above, $LiFePO_4$ shows capacity retention characteristics superior to $LiMn_2O_4$ in $LiPF_6$-based electrolytes, perhaps owing

to a much lower Fe dissolution compared to Mn dissolution [26, 27]. It has been shown that in electrochemical cells the $LiFePO_4$ electrode material works well at 60 °C, but may have a slightly higher capacity fade at this operating temperature [25]. Actually, the capacity fade of this cathode depends on the amounts of impurities in the material, including Fe phosphites, and also impurities in the electrolyte. Iron dissolution can be an issue, especially at elevated temperatures in the presence of water or acidic/protic contaminants [28, 29]. Choice of electrolyte salt can be important in reducing the acidity of the electrolyte, with $LiB(C_2O_4)_2$ or $LiClO_4$ as better options than $LiPF_6$, for example. When in the presence impurities, when $LiFePO_4$ is cycled in a cell vs. graphite, dissolved Fe plates onto the graphite surface, causing an impedance rise for the graphite electrode and cell capacity fade [29]. Therefore, in elevated-temperature applications, the purity of the electrode and electrolyte, along with electrolyte salt choice, are crucial. Since car manufacturers hold 60 °C as a specification for battery temperature for all subsystems in their cars, $LiFePO_4$ is a possible candidate for use in hybrid-electric or electric vehicles. Cycling of $LiFePO_4$ cathodes at a 20C rate has also been reported [30], showing the promise of $LiFePO_4$ as a high power cathode.

2.2 Atomic Structure

$LiFePO_4$ is known to cycle as a two-phase system, with triphylite as the lithiated phase and heterosite as the delithiated phase. Both phases are olivine-type orthorhombic structures, with the Pnma space group, with the differences being the presence of lithium chains in the triphylite structure, which change the unit cell of the crystal. Figure 2.1 shows unit cells of the two structures.

As lithium is extracted from triphylite ($LiFePO_4$), the second phase, heterosite ($FePO_4$) is formed. Triphylite contracts by approximately 7% in volume as heterosite is formed. The lattice parameters for each phase are given in table 2.1.

The two-phase nature of the partially lithiated material is shown by both x-ray diffractometry (XRD) and Mössbauer spectrometry. Andersson, et al. performed early measurements by both XRD and Mössbauer spectrometry of $LiFePO_4$ at different states of charge

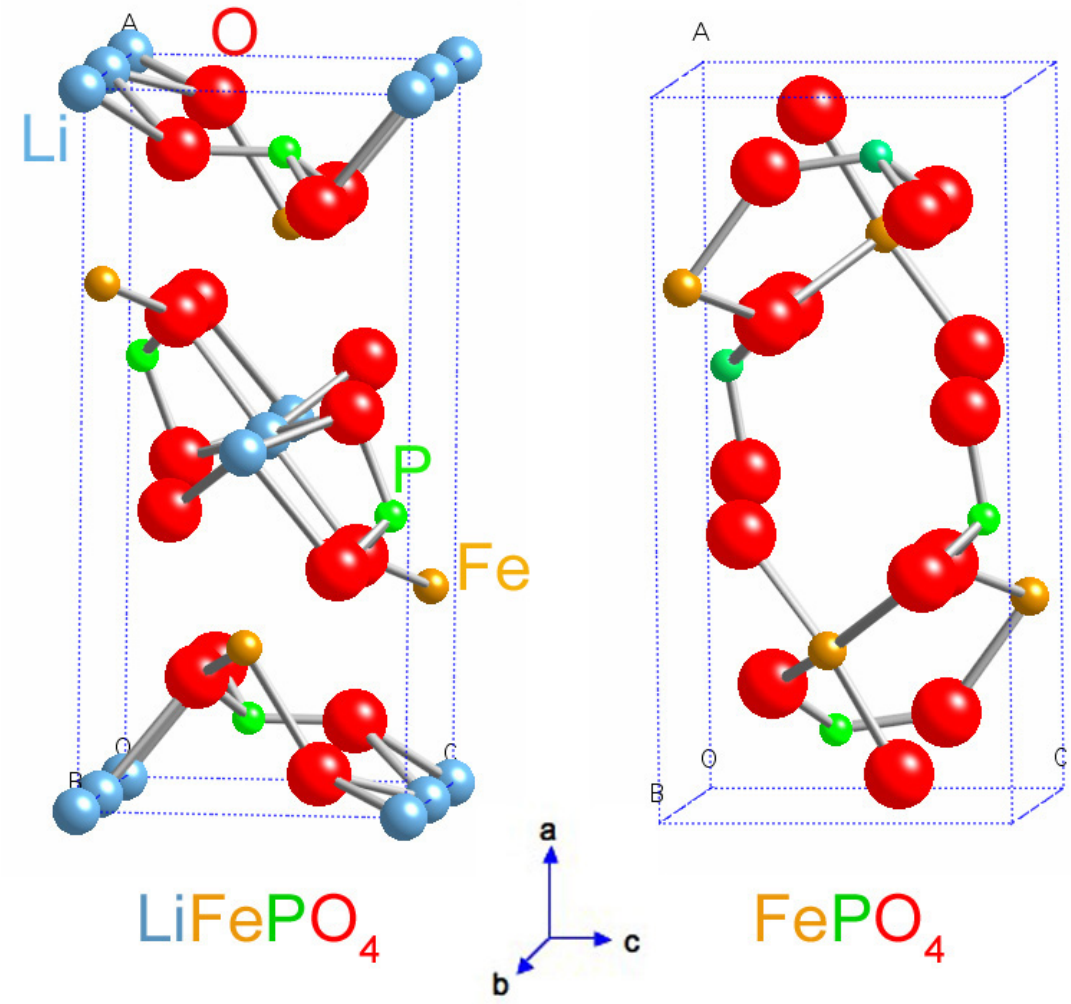

Figure 2.1: Triphylite ($LiFePO_4$) and heterosite ($FePO_4$) structures.

Phase	Triphylite ($LiFePO_4$) [31]	Heterosite ($FePO_4$) [31]	Triphylite ($LiFePO_4$) this work	Heterosite ($FePO_4$) this work
a (Å)	10.329	9.814	10.335	9.825
b (Å)	6.007	5.789	6.011	5.796
c (Å)	4.691	4.782	4.695	4.788
Volume (Å^3)	291.1	271.7	291.6	272.6

Table 2.1: Lattice parameters and volume of unit cell for triphylite and heterosite phases as determined by Rietveld refinement, by Andersson et al. [31] and in this work.

[31]. Their results were confirmed in this work. Figure 2.2 shows a series of XRD patterns for materials with different amounts of lithiation, between $x = 0$ and $x = 1$. The intensities of heterosite phase peaks gradually increase as lithium is extracted from the material.

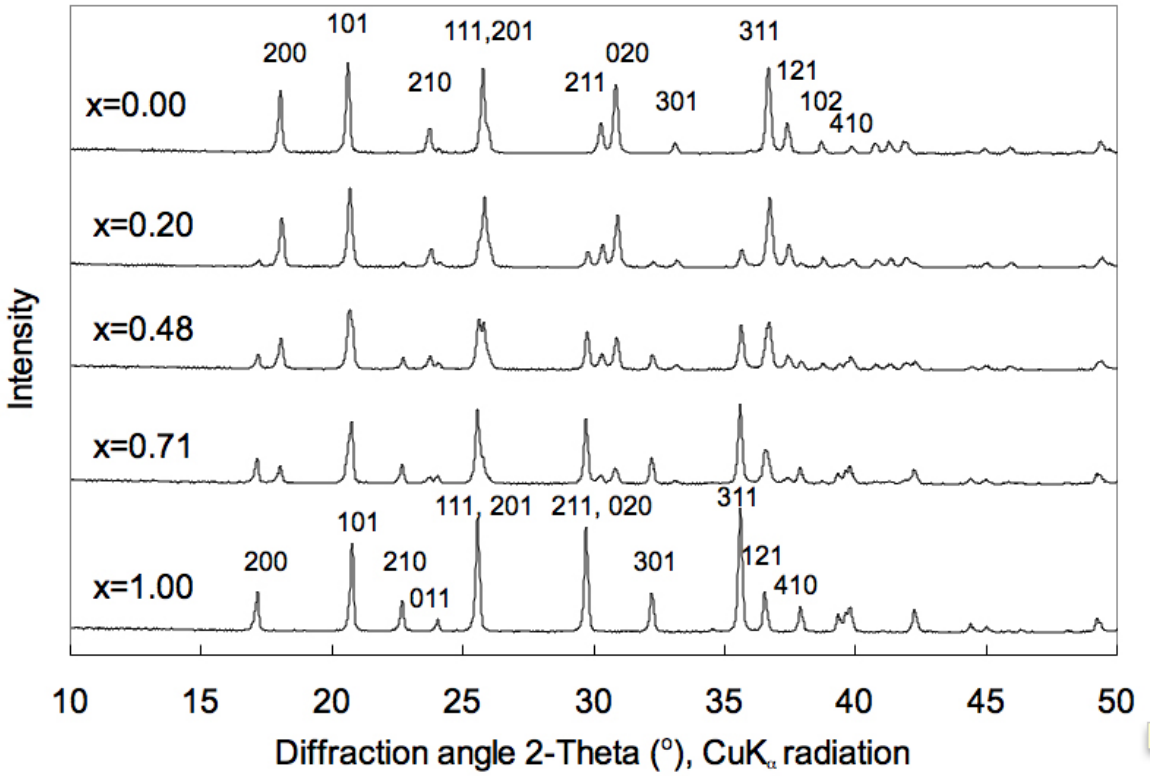

Figure 2.2: XRD patterns for five samples, each with a different amount of lithiation, x, in Li_xFePO_4. The values x were computed by Rietveld refinement of the XRD patterns. The $x = 1.00$ pattern matches the triphylite Pnma orthorhombic structure, while the $x = 0.00$ pattern matches the heterosite structure. For x between 0 and 1, a combination of both triphylite and heterosite is evident.

Mössbauer spectrometry is a method to probe the electronic structure near the Fe nucleus. From such measurements, the percentage of Fe^{2+} and Fe^{3+} in the material can be determined. The Mössbauer spectra of several samples of $LiFePO_4$ are shown in figure 2.3.

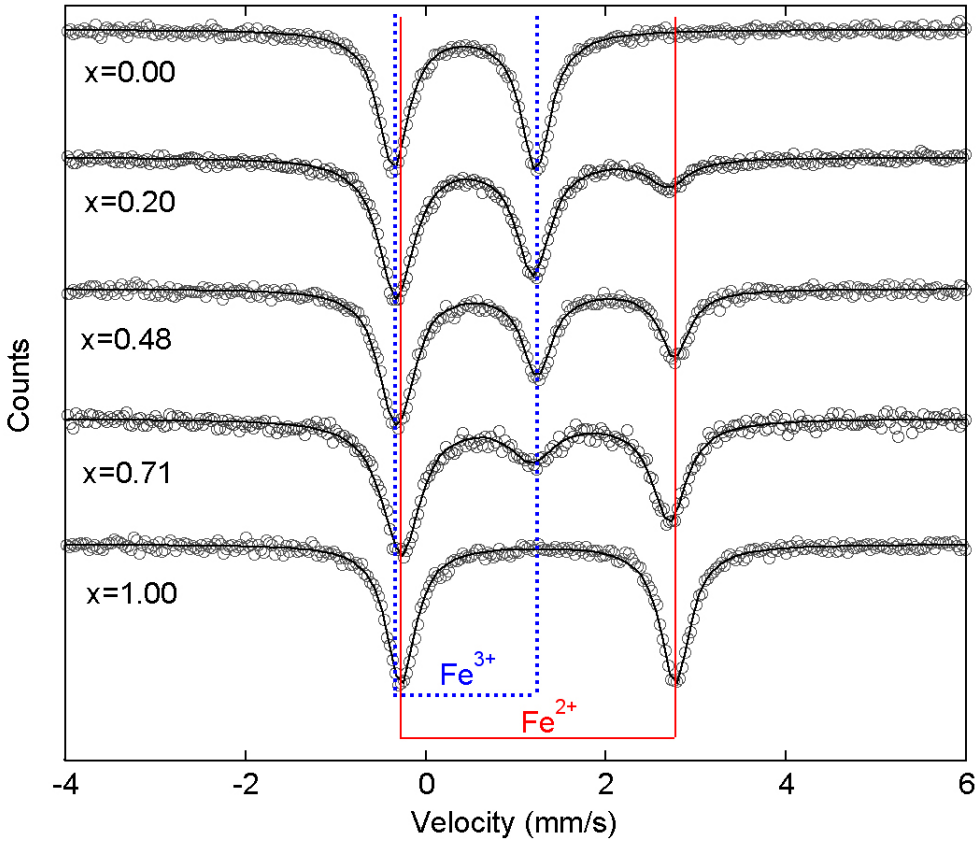

Figure 2.3: The Mössbauer spectra for five samples. Each sample has a different state of lithiation, x in Li_xFePO_4. $LiFePO_4$, where $x = 1$, has iron in the Fe^{2+} state, while $FePO_4$, where $x = 0$, has iron in the Fe^{3+} state. The doublets for Fe^{2+} and Fe^{3+} are indicated by vertical lines.

2.3 Electrochemical Operation Mechanism

The voltage curve for Li_xFePO_4 shows a potential that is independent of x over a large range of x. The flat voltage profile indicates by Gibbs' phase rule that the extraction/insertion reactions proceed by the motion of a two-phase interface. Figure 2.4 shows the voltage and current during charge and discharge of a $LiFePO_4$ cathode cycled vs. lithium at a C/20 rate. In assessment of the rate capability of the material, Padhi et al. noted that increasing the current density does not lower the OCV, but it reversibly decreases the cell capacity. Cycling again at lower rates restores the capacity, indicating the loss in capacity is a diffusion-limited phenomenon associated with the two-phase nature of the insertion process or the low electrical conductivity of the material [13].

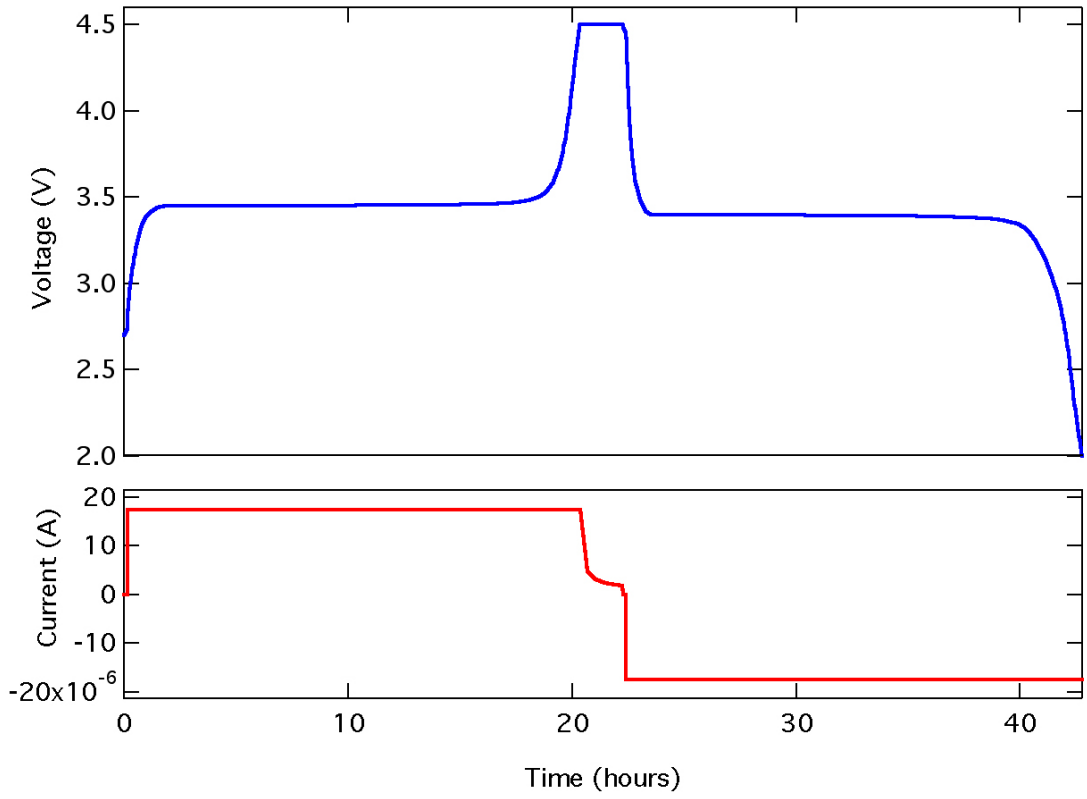

Figure 2.4: Voltage profile for $LiFePO_4$ cathode cycled vs. lithium metal. The current applied to the cell is also shown (17.4 μA for a C/20 rate). The cell capacity was 170 mAh/g, which is the theoretical achievable capacity.

A core-shell model was initially proposed for the $LiFePO_4$ system [13]. In this model, as delithiation proceeds from the particle surface, the surface area of the two-phase interface shrinks, until the rate of lithium transported across the interface is no longer able to sustain the current, and the cell performance becomes diffusion limited. Later evidence has given other ideas on the model of lithium diffusion in $LiFePO_4$.

First of all, lithium has been found to diffuse more quickly in the b direction than the a or c directions. First principle electronic structure calculations suggest that the activation energy for diffusion is much lower along the b-axis (the direction of lithium chains in the structure) and much higher in other directions (270 meV compared to 2.5 eV and 1 eV, for $x = 1$ in Li_xFePO_4) [32, 33]. Therefore, lithium diffusion is essentially restricted to the tunnels along the b-axis, so that this material is a one-dimensional ionic conductor. Therefore, it would be important to synthesize material which is thinner in the b-axis direction, to optimize it by increasing the percentage of electroactive ac faces of the crystals.

High-resolution transmission electron spectroscopy was performed on $LiFePO_4$ in two different studies. In both cases, platelet-type materials which were much thinner in the b-axis direction were studied. In the first, Chen et al. found dislocations in the direction of the c-axis which appear to be aligned with the bc plane. The dislocations probably form due to the mismatch in lattice parameters between $LiFePO_4$ and $FePO_4$. Due to the orientation of the dislocations, the interface between $LiFePO_4$ and $FePO_4$ could be in the bc plane, and the phase boundary can progress in the a-axis direction while lithium ions move in the b direction. In the second study, Laffont et al. used high-resolution electron energy loss spectroscopy to find that the phase transition occurs by a successive emptying or filling of the lithium channels in the b-axis direction. They found that for the various compositions tested (Li_xFePO_4 with $0 < x < 1$), $FePO_4$ was always found at the core, surrounded by $LiFePO_4$, independent of whether the sample was processed by delithiation or lithiation [34]. Due to the $LiFePO_4$ and $FePO_4$ cell volumes (291 $Å^3$ for $LiFePO_4$ compared to 272 $Å^3$ for $FePO_4$) it makes sense that $FePO_4$ is found in the core, since the phase with the smaller unit-cell volume would be more likely to be located in the core of the particles rather than the periphery, also suggested by Prosini [35].

2.4 Methods for Improved Performance

One major concern about the performance of this cathode material is its low intrinsic electrical conductivity [13, 31]. Pristine $LiFePO_4$ (in the absence of carbon) has an electrical conductivity of $\sim 10^{-9}$ S cm^{-1} [30, 36], which is a quite low value compared to the $\sim 10^{-3}$ S cm^{-1} conductivity of $LiCoO_2$ [37]. Much work has been done to improve the electrical performance of $LiFePO_4$ by particle-size minimization [23], addition of carbon coating [38, 39], or by doping the material with supervalent cations [30]. These methods of improvement will be discussed here.

2.4.1 Carbon-coating techniques

Since $LiFePO_4$ is an insulating material, it was initially found to have poor rate capability as an electrode material, even when mixed with carbon additives. However, several methods of carbon coating have been shown to be useful in promoting higher rate capability, allowing electrochemical cycling with nearly the theoretical capacity of $LiFePO_4$ at room temperature. The first carbon coating was shown by Ravet et al., with almost the full theoretical capacity achieved at 80 °C in a polymer electrolyte cell [40]. Huang et al. made $LiFePO_4$/C composites by mixing the precursors with a carbon gel during material synthesis, resulting in particle size minimization and intimate carbon contact, achieving 162 mAh/g at a C/10 rate (95% of lithium accessible)and 153 mAh/g at C/2 rate (90% of lithium accessible) [38]. In this case, the carbon content in the composite was 15%. Other carbon coating techniques allowed similar performance, with lower carbon contents. Chen and Dahn mixed table sugar with the other raw materials, resulting in 3.5 weight % of carbon in the $LiFePO_4$/C composite, but also added 7 weight % super-S carbon black in making their electrodes [39]. Belharouak et al. used a vapor-deposition technique to carbon coat $LiFePO_4$, arriving at capacities of 140 mAh/g at C/3 rate with only 3 weight % of carbon in the electrodes [41].

2.4.2 Particle size minimization

Due to the relatively low rate capability of $LiFePO_4$, many processing methods have been attempted in order to improve its performance. Particle size minimization is a way to reduce the length of ionic diffusion pathways of lithium. Optimization of the synthesis method is a key point. Yamada et al. [23] experimented with the sintering temperature, finding that although the pure olivine phase could be formed at much lower temperatures (around 300 °C), the cathode performance depended strongly on sintering temperatures, and the capacity was maximized when the sintering temperature was 500–600 °C. Sintering above 600 °C resulted in an abrupt particle growth, which was clearly linked with a decrease in rate capability and capacity. In these studies, at 550 °C the material had a 160 mAh/g specific capacity with particles with radii of less than 30 microns. However, the material also included 20% of conductive carbon and probably was cycled at low rates. In order to improve even further on rate capability, many further studies have gone in the direction of nanoscale particles, down to even 50 nm diameters [42].

2.4.3 Doping

A key limitation of using $LiFePO_4$ as a cathode material has been its extremely low conductivity. Approaches of carbon coating and particle size minimization can help in overcoming this issue. However, both approaches result in loss of total energy density; in carbon coating by the addition of electrochemically inert additives, and smaller particles can result in a lower tap density and volumetric capacity.

Chung et al. reported a method to improve the material's lattice electronic conductivity, by selectively doping it with supervalent cations [30]. The result is an increase in conductivity by a factor of 10^8, to values of greater than 10^{-2} S/cm at room temperature. Dopants tested include Zr^{4+}, Ti^{4+}, Nb^{5+}, and Mg^{2+}, all giving significantly higher conductivities when doped at 1 atom % at the Li site (for example to form $Li_{0.99}M_{0.01}FePO_4$). The resulting material was tested electrochemically, resulting in exceptional high rate performance, with greater than 110 mAh/g for 20C discharge rates at room temperature [43], making this $LiFePO_4$ material suitable for high rate applications such as power tools or hybrid electric

vehicles.

It has been hypothesized that improvement in conductivity is possible due to extension of the solid solution region for the pure $LiFePO_4$ phase, making a lithium-deficient solid solution $Li_{1-a}FePO_4$. This could promote charge compensation by Fe^{3+}, resulting in p-type conductivity. Similarly, for the $FePO_4$ phase in which Fe is trivalent, cation doping would result in formation of Fe^{2+}, and n-type conductivity should result. It has also been suggested that in addition to the extended lithium miscibility of doped nanoscale powders, the reduced lattice misfit between the coexisting phases correlates with a higher power capability [44]. This idea will be discussed further in section 2.5.2.

Since this work on doping with supervalent cations showed such a large increase in conductivity, even though $LiFePO_4$ is normally an insulator material, several other research groups have tried to reproduce the doping, but without the same conclusions or success. Some claim that the high conductivities measured by Chung et al. were due to carbon-coating of their doped nanoparticles, since they were synthesized from carbon-containing precursors [45, 46]. Herle et al. also claims that the high conductivity is a result of a nano-network of metal-rich phosphides [46]. Delacourt et al. also studied such doping techniques, and argued that aliovalent doping of $LiFePO_4$ is not possible, and that the process used by Chung et al. results in conductive coatings of carbon or metal phosphides on particles [47]. Chung et al. still state that high resolution microscopy results refute these claims by others [30], but as of yet, an agreement among the scientific community has not been found.

2.5 Phase Composition

2.5.1 Discovery of disordered phase at high temperatures

At room temperature, Li_xFePO_4 has been shown to behave as a two-phase system, both by its flat voltage profile and by XRD and Mössbauer results. Delacourt et al. investigated the thermal behavior of several $x\text{LiFePO}_4/(1-x)\text{FePO}_4$ $0 \leq x \leq 1$ two-phase mixtures, and discovered an intermediate solid solution phase, with lithium composition in between the heterosite and triphylite phases [48]. They found the formation of diffraction peaks intermediate to those of $LiFePO_4$ and $FePO_4$ starting at around 200 °C, which gave rise to

well-defined new sets of reflections from the new Li_xFePO_4 phases at around 350 °C. These Li_xFePO_4 phases have the same orthorhombic Pnma structure as $LiFePO_4$ and $FePO_4$, but with intermediate lattice parameters, depending upon the degree of lithiation, x. Further neutron diffraction studies showed no evidence of lithium ordering within the solid solution phases [49], suggesting that lithium is disordered throughout the lithium sites. These results also suggested anisotropic strains in the [100] and [010] directions (more so in the [100] direction) suggesting that lithium heterogeneities could exist in either of these directions.

The existence of a single-phase Li_xFePO_4 solid solution is an exciting topic which has spurred several studies (including some of the studies which will be explained in this thesis). Some speculate that the two-phase delithiation process in $LiFePO_4$ may be the origin of electrochemical limitations and the low intrinsic ionic and electronic conductivity of $LiFePO_4$ [36]. Therefore, it is interesting to determine whether these solid solution phases exhibit higher conductivities or could result in a higher rate capability $LiFePO_4$ cell if they can be stabilized at lithium cell working temperatures.

2.5.2 Miscibility gap and solid solution regions

Until recently, the delithiation of $LiFePO_4$ has been generally explained as a two-phase system, with $LiFePO_4$ and $FePO_4$ being the two constituent phases. However, in the last couple of years, studies have shown that the miscibility gap is not between 0 and 1, but between α and $1-\beta$, and that there are some lithium defects in heterosite phase ($Li_\alpha FePO_4$), and vacancy defects in the triphylite phase ($Li_{1-\beta}FePO_4$).

Yamada et al. first published an x-ray diffraction study showing that intermediate Li_xFePO_4 samples were composed of $Li_\alpha FePO_4$ and $Li_{1-\beta}FePO_4$ phases, where $\alpha \sim 0.03$ and $\beta \sim 0.04$ at room temperature [50]. The data suggested narrow monophase regions ($0 < x < \alpha$ and $1 - \beta < x < 1$) close to the stoichiometric end members, and that for intermediate x, the two-phase reaction involves $Li_\alpha FePO_4$ and $Li_{1-\beta}FePO_4$. In follow-up experiments [51], neutron diffraction measurements indicated site occupancies of lithium to be $\alpha = 0.05$ and $1 - \beta = 0.89$. Microcalorimetry and OCV measurements indicated corresponding solid solution ranges outside the miscibility gap. The differences between α and β values from the first to second experiments seems to be dependent upon the material

particle size. For Yamada's XRD study, the material particle size ranged from 100 to 200 nm [50] while for the second set of studies, the particles were around 100–120 nm in diameter [51].

Meethong et al. probed the α and β values of $Li_{\alpha}FePO_4$ and $Li_{1-\beta}FePO_4$ for particle sizes between 34 nm and 113 nm by Rietveld analysis of XRD patterns and potentiostatic measurements at temperatures $-23\,^{\circ}C$, $23\,^{\circ}C$, and $45\,^{\circ}C$ [52]. They found that the miscibility gap contracts systematically with decreasing particle size and increasing temperature, attributing the effect primarily to coherency stresses. They also note that by decreasing the particle size, as α and β increase, the lattice parameters between the two phases approach each other, resulting in less lattice misfit between phases. Chiang's group also found higher lithium miscibility and smaller lattice misfits in their doped nanoparticles, compared to regular nanoparticles, and have proposed that this smaller lattice misfit can be a reason for their higher power capabilities. If the lattice misfit is small enough the material can have a coherent interface while cycling vs. lithium, while for a larger lattice misfit the interface has enough strain that it is incoherent, with the strain reduced by generating dislocations at the interface. For the incoherent interface, either the phase transformation has to proceed slowly enough to allow the dislocation migration, or additional dislocations must be generated as the interface moves. In contrast, migration of a coherent interface is only limited to Li transport rates. This could explain why nanoparticles, especially doped nanoparticles, have such higher rate capabilities compared to conventional materials.

2.6 Summary

Although many improvements in $LiFePO_4$ cathodes have been achieved in the past decade, there are still new stones to be turned. Particularly, the phase composition is still an important area of study, along with the mechanisms of cell operation and phase transformation and further improvements to the material rate capability. These topics are all interrelated, and will be discussed in further chapters of this thesis.

Chapter 3

Experimental Techniques

3.1 X-Ray Diffraction

X-ray diffraction (XRD) was used extensively for the characterization of materials in our studies. It is a powerful method for determining how atoms are arranged into crystal structures. For our measurements, Cu Kα radiation, with wavelength $\lambda = 1.5406$ Å was used. The x-ray diffractometers used were a Rigaku Co. R2000 and PANalytical X'Pert PRO X'Celerator. Since our samples were in powder form, the powders were pressed flat on a zero background holder to obtain a uniform sample height. Silicon powder was added to most samples as a standard to aid in corrections for any height variation between samples, since the reference peaks from Si are known.

PANalytical X'Pert High Score software was used to determine peak positions and to remove Kα_2 peaks. X'pert Highscore was also used to identify the phases of the material by cross-referencing a structure database. After phase identification, Rietveld analysis was used to determine phase fractions present in the samples by using X'pert Plus software (PANalytical).

3.2 Mössbauer Spectrometry

3.2.1 Overview

Mössbauer spectrometry is a powerful technique for probing the electronic structure near the nucleus. It measures the spectrum of energies at which specific nuclei absorb γ rays.

The Mössbauer effect is the recoilless emission of a γ-ray photon by a nucleus [53]. In 1957 Rudolf L. Mössbauer discovered that recoilless emission and absorption of γ rays by a nucleus can sometimes occur in a solid without the excitation of phonons. The Mössbauer effect is optimized for low-energy γ rays, nuclei strongly bound in a crystal lattice, and low temperatures. Some of the nuclei which can be studied due to this effect include ^{57}Fe, ^{119}Sn, ^{151}Eu, ^{121}Sb, and ^{161}Dy [54]. The most extensively studied isotope is ^{57}Fe, and the technique of Mössbauer spectrometry has been widely used for the investigation of iron-containing systems.

In Mössbauer spectrometry, the energy levels of a nucleus are investigated by measuring the energies of resonant absorption of γ rays by nuclei. The resonant absorption of γ rays is of an extremely precise energy. Without the energy variations associated with phonon creation or annihilation, very small energy changes resulting from hyperfine interactions between the nucleus and its surrounding electrons can be measured, thus providing a probe of the nucleus's environment. The experimental setup for Mössbauer spectrometry includes a radioactive source containing the Mössbauer isotope in an excited state and the material to be investigated, which contains this same isotope in its ground state. In particular, since this study deals with measurements of $LiFePO_4$, ^{57}Fe Mössbauer spectrometry will be described in more detail.

For this case, ^{57}Co is used as the radioactive source. By a spontaneous electron capture, the source changes to a metastable state of ^{57}Fe and then decays to the ground state, emitting γ rays, particularly a 14.41 keV Mössbauer γ ray. The emitted γ rays are passed through the sample, where some of them are absorbed, and then the remaining γ rays continue on to a detector. To investigate the energy levels in the sample, the energy of the γ ray beam is varied through the energies for resonant absorption. The energy modification is performed by moving the source relative to the absorber, thus shifting energy as a result of the first-order relativistic Doppler effect. This setup for the experiment is depicted in figure 3.1.

Energy shifts of nuclear levels caused by hyperfine interactions are of the order 10^{-7} eV. These shifts can be achieved by Doppler shifting the energy of the photon. The Doppler shift ΔE imparted on the photon due to a relative velocity v of the source is $E_\gamma v/c$, so that

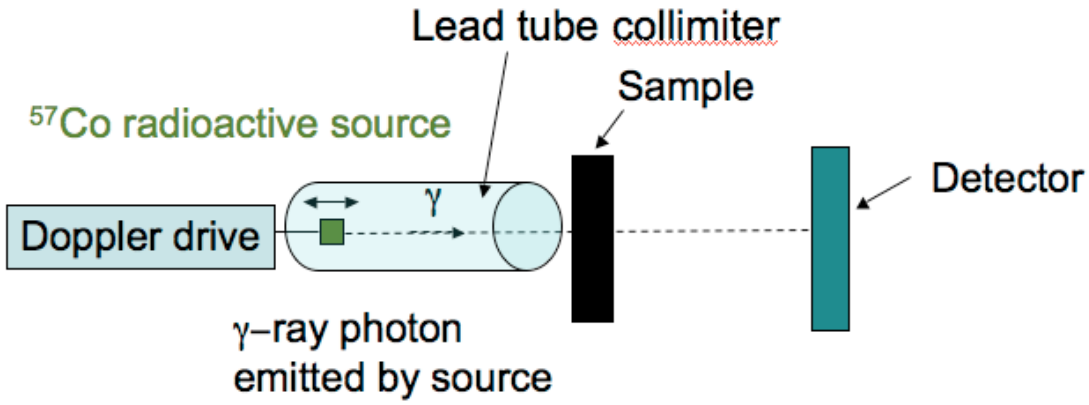

Figure 3.1: Setup for Mössbauer spectrometry measurements.

the resulting photon energy E'_γ can be expressed as

$$E'_\gamma = E_\gamma(1 + v/c), \tag{3.1}$$

where E_γ is the photon energy in the reference frame of the source, and c is the speed of light in vacuum. For the 14.41 keV γ ray of ^{57}Fe, the velocities needed are on the order of several mm/s. An energy range of $\pm$ 10 mm/s would give an energy shift of 4.8×10^{-7} eV to a 14.41 keV γ ray, which is usually sufficient to investigate the Mössbauer energy spectrum for ^{57}Fe. The following sections describe some of the properties which can be measured by Mössbauer spectrometry. The isomer shift and electric quadrupole splitting were measured in our study on valence fluctuations of ^{57}Fe in Li_xFePO_4, discussed in chapter 7.

3.2.2 Isomer shift

The peaks in a Mössbauer spectrum undergo observable shifts in energy depending on the material in which the Mössbauer atom is located. These shifts in energy originate from hyperfine interactions between the nucleus and nearby electrons. This interaction is called the isomer shift, and is a measure of the electron density at the nucleus. For s electrons (1s, 2s, 3s, etc.) the electron wavefunction is quite large in magnitude at r = 0 (inside the nucleus). The overlap of this s-electron wavefunction with the nucleus causes a Coulomb

perturbation which lowers the nuclear energy levels. The nuclear radius changes when it enters an excited state (similarly to an atomic radius changing when electrons are excited). For ^{57}Fe, the effective radius of the excited nucleus, R_{ex}, is smaller than the radius of the ground state, R_g. For ^{119}Sn, the opposite is true. For a constant charge density, when the nucleus is smaller, the total electrostatic attraction is stronger. Therefore, because of the Coulomb perturbation, the difference in energy between the nuclear excited state and ground state is a function of the electron density [54]. Since the shift in this transition energy is usually different for nuclei in the radiation source and the nuclei in the sample, the shift of the absorption peak in the measured spectrum is as follows:

$$\Delta E_{IS} = \delta = CZe^2(R_{ex}^2 - R_g^2)\left[|\Psi_{sample}(0)|^2 - |\Psi_{source}(0)|^2\right]. \tag{3.2}$$

The factor C depends on the shape of the nuclear charge distribution. For ^{57}Fe, since $R_{ex} < R_g$, for a sample with a greater s-electron density at the nucleus than the source the Mössbauer peaks will be shifted to a more negative velocity.

For the Fe nucleus, 3d electrons partially screen the nuclear charge from s electrons, so an increase in 3d electrons at an ^{57}Fe atom will increase this screening and reduce the s-electron density at the nucleus, resulting in a positive isomer shift. Therefore, Fe^{2+} has a larger isomer shift than Fe^{3+}. For Fe_o there are more s electrons at the nucleus than for its ionic counterparts, mainly because it has about one 4s electron, which Fe^{2+} and Fe^{3+} do not have. Therefore, the isomer shift is sensitive to chemical influences such as valence state, spin state, and bonding. The s-electron density at the nucleus is directly changed by changing the s-electron population in the valence shell or indirectly through shielding by other electrons. In this manner, the valence state of Fe atoms can be deduced from Mössbauer spectra. Below are the trends for electron density at the nucleus and isomer shifts for Fe:

$$\Psi_o^2(0) > \Psi_{3+}^2(0) > \Psi_{2+}^2(0),$$
$$\delta_o < \delta_{3+} < \delta_{2+}.$$

Figure 3.2(a) depicts the Mössbauer spectrum for an ^{57}Fe nucleus with less electron density than Fe_o, and the resulting positive isomer shift.

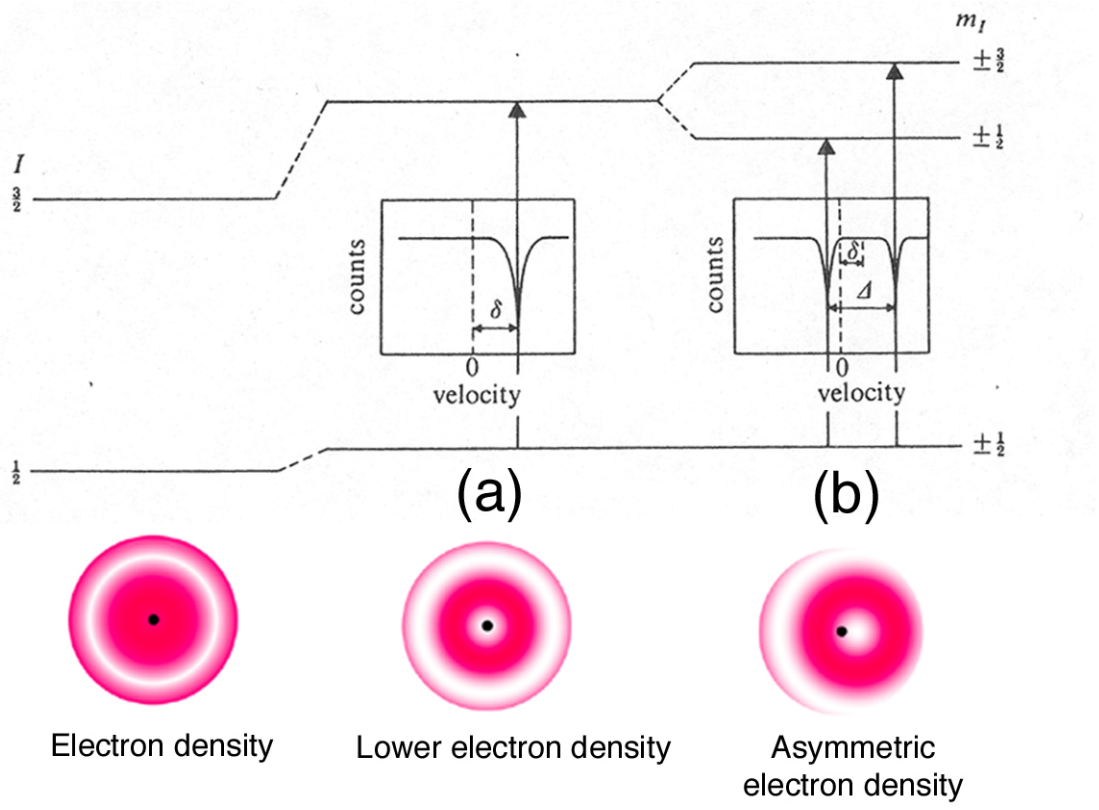

Figure 3.2: Schematic showing an energy level diagram for ^{57}Fe, and its perturbation (a) with a lower electron density and (b) in the presence of an electric field gradient. A portion of this figure was replicated from reference [55].

3.2.3 Electric quadrupole splitting

Another measurable effect in Mössbauer spectrometry is the electric quadrupole splitting. This effect indicates the asymmetry of the nucleus. Nuclei in states with nuclear angular momentum quantum number $I > 1/2$ have non-spherical charge distributions which are characterized by a nuclear quadrupole moment [55]. An asymmetric electronic charge distribution causes an asymmetric electric field, or electric field gradient (EFG). When the nuclear quadrupole moment interacts with the EFG, an electric quadrupole interaction occurs, resulting in a splitting of the nuclear energy levels corresponding to different alignments of the quadrupole moment with respect to the principal axis of the EFG.

For ^{57}Fe, the excited state has $I = 3/2$ and an electric field gradient splits its energy into two substates characterized by $m_I = \pm 1/2$ and $m_I = \pm 3/2$. This splits the original single peak into two peaks separated by the quadrupole splitting Δ. Figure 3.2(b) shows the splitting in energy levels and the resulting Mössbauer spectrum when in the presence of an electric field gradient.

The quadrupole splitting deals with both a nuclear and electronic quantity, the nuclear quadrupole moment and the electric field gradient, respectively, but since the nuclear quadrupole moment is fixed for a given nucleus, details of the EFG can be derived from a Mössbauer spectrum. The asymmetry of the electronic structure can be due to partially filled electronic shells occupied by valence electrons or due to local atomic arrangements, such as ligand charge and coordination.

3.3 Preparation of $LiFePO_4$ Material

3.3.1 Synthesis of $LiFePO_4$

$LiFePO_4$ material was prepared by a solid-state reaction consisting of a mixture of iron(II) oxalate $Fe(C_2O_4)\cdot 2H_2O$, ammonium dihydrogen phosphate $NH_4H_2PO_4$, and lithium carbonate Li_2CO_3 in the molar ratio (1:1:0.5). The precursors were mixed by ball milling in acetone overnight. The resulting gel was dried at 60 °C under vacuum, thoroughly reground, and heated under purified N_2 gas for 24 hours at 700 °C [29]. Powder was synthesized in this manner by Argonne National Lab, who provided us with enough powder to

perform most of our studies (including the phase diagram, thermostability, Mössbauer, and conductivity studies).

3.3.2 Chemical delithiation of $LiFePO_4$

We delithiated this material chemically by use of potassium persulfate ($K_2S_2O_8$) in an aqueous solution, as follows:

$$LiFePO_4 + \frac{y}{2}(K_2S_2O_8) \rightarrow (1-y)LiFePO_4 + yFePO_4 + \frac{y}{2}(Li_2SO_4 + K_2SO_4), \quad 0 < y < 1. \tag{3.3}$$

The $K_2S_2O_8/K_2SO_4$ redox couple has a Nernst standard potential of approximately 5 V vs. Li/Li^+, which is higher than the 3.5 V vs. Li/Li^+ for $Li_{0.0}FePO_4/Li_{1.0}FePO_4$ couple. Therefore, $K_2S_2O_8$ can oxidize $LiFePO_4$ to full delithiation.

The methods for chemical delithiation were as follows:

1. The quantities of $K_2S_2O_8$ and $LiFePO_4$ were weighed out.

2. The $K_2S_2O_8$ was dissolved in deionized water, noting that the solubility of $K_2S_2O_8$ in water is 4.7 g per 100 g H_2O. This solubility limit was not exceeded.

3. Following the dissolution of $K_2S_2O_8$ in the water, $LiFePO_4$ was added to the solution. For consistency, 50 ml of deionized water was used for each 1 g of $LiFePO_4$ which was delithiated.

4. The solution of $K_2S_2O_8$ and $LiFePO_4$ was mixed at ambient temperature for 24 hours, allowing equilibrium to be reached. The flask was covered with paraffin waxed paper to avoid evaporation of the water.

5. After the mixing time, the solution was filtered with a Whatman No. 5 filter paper, using a Buchner funnel and vacuum filtration. After the powder was removed from solution, it was rinsed by adding the material to a flask of deionized water and mixing with a stir bar for another 15 minutes. This filtering and rinsing procedure was repeated two times, to ensure the $K_2S_2O_8$ and its products were rinsed from the $LiFePO_4$. To obtain higher yields, after each filtration, the filter paper was dried at

approximately 50–60 °C, and making it easier to scrape the $LiFePO_4$ powder from the filter paper.

6. After filtration and rinsing, the material was dried in vacuum at 110 °C for 8–12 hours.

By altering the molar ratio of $K_2S_2O_8$/$LiFePO_4$, samples with different amounts of lithium were prepared. A plot showing the consistency between the targeted and measured lithiation x in Li_xFePO_4 is shown in figure 3.3. The measured x was determined by Rietveld refinement of XRD patterns to find the relative amounts of the two phases, and assuming $x = 1$ for triphylite and $x = 0$ for heterosite.

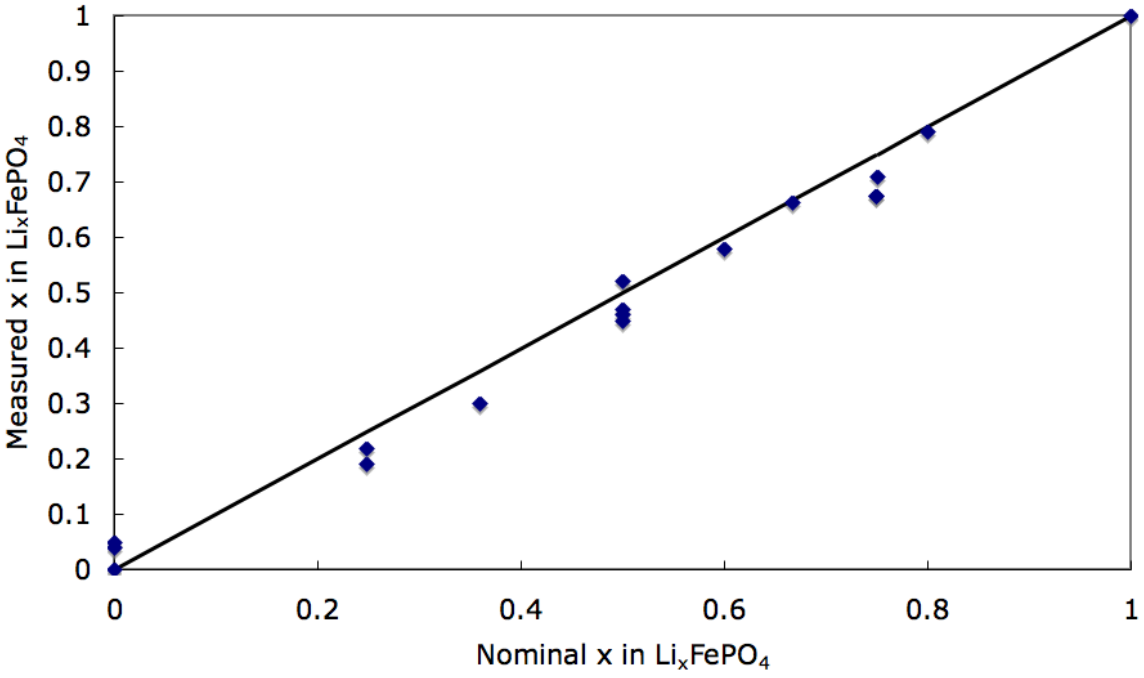

Figure 3.3: Comparison between the calculated value of lithiation and the measured value, for samples delithiated chemically using $K_2S_2O_8$. The nominal values are based on equation (3.3), while the measured values are based on Rietveld refinement of XRD patterns.

3.4 Electrochemical Cell Testing

3.4.1 Cell construction

Coin cells are often used to electrochemically cycle lithium-ion battery materials. For these studies, both 2016 and 2034 cells were used (both with 20 mm diameters and thicknesses of 16 mm and 34 mm respectively). Half-cells consisting of a cathode cycled versus lithium metal were used. The cell components included:

- 17 mm diameter lithium metal disk, 0.75 mm thick
- 19 mm diameter microporous polypropylene separator (Celgard 3401) soaked in electrolyte
- Electrolytes used: 1.2 M $LiPF_6$ salt in ethylene carbonate/diethylene carbonate (EC/DMC) solvents and 1 M lithium bis(oxalato)borate salt (LiBOB) in propylene carbonate (PC)
- 14–16 mm diameter cathode electrode, prepared by a film deposition method
- Additional spacers: stainless steel metal disk of 0.2 mm thickness and Cu foil inserts of 10 μm thickness for adjustments in the cell pressure
- Stainless steel coin cell top and bottom and plastic gasket

The materials were dried and then stored in a glove box filled with argon. The coin cells were then constructed in the glove box and crimped shut. The order of assembly was (from bottom to top of cell):

1. Stainless steel cell bottom with plastic gasket fitted over its edges
2. Copper foil spacers (if necessary) and stainless steel metal spacer
3. Lithium metal disk
4. Polypropylene separator (soaked in electrolyte)
5. Cathode
6. Stainless steel cell top

Once coin cells were crimped together with an air-tight seal, they were checked for short circuits by measuring the cell voltage. If satisfactory, they could be taken out of the glove box for further testing in the lab.

3.4.2 Cathode film fabrication

Cathode films were made by mixing $LiFePO_4$ material with a polyvinylidene difluoride (PVDF) binder and acetylene black (AB). PVDF is a film binder commonly used in lithium-ion batteries. Acetylene black is a conductive material added to improve rate capability of the electrode. For a film of 12.7 cm diameter and between 50 and 100 μm thick, the following masses were used:

Electrode Component	Mass (g)	Weight %
$LiFePO_4$	0.225	75
PVDF	0.045	15
AB	0.030	10
Total	0.300	100

Table 3.1: Cathode film components.

The following steps were used to prepare the electrode films:

1. All three powders were weighed and mixed with a mortar and pestle (a light grinding so as not to break up particles, just to thoroughly mix the powders).

2. The powder was added to a small flask or bottle, and acetone was added to the powders, along with a stir bar. The amount of acetone was minimal, just enough to obtain a slurry. The solution was stirred for 2 hours.

3. The slurry was then poured into a teflon mold of diameter 12.7 cm, which was lined with aluminum foil. Care was taken to make sure the slurry was evenly distributed throughout. Acetone evaporated at ambient temperature.

4. Disc electrodes (14–16 mm diameter) were cut with a steel die.

5. Disc electrodes were dried at 110 °C in vacuum for several hours.

6. Electrodes were weighed on a scale (0.1 mg accuracy).

7. Disc electrodes were again dried at 110 °C in vacuum for at least 8 hours, then brought into the glove box.

3.4.3 Galvanostatic cycling

Coin cells were cycled (charged and discharged) by applying a constant current and monitoring the cell voltage. The cathode materials were cycled vs. lithium metal, so all voltages discussed here are in reference to the Li/Li^+ electrochemical couple. The current applied to the cell was determined based on its theoretical capacity, which was calculated based on the working electrode active material mass.

A common convention is to refer to the cycling rate of batteries as the "C-rate." At a C/n rate, the cell will be fully charged or discharged in n hours. To discharge at a C/n rate, the current is chosen such that I = C/n, where C is the cell capacity and n is the number of hours chosen for discharge time. For example, to discharge a 100 mAh cell at C/2 rate (it will take approximately 2 hours to discharge it), the current chosen is 50 mA. Since $LiFePO_4$ generally has a low rate capability, for our tests we usually chose either a C/10 or C/20 rate.

A 16 channel cycler model BT2000 manufactured by Arbin Instruments was used to cycle cells, allowing initial capacity determination and also cycling tests. For capacity determination of $LiFePO_4$ cells, cells were charged at a C/20 rate, up to 4.5 V, then held at constant voltage at 4.5 V until the current dropped to a C/200 rate. After 10 minutes rest time, the cells were then discharged at a C/20 rate to 2.0 V. For cell capacity determination, cells were usually cycled 5 times to ensure reproducibility.

3.4.4 Open-circuit voltage vs. temperature measurements

Open-circuit voltage vs. temperature measurements were performed on coin cells to calculate the entropy and enthalpy of lithiation in $LiFePO_4$ and related materials. The results of these measurements will be discussed in chapter 6.

An automated electrochemical thermodynamic measurement system was developed by

Yvan Reynier, a previous student in our laboratory. This system uses a Visual Basic program to control the experiment and record the data. An Agilent 3633 power supply provides current to a Peltier plate to cool coin cells, which are placed in thermal contact with the plate. The program also controls the data acquisition of the open circuit voltage and temperature of up to four cells. An Agilent 34970 multimeter accurate to 10 μV is used for OCV measurements. Resistive temperature detectors (RTDs) accurate to 0.1 °C are placed in contact with the Peltier plate and the cells to monitor their temperatures. The program also signals an Arbin BT4+ cycler to correlate changes in lithium composition between thermodynamic measurements. The system is shown in a schematic diagram in figure 3.4.

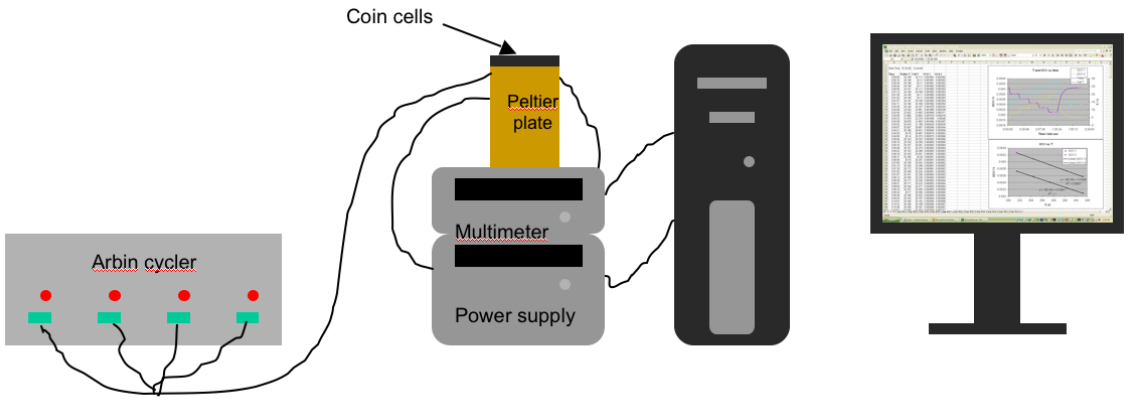

Figure 3.4: Diagram of the automated electrochemical thermodynamic measurements system (ETMS), drawn by Yvan Reynier [56].

The temperature range was between room temperature and around 12 °C. This range was chosen to minimize the self-discharge effects which would be more prevalent at higher temperatures. An example of data acquired with the ETMS is shown in figure 3.5. The temperature response of the Peltier plate is quite good, with a sharp decrease in temperature without overshoot. In this case, the OCV (E_0) increases at the temperature is decreased. In addition, however, there is a linear decrease in voltage due to self-discharge. The OCV at room temperature after the 2 hour 40 minute measurement decreased by 0.6 mV due to self-discharge. Voltage values were corrected by subtracting the self-discharge contribution

of the cell, resulting in a linear relationship between the OCV and temperature. The slope and intercept of the line shown in figure 3.6 can be used to determine the entropy and enthalpy of lithiation, which will be discussed more in chapter 6.

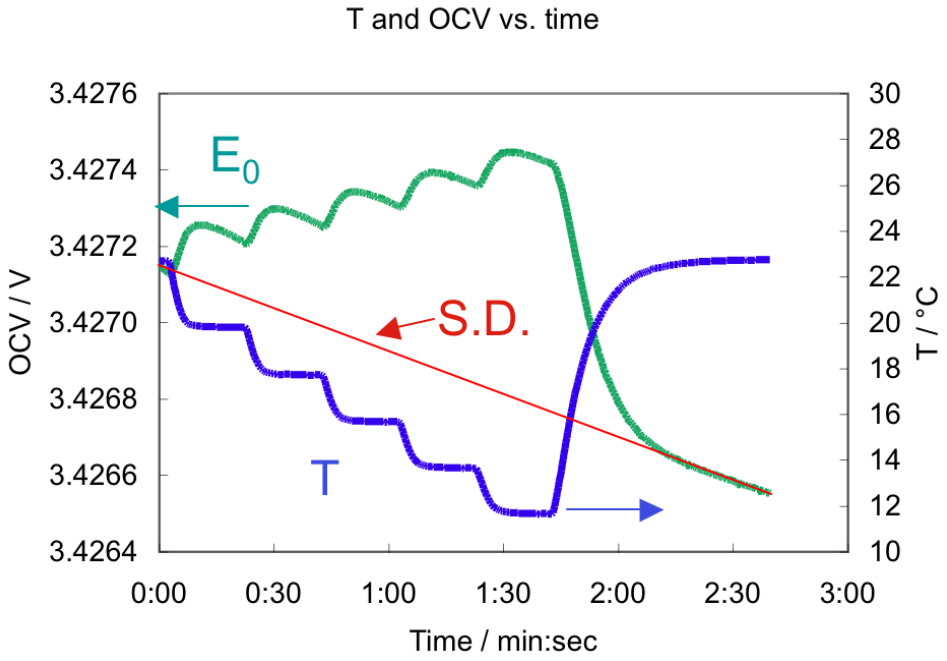

Figure 3.5: The response of the OCV (E_0) to incremental decreases in cell temperature are shown. The data shown are for a Li_xFePO_4 cell at $x = 0.75$ lithiation. Self-discharge of the cell (indicated by S.D.) also occurs during this measurement.

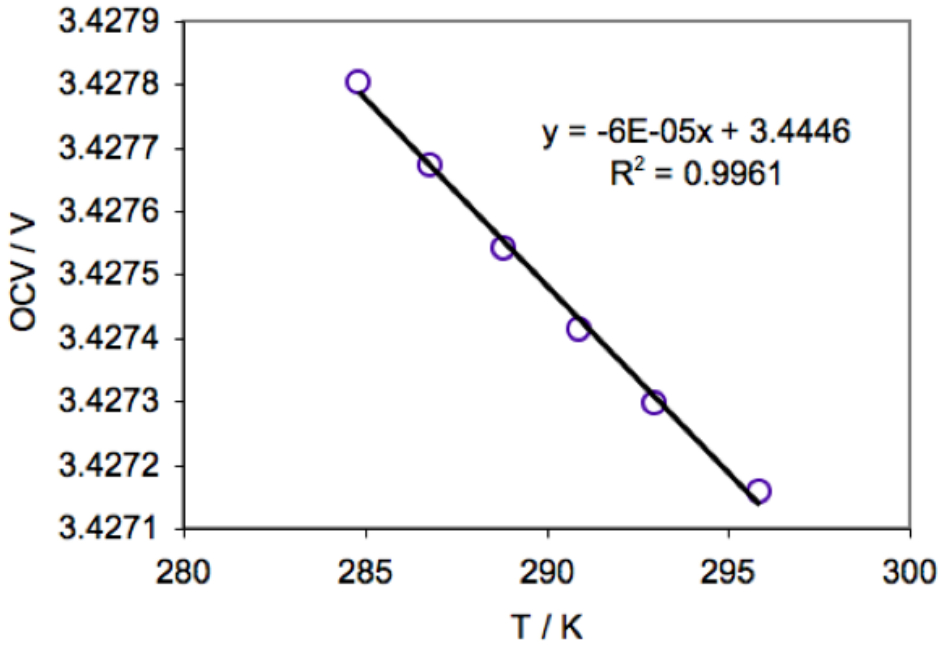

Figure 3.6: The OCV vs. T curve is plotted, showing a linear relationship.

Chapter 4

Phase Diagram of Li_xFePO_4

4.1 Introduction

The recent discovery of a single phase Li_xFePO_4 solid solution at temperatures of around 350 °C [48] has spurred great interest in determining its role in the performance of $LiFePO_4$ as a cathode material for lithium-ion batteries. A brief description of this discovery was given in section 2.5.1. Since there is no ordering of lithium among lithium sites in the solid solution phase, we refer to this Li_xFePO_4 phase as disordered. In addition, this phase forms at high temperatures where entropy plays a larger role in phase stability. We have studied the transformation of the two-phase mixture, xLiFePO$_4$ plus $(1-x)$FePO$_4$, to the single phase Li_xFePO_4 for several compositions x. The mixing and unmixing transitions are slow, but they are reversible with some hysteresis. The thermodynamics and kinetics of mixing and unmixing of xLiFePO$_4$ plus $(1-x)$FePO$_4$ $(0 \leq x \leq 1)$ to form a disordered solid solution Li_xFePO_4 are the subject of this study. Our results are summarized as a phase diagram of Li_xFePO_4, showing temperatures where the mixing-unmixing transition occurs at different lithium concentrations. There is uncertainty in the precise phase boundaries due to sluggish kinetics. The phase diagram is as expected, an unmixing system up to around 200 °C, with intermediary compounds $(0 < x < 1)$ being composed of the heterosite and triphylite phases. Above 200 °C, mixing of lithium and the formation of a disordered solid solution phase occurs. For the composition of $x = 0.6$, the disordered solid solution is stable at relatively low temperatures, much as for a eutectoid transformation.

Portions of this chapter have been published in the journal article: J. L. Dodd, R. Yazami, and B. Fultz, *Electrochem. Solid State Lett.*, **9**, A151 (2006).

4.2 Experimental

4.2.1 Chemical Delithiation

$LiFePO_4$ material was prepared by a solid-state reaction consisting of a mixture of iron(II) oxalate $Fe(C_2O_4)\cdot 2H_2O$, ammonium dihydrogen phosphate $NH_4H_2PO_4$, and lithium carbonate Li_2CO_3 in the molar ratio 1:1:0.5. The precursors were mixed by ball milling in acetone overnight. The resulting gel was dried at 60 °C under vacuum, thoroughly reground, and heated under purified N_2 gas for 24 hours at 700 °C [29]. We delithiated this material chemically by use of potassium persulfate ($K_2S_2O_8$) in an aqueous solution, as follows:

$$LiFePO_4 + \frac{y}{2}(K_2S_2O_8) \rightarrow (1-y)LiFePO_4 + yFePO_4 + \frac{y}{2}(Li_2SO_4 + K_2SO_4), \quad 0 < y < 1. \tag{4.1}$$

The $K_2S_2O_8/K_2SO_4$ redox couple has a Nernst standard potential of approximately 5 V vs. Li/Li^+, which is higher than the 3.5 V vs. Li/Li^+ for $Li_{0.0}FePO_4/Li_{1.0}FePO_4$ couple. Therefore, $K_2S_2O_8$ can oxidize $LiFePO_4$ to full delithiation. An aqueous solution of $K_2S_2O_8$ and $LiFePO_4$ was mixed at ambient temperature for 24 hours, allowing equilibrium to be reached. By altering the molar ratio of $K_2S_2O_8/LiFePO_4$, samples with different amounts of lithium were prepared.

4.2.2 Heat Treatment

The samples were purged with argon and vacuum sealed in borosilicate glass ampoules, then heated in a tube furnace. After heat treatments, the samples were taken out of the furnace and cooled quickly by blowing pressurized air over them or water quenching them, both methods giving similar results. The samples were then removed from the glass, and measured by x-ray diffraction. By using the glass tubes for heating, we were able to perform the sample reaction over long times, which we could not do with a high temperature XRD stage.

4.2.3 X-ray Diffraction

An x-ray diffractometer with Cu Kα radiation (PANalytical X'Pert PRO X'Celerator) was used to analyze and identify the phases in the material. Samples were mixed with a silicon standard powder to ensure accuracy in peak position determinations. Rietveld analysis was used to determine phase fractions present by using Philips X'pert Plus software (PANalytical). At low temperatures the system is a two-phase mixture, with nearly all the lithium in the triphylite phase. The fraction of triphylite ($LiFePO_4$) in the sample before heat treatment was determined by Rietveld analysis, and was used as a measure of the concentration of lithium in the sample. After heat treatment, samples were again analyzed with Rietveld analysis.

4.2.4 Differential Scanning Calorimetry (DSC)

Two different Netzsch differential scanning calorimeters (DSC 404C and STA 449 C) were used to scan samples at a 5 °C/minute rate from room temperature to 400 °C and then back down to room temperature. During heating and cooling, distinct endothermic and exothermic peaks were found, representative of mixing and unmixing in the sample, respectively. The sample was purged with argon throughout the measurements.

4.3 Results

Several samples prepared by chemical delithiation were studied in detail. The states of lithiation of the Li_xFePO_4 samples were x = 0.19, 0.45, 0.47, 0.66, 0.71, and 0.79. Figure 4.1 shows the XRD patterns for these samples. Diffraction patterns for $x = 0$ and $x = 1$ (heterosite and triphylite) are also shown, and indexed for the orthorhombic Pnma structures.

Samples with x = 0.00 and 1.00 were stable up to 400 °C, as reported previously [57]. However, samples with intermediate lithium concentrations showed structural changes upon heating to above 200 °C. Some results were obtained by use of a high temperature stage on the x-ray diffractometer, but due to lower signal to noise with the high temperature stage, and since the kinetics of the transformation were sluggish at temperatures below

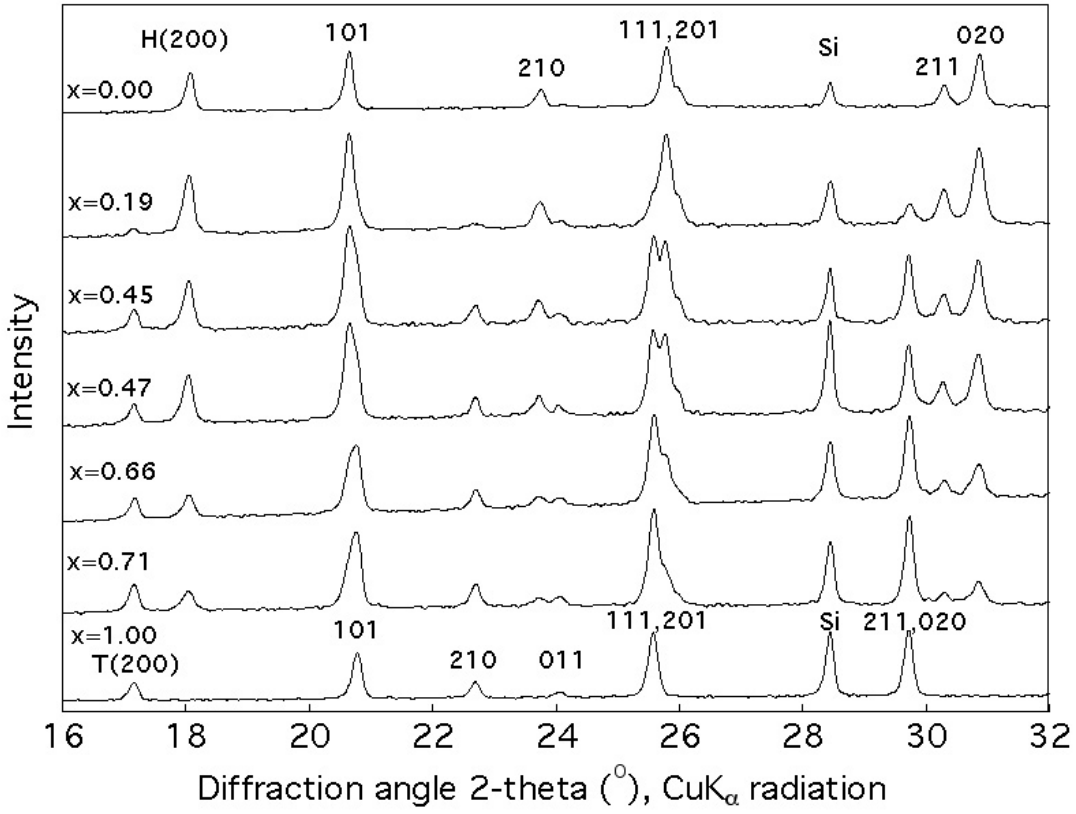

Figure 4.1: XRD patterns for samples with various delithiation. The amount of lithium in the sample is indicated as x. Diffraction peaks are labeled for the Pnma orthorhombic structure of heterosite (H) and triphylite (T).

300 °C, heat treatments for phase fraction determinations were performed for long times with samples in glass ampoules, followed by quenching. After quenching the samples, the phase structure was quite stable, with little change back toward the original phases, even after weeks or several months at room temperature.

A kinetics study was made at three temperatures, 220 °C, 260 °C, and 380 °C, using the delithiated sample with $x = 0.47$. Heat treatment times varied from 30 minutes to 4 days. At 380 °C, the sample reached equilibrium quickly, with transformation to a disordered solid solution being complete even after 30 minutes. For lower temperatures of 260 °C and 220 °C, equilibration takes a longer time, with measurements taken after 12 hours of heating differing from those taken after 2 hours. Between 12 hours and 3-4 days the changes were smaller, however. The percentages of disordered phase present in each sample as a function of time, determined by Rietveld refinement, are shown in figure 4.2 for three temperatures.

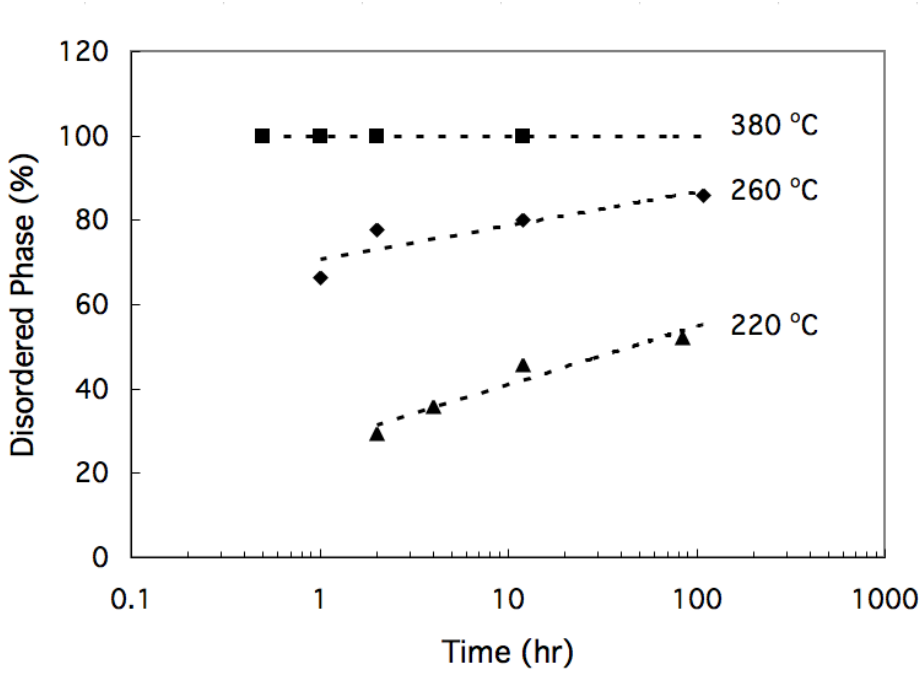

Figure 4.2: Comparison of kinetics of formation of disordered phase for samples with lithium composition $x = 0.47$. The percentage of disordered phase in each sample is plotted as a function of time held at the following temperatures: 220 °C, 260 °C and 380 °C.

A 12-hour isothermal hold of the samples was selected for a further assessment of the

equilibrium state. Although the samples did not reach equilibrium within 12 hours, especially at temperatures below 300 °C, the formation or loss of phases at different temperatures for a specific composition identified the equilibrium tendencies of the system. Figures 4.3, 4.4, and 4.5 show a series of x-ray scans for samples of $x = 0.47$, 0.66, and 0.71 heated to different temperatures for 12 hours. It is easy to see the extent of formation of the disordered solid solution from the initial mixture of the heterosite and triphylite phases by looking at the angles between 16° and 19° (200 peaks) and also at 29° to 31° (020 and 211 peaks). The transformation begins at 200 °C, and the solid solution is distinct at 220 °C, where all three phases are present. At 260 °C, each sample consists of two phases, the disordered phase and either triphylite (for $x = 0.71$, 0.66) or heterosite (for $x = 0.47$). The complete transition to the disordered solid solution is found for samples treated to above 300 °C.

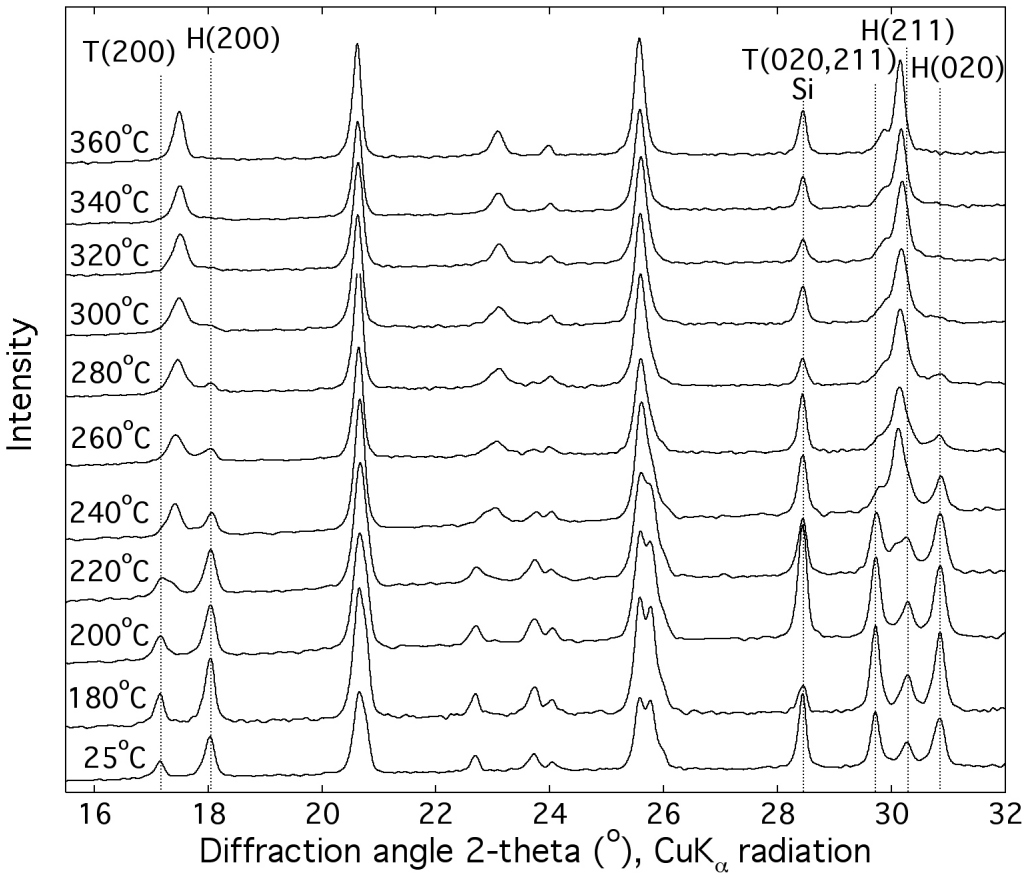

Figure 4.3: Series of XRD patterns for samples with lithium composition $x = 0.47$. Each sample was held at the noted temperature for 12 hours, and then quenched to room temperature.

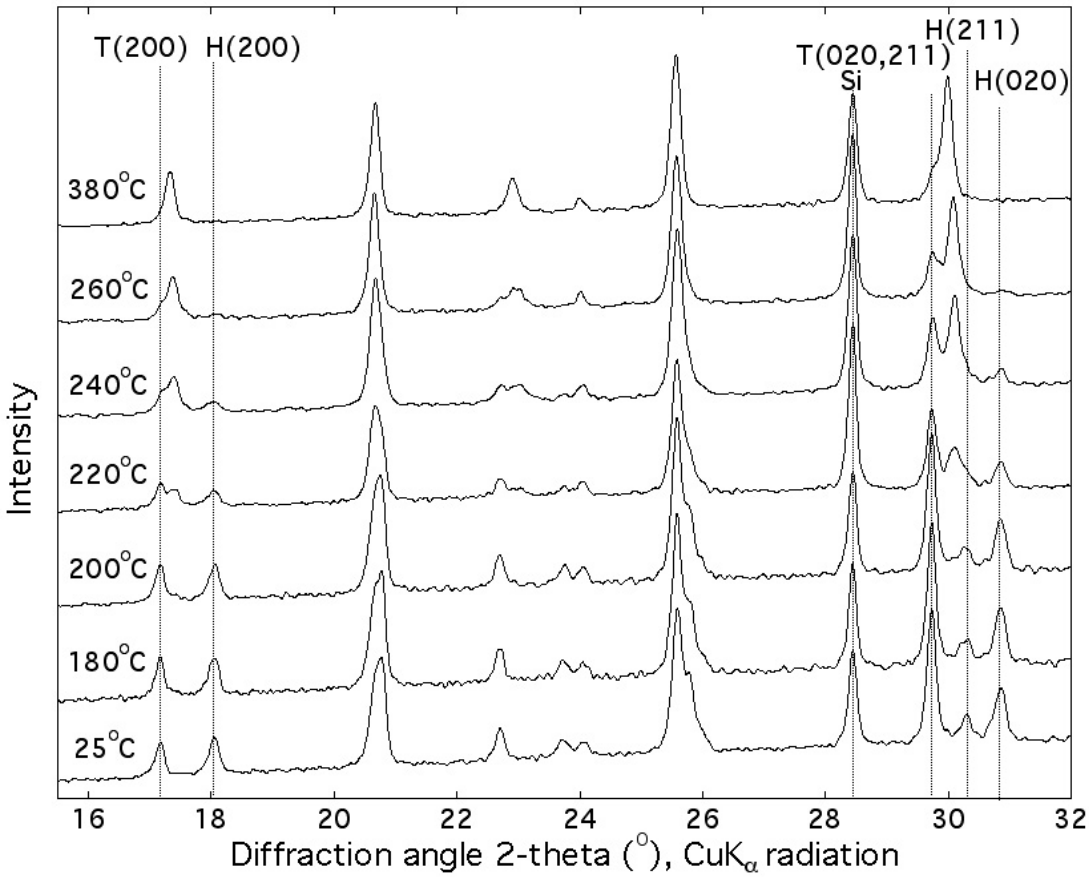

Figure 4.4: Series of XRD patterns for samples with lithium composition $x = 0.66$. Each sample was held at the noted temperature for 12 hours, and then quenched to room temperature.

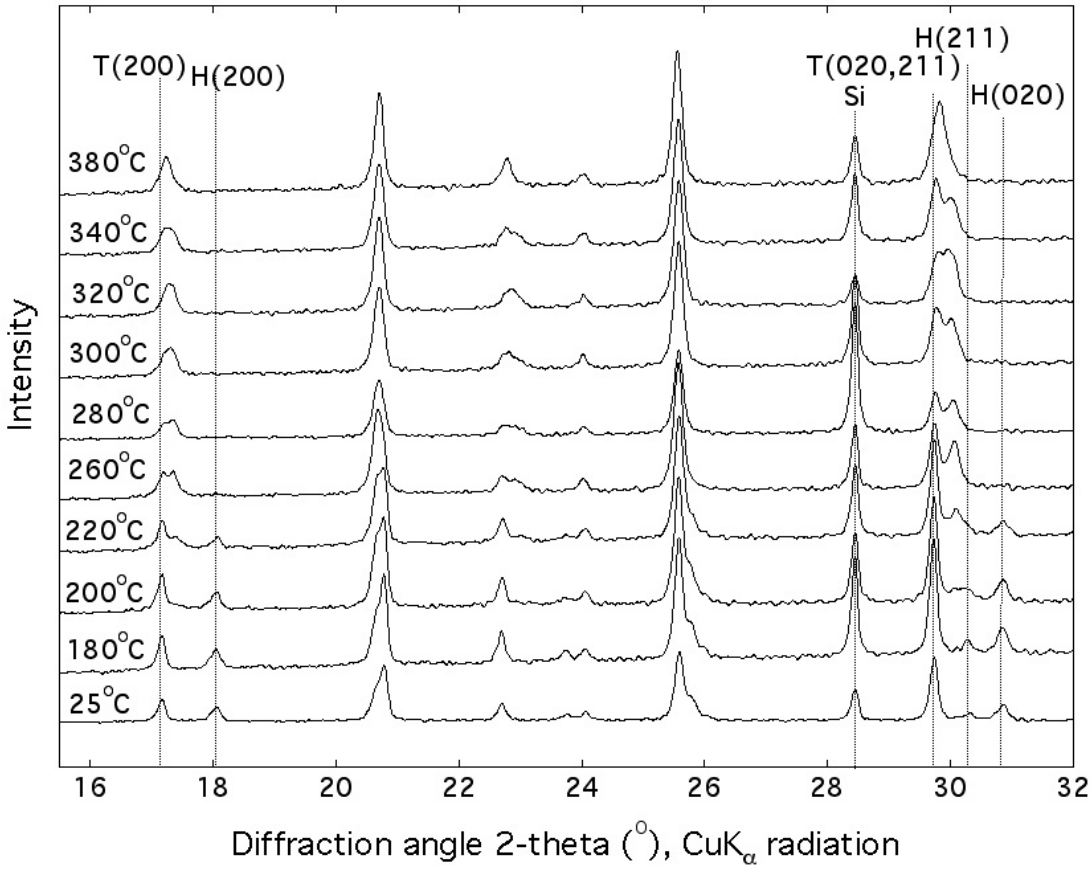

Figure 4.5: Series of XRD patterns for samples with lithium composition $x = 0.71$. Each sample was held at the noted temperature for 12 hours, and then quenched to room temperature.

The reversibility of the transformation to the disordered solid solution from heterosite and triphylite was confirmed in the course of assessing a phase diagram. The unmixing of the disordered solid solution is sluggish at room temperature, perhaps even imperceptible, but at higher temperatures the kinetics for unmixing are faster. Figure 4.6 shows a series of $x = 0.45$ samples that were heated to 380 °C for 2 hours to form the disordered solid solution, and then held at lower temperatures for unmixing. For temperatures of 220 °C and above, no unmixing is evident. However, some separation of 200, 020, and 211 diffraction peaks can be seen at 200 °C, 180 °C, and 160 °C. At these temperatures, complete unmixing does not occur within 12 hours.

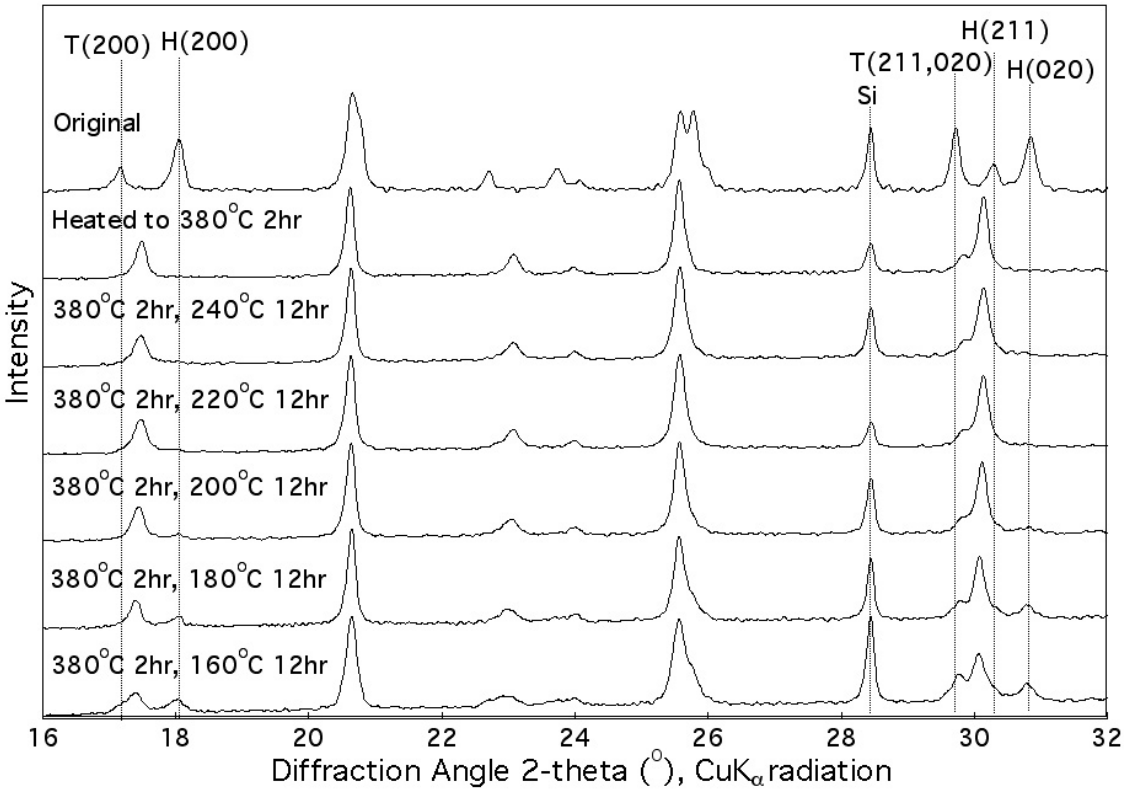

Figure 4.6: Comparison of XRD structure of $x = 0.45$ sample to sample heated to 380 °C for 2 hours, and to samples similarly heated and then cooled at the indicated temperatures. The cooling time was 12 hours. The separation of the samples into distinct phases is evident, especially upon cooling to 180 °C and 160 °C.

To further understand the thermodynamics of this system, we performed DSC measure-

ments with the $x = 0.47$ sample to determine enthalpies of mixing and unmixing. A DSC scan is shown in figure 4.7 for both heating and cooling. For a scanning rate of 5 °C/minute, the enthalpy of mixing was found to be 500 J/mol, with an onset temperature of approximately 200 °C. Upon cooling, the enthalpy of unmixing was found to be 700 J/mol, with an onset of approximately 170 °C. The lower enthalpy upon heating could be a result of gradual mixing over a wide temperature range. The data are consistent with the XRD results that show the formation of the disordered solid solution beginning at approximately 200 °C and continuing up to 300 °C. After the DSC measurement, the sample was analyzed again with XRD, showing a structure with 200 peaks separated, but not to the original triphylite and heterosite peak positions. (The sample had not decomposed to the original two phases.) If allowed longer times, the enthalpy of unmixing is expected to be higher than our reported values. Unfortunately, slower scans gave signals that were too weak to quantify.

4.4 Discussion

The transformation of the two phases, heterosite and triphylite, to a disordered solid solution along with the reverse transformation has been shown in my work. Many characteristics are similar to those reported by Delacourt et al. [48], but since our heat treatments were for longer times, with samples approaching equilibrium, we found some differences. The formation of the disordered solid solution occurs at temperatures of around 200 °C. At 220 °C, the samples with lithium concentrations of $x = 0.45$, 0.47, 0.66, and 0.71 all showed a mix of all three phases (heterosite, triphylite and disordered) after 12 hours of equilibration. For the $x = 0.45$ and 0.47 samples, the triphylite phase disappeared above 220 °C, leaving only a mix of heterosite and the disordered solid solution. For the $x = 0.71$ sample, the opposite occurred, with a disappearance of the heterosite phase. For the $x = 0.19$ sample, the XRD peak positions of the disordered solid solution varied with temperature, and the transformation was not complete until heating at 300 °C.

After formation of the disordered solid solution at high temperatures, unmixing occurs at temperatures below 200 °C. During unmixing, the heterosite and triphylite phases reform, with slightly shifted lattice parameters. These reformed phases indicate the equilib-

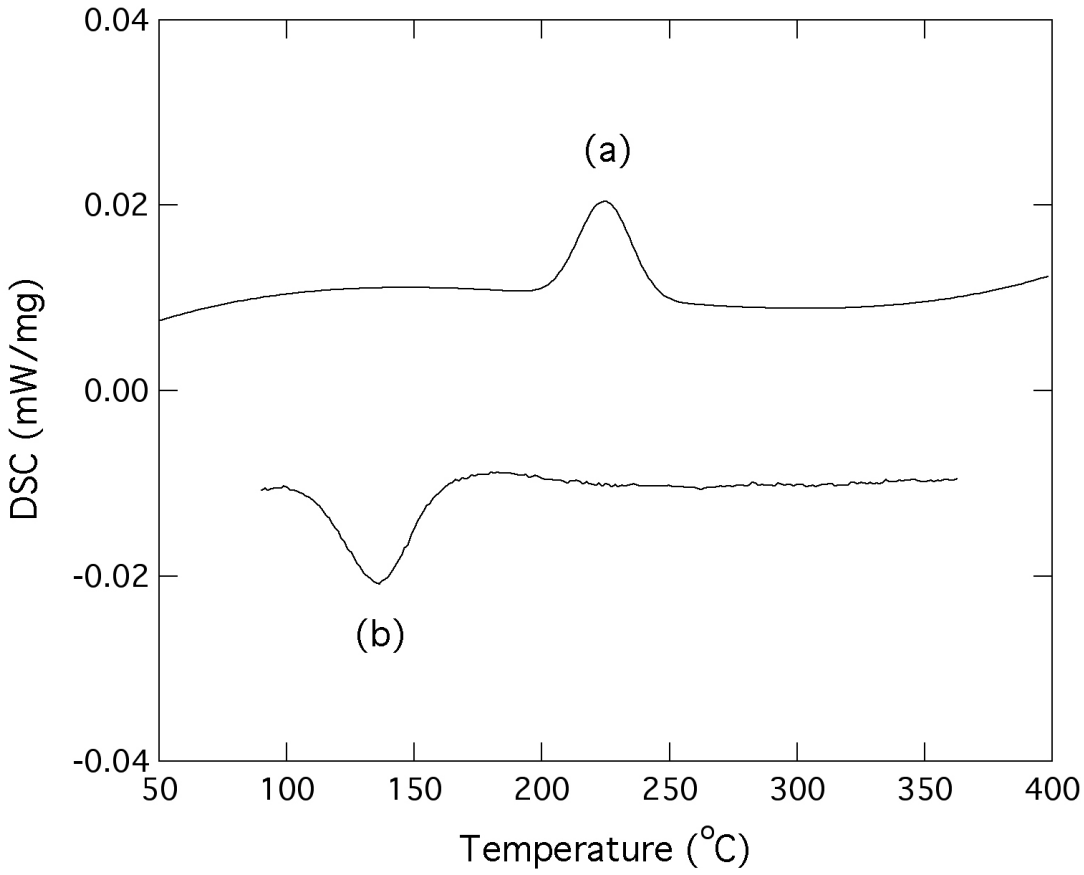

Figure 4.7: DSC scan of $Li_{0.47}FePO_4$ sample from room temperature to 400 °C. During heating, the endothermic peak (a) has a measured enthalpy of 500 J/mol. The exothermic peak (b) formed during cooling was measured as 700 J/mol.

rium structures at each temperature. Assuming the orthorhombic lattice constants follow Vegard's law as suggested by [48] and by the present results, the equilibrium compositions in the unmixed state were calculated for temperatures between 160 °C and 220 °C.

Our best estimate of the phase diagram is shown in figure 4.8. We propose that the phase diagram is an unmixing diagram with some characteristics of a eutectoid transformation. Rietveld refinement was used to determine phase fractions at each temperature. These results are plotted for several of the samples in figure 4.9. Our samples consisted of two phases at temperatures between 260 °C and 300 °C, so we were able to use the measured phase fractions and the lever rule to determine several points on the phase diagram.

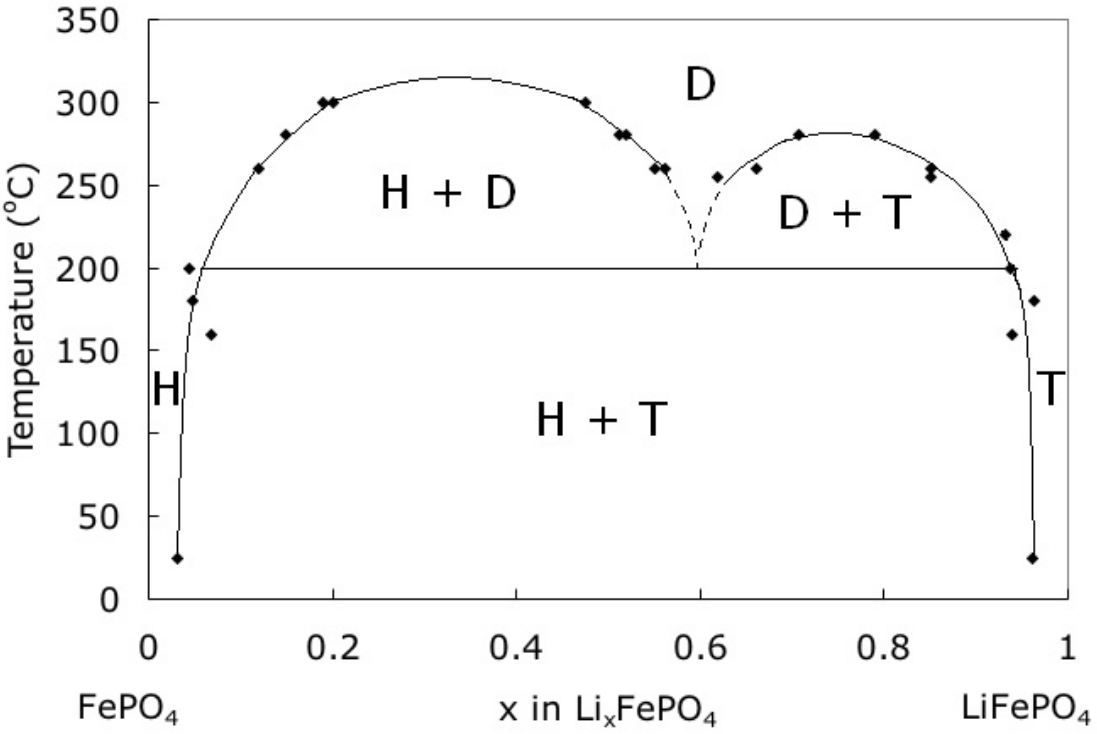

Figure 4.8: Phase diagram of $LiFePO_4$ (T, for triphylite) and $FePO_4$ (H, for heterosite) phases showing their merging to a solid solution (D, for disordered) in a eutectoid-like system. Data points at 25 °C are based on published work by Yamada et al. [50]. The eutectoid point is around the composition $x = 0.6$ and temperature 200 °C. Above 200 °C, mixtures of heterosite or triphylite and the disordered phase were seen up to around 300 °C. Above 300 °C, the disordered phase dominates.

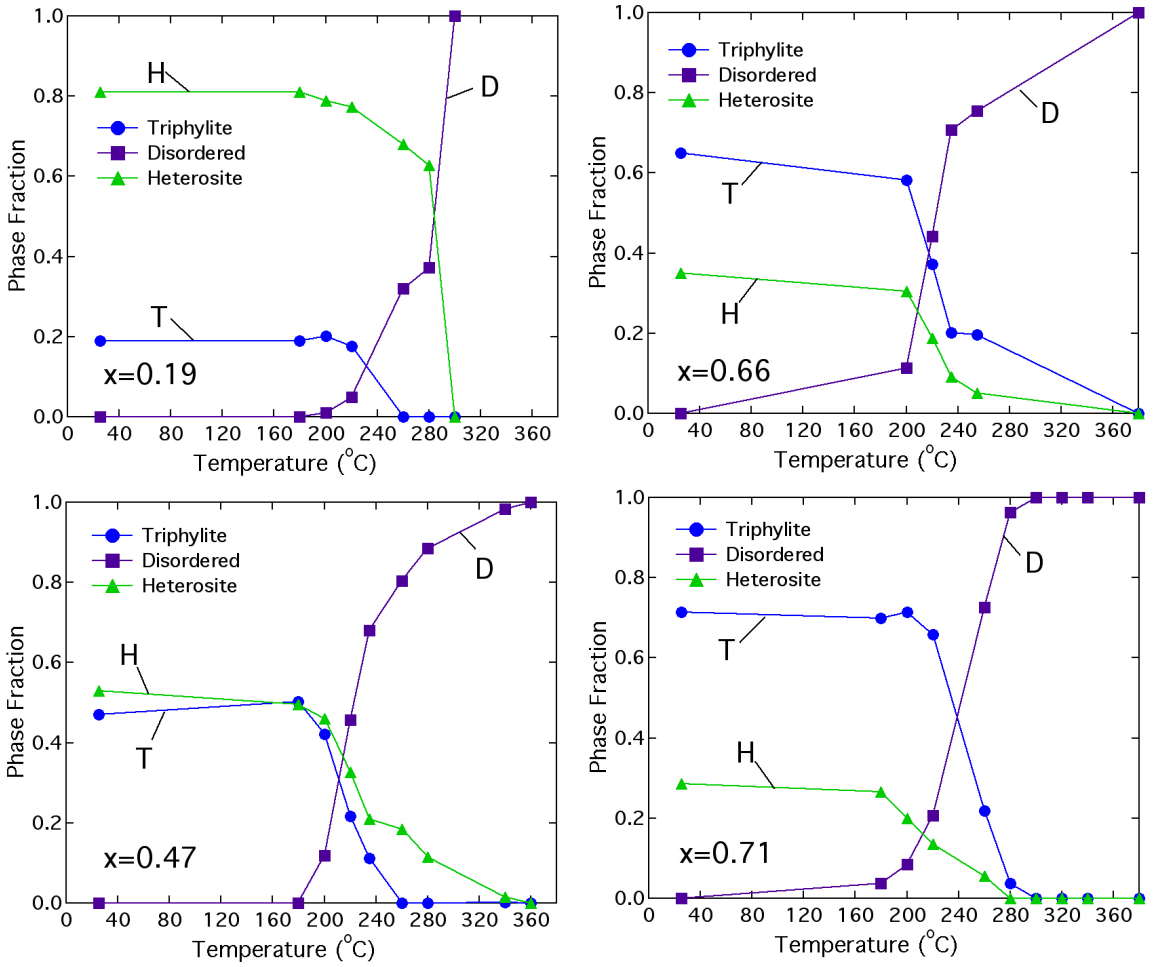

Figure 4.9: Phase fractions for two-phase mixtures heated at different temperatures are plotted for $x = 0.19$, 0.47, 0.66 and 0.71, as indicated. The triphylite phase (T), heterosite phase (H) and disordered phase (D) are also labeled. These phase fractions were determined by Rietveld refinement of samples held for 12 hours at each temperature.

For temperatures below 260 °C, equilibrium takes a much longer time, so it is difficult to pinpoint the phase boundary for the disordered phase near the composition $Li_{0.6}FePO_4$. For example, after several weeks at 220 °C, the samples with compositions $x = 0.47$, 0.66 and 0.71, were all mixtures of the heterosite, triphylite and disordered phases. However, after several weeks at 240 °C, a $Li_{0.66}FePO_4$ sample was nearly completely disordered. In general, samples near the $Li_{0.6}FePO_4$ composition required less time and lower temperatures to disorder compared to other compositions. In addition, after disordering, upon

holding at 200 °C, a $Li_{0.58}FePO_4$ sample does not unmix, while for compositions $x = 0.47$ and 0.71, unmixing occurs at 200 °C, suggesting stability of the disordered phase at lower temperatures for $x = 0.6$ compared to other states of lithiation (figure 4.10).

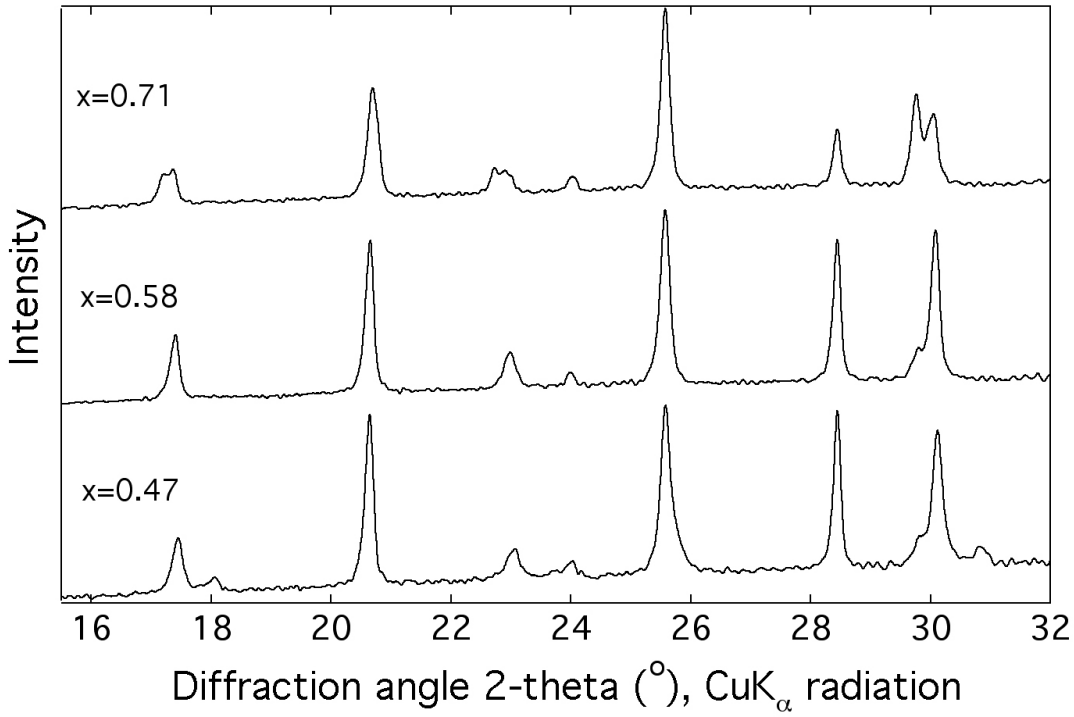

Figure 4.10: In order to test the stability of the disordered phase at different compositions, samples with compositions $x = 0.47$, 0.58 and 0.71 were heated to 380 °C for 2 hours, and then held at 200 °C for 36 hours. It is evident that the disordered phase is more stable at $x = 0.58$ compared to the other compositions shown.

Additional points at 220 °C and below were calculated based on the lattice parameters of reformation of heterosite and triphylite upon cooling the disordered solid solution. The data points of the phase diagram indicate that the eutectoid point occurs around composition $x = 0.6$ and temperature 200 °C.

The presence of narrow monophase regions near the stoichiometric end members of $LiFePO_4$ and $FePO_4$ at room temperature was first suggested by Yamada et al. [50]. In their study, the range of these monophase regions were from $x = 0.00$ to 0.03 and $x = 0.96$ to 1.00. It was later suggested that the material particle size affects the size of these

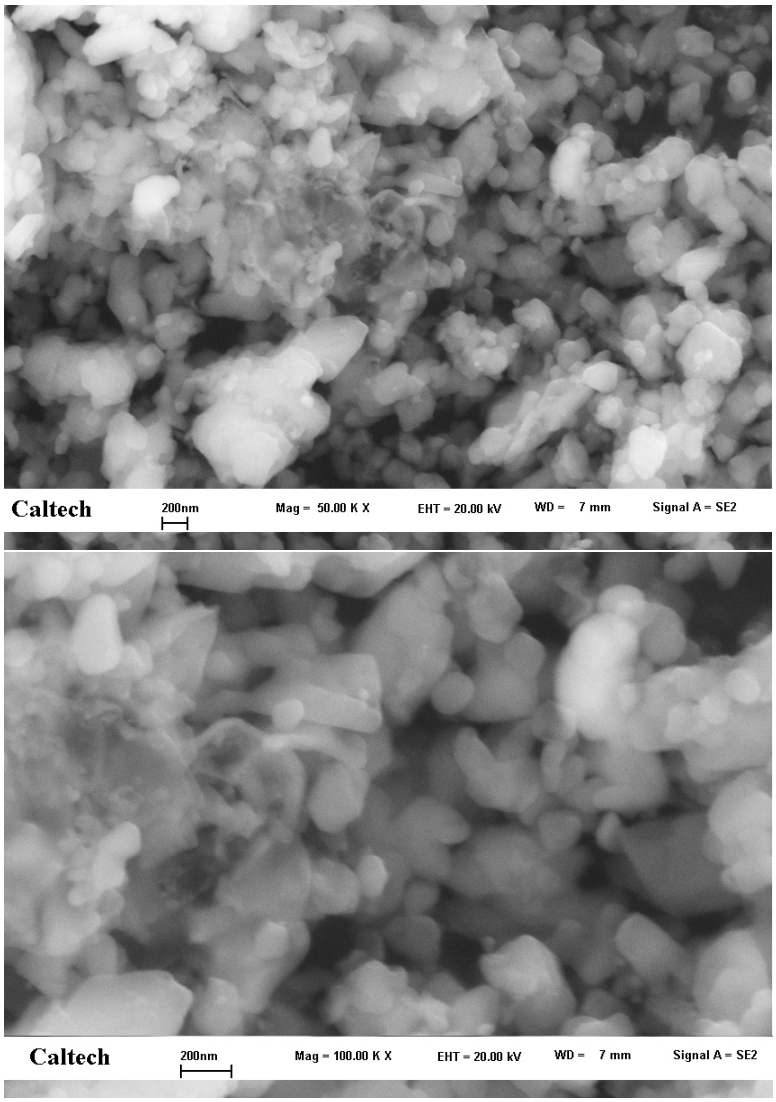

Figure 4.11: Shown are SEM images taken of the $LiFePO_4$ material used in this study, at 50,000× and 100,000× magnifications. Particles were approximately 200 nm in diameter, but there was some variation in size distribution.

monophase regions, with smaller particles having larger monophase regions and a smaller miscibility gap [52, 51]. However, larger differences are not seen until particles are below 50 nm in diameter. The material used in our study had an average particle size of 200 nm, as can be seen in figure 4.11. In Yamada's original study the particle sizes were between 100 and 200 nm [50]. Therefore, our sample should have similar monophase regions, and Yamada's results were added as data points to our phase diagram at room temperature, since compositions $x = 0.03$ and 0.96 mark a transition between a monophase region equivalent to a disordered solid solution phase and the two-phase mixture of heterosite plus triphylite. Figure 4.12 shows the 2-theta positions of the 200 diffractions for the $x = 0.45$ sample, plotted against heat treatment temperature. The plots include two sets of data: one shows the peak positions for the delithiated sample heated to each temperature, the second shows the peak positions after cooling for 12 hours, after first heating to the disordered state. The peak from the disordered solid solution first appears while the heterosite and triphylite peaks are still present, indicating a nucleation-and-growth type of phase transformation. For both heating and cooling, there is a spread of about 80 °C between the temperatures where the 200 peak from the disordered solid solution first appears, and the temperature where the transformation is complete. The unmixing from the disordered solid solution does not happen readily within 12 hours. However, it is evident that upon cooling, the samples unmix to form the original heterosite and triphylite compositions, in addition to the disordered solid solution.

Ordinarily, one expects two compositional ranges for disordered solid solutions in unmixing systems, and this is the case for the present phase diagram at temperatures below 200 °C. Conventional unmixing phase diagrams are readily understood from free energy vs. composition curves when interatomic interactions between unlike pairs of atoms are unfavorable. In the present system, the unmixing tendency is between Li ions and vacant sites, which have a repulsive effective interaction. At intermediate temperatures from 200 to 300 °C, however, the phase diagram of figure 4.8 shows three composition ranges for disordered solid solutions. The phase diagram of figure 4.8 implies two zones where the free energy of mixing is unfavorable, unlike the usual case of one maximum near the middle of the composition range. This is a characteristic of eutectoid transformations, where the

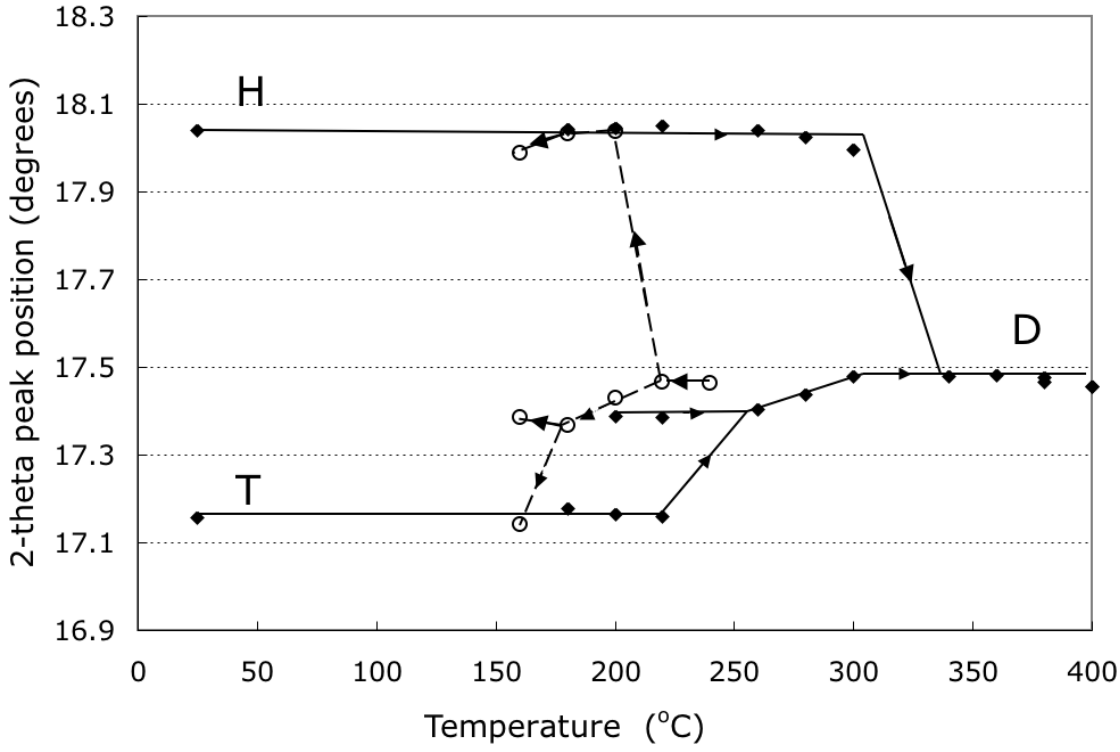

Figure 4.12: Positions of 200 peaks as a function of temperature. Data are shown for a sample with $x = 0.45$. The solid symbols (connected by solid lines) are peak positions from samples heated to the specified temperatures for 12 hours. The open symbols (connected by dotted lines) are from samples first heated to 380 °C for 2 hours, and then held at the specified temperatures for 12 hours.

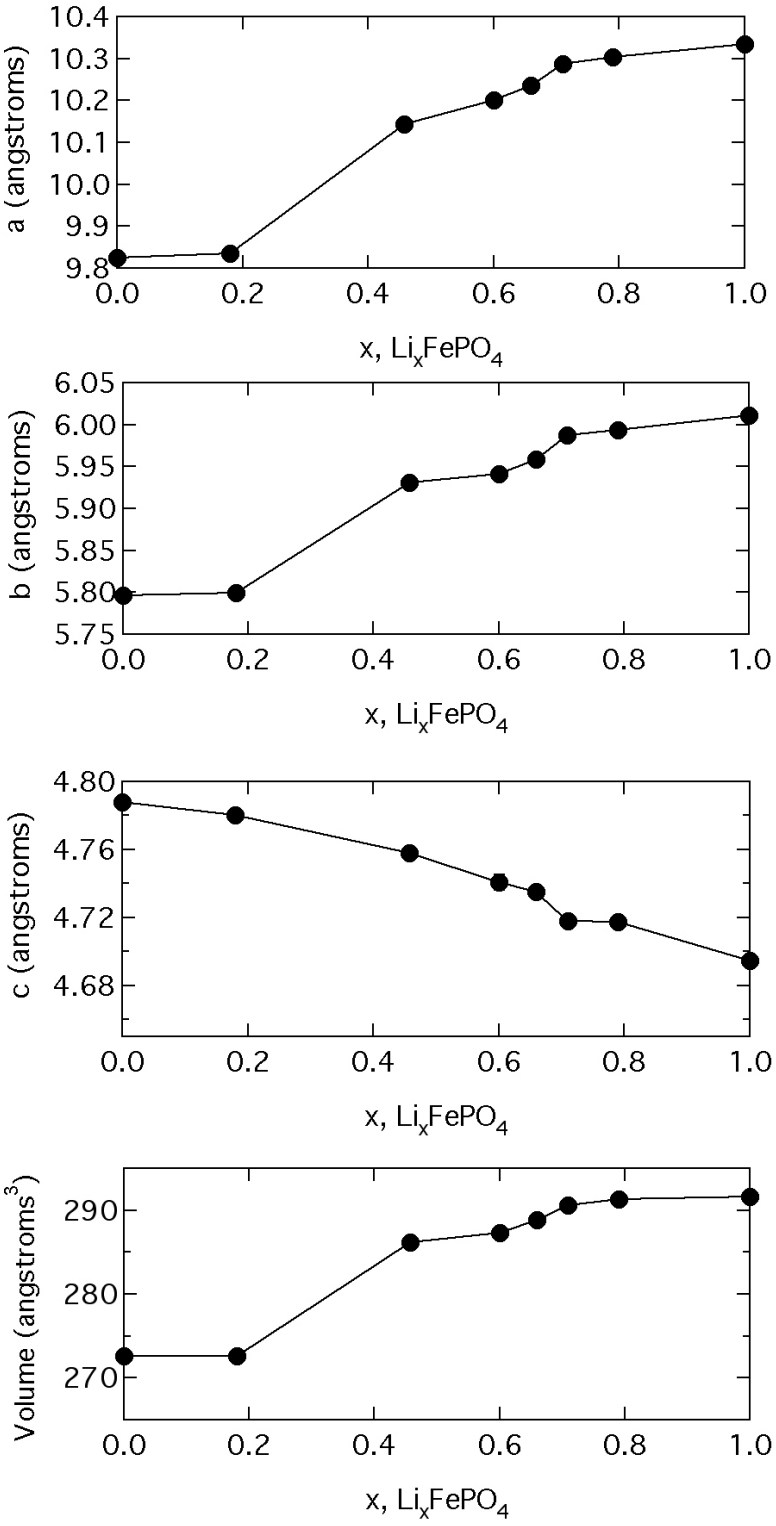

Figure 4.13: The a, b, and c parameters of the disordered solid solution phase are plotted for samples of different lithiation x. The unit cell volume is also plotted.

three phases are distinct. For the case of Li_xFePO_4, it is less obvious what distinguishes the phase with composition near $x = 0.6$. We have found no evidence for chemical ordering, although x-ray diffractometry is not highly sensitive to the spatial order of Li atoms. Delacourt et al. did not see any lithium ordering in the disordered phase either [49]. Changes in Li concentration do cause large changes in lattice parameter and alter the shape of the unit cell in Li_xFePO_4. Such differences would alter the enthalpy or entropy for unmixing, but it is not obvious how this would provide a local minimum in free energy near $x = 0.6$. Figure 4.13 shows the lattice parameters and unit cell volume for the disordered phase for samples of different lithiation x. The a, b, and c parameters vary gradually between $x =$ 0 and 1 compositions. The change is nearly linear for intermediate x ($0.2 < x < 0.8$) with not as steep of a change closer to $x = 0$ and 1.

The eutectoid-type behavior of the phase diagram could be due to the addition of two different entropy contributions (S_1 and S_2). In addition to the configurational entropy of lithium (S_1), another entropic term, with a sharper peak shape (S_2), could cause the disordered solid-solution phase stability at $x = 0.6$. Figure 4.14 depicts enthalpy (H), entropy (S), and Gibbs free energy (G) curves resulting in a eutectoid-type phase diagram. Free energy curves are drawn for multiple temperatures, increasing from T_1 to T_5, with the eutectoid temperature being T_4. We compared the vibrational entropy of two-phase and single-phase $Li_{0.6}FePO_4$ samples, and found no significant difference [58], so we do not expect the additional entropic term to be vibrational. Nor do we expect a magnetic entropy contribution to cause single-phase stability at $x = 0.6$. The stability of Li_xFePO_4 at $x = 0.6$ could be due to the configurational electronic entropy in the system. Zhou et al. proposed that the formation of a solid solution in this system is almost entirely driven by electronic rather than ionic configurational entropy [59]. In their first principles calculations, at the eutectoid point, they found that the mixing entropy driving the transition to the disordered solid solution is mostly electronic: 0.19 k_B from electronic entropy vs. 0.05 k_B from ionic (Li) entropy.

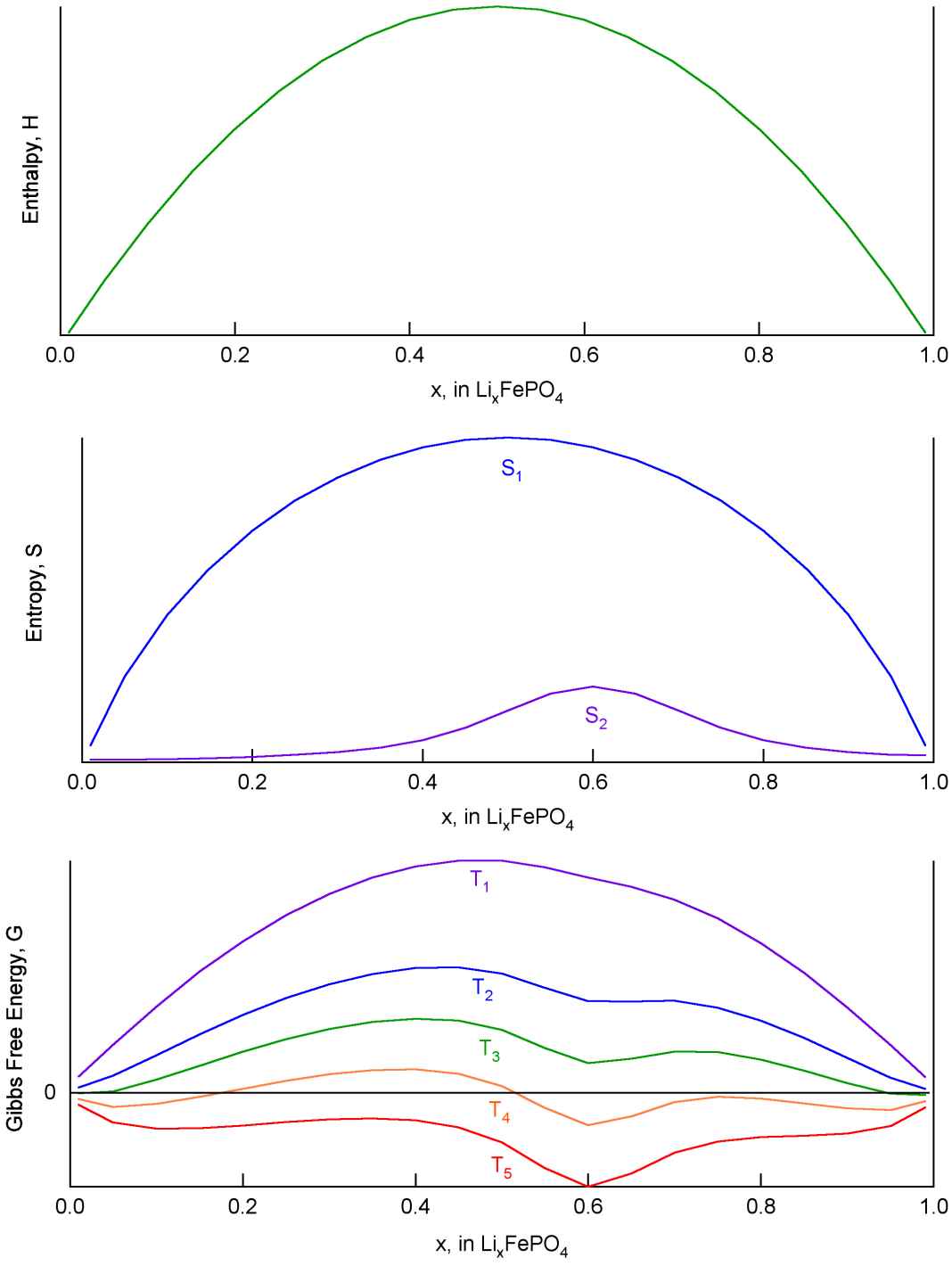

Figure 4.14: Drawings depicting the enthalpy (a), entropy (b), and Gibbs free energy (c) for a eutectoid-type Li_xFePO_4 phase system.

4.5 Conclusion

The mixing transformation from the heterosite and triphylite phases to a disordered solid solution of Li_xFePO_4 occurs around 200 °C. Between 200 and 300 °C, a mixture of disordered solid solution and either heterosite or triphylite is present. Above 300 °C, all Li_xFePO_4 samples equilibrated to form a disordered solid solution. The phase diagram for this system indicates that there are three compositional ranges where the disordered solid solution is stabilized at intermediate temperatures, near $x = 0.0$, 0.6 and 1.0. The heat of transformation was measured for an $x = 0.5$ sample, and is estimated to be at least 700 J/mol.

Chapter 5

Thermostability of Li_xFePO_4

5.1 Introduction

Much electrochemical work has been performed at elevated temperatures to investigate the stability of $LiFePO_4$ as an electrode material for a cathode, finding it quite suitable for service at high temperatures such as 60 °C [21, 25, 26]. In addition, thermal scanning measurements of $Li_{1.0}FePO_4$ and $Li_{0.0}FePO_4$ have been performed, showing that $LiFePO_4$ has a higher onset temperature and lower exothermic heat of decomposition than $LiCoO_2$, showing its advantageous safety characteristics [21, 22, 23]. However, the stability at specific states of lithiation for $0 < x < 1$ had not been investigated until recently. Delacourt et al. investigated Li_xFePO_4 at elevated temperatures, suggesting the existence of intermediate Li_xFePO_4 phases while heated to 350 °C [48]. Our additional work on the phase diagram of Li_xFePO_4 determined phase compositions and boundaries for temperatures from 25 °C to 400 °C [60]. The present work reports additional results on the thermostability of Li_xFePO_4 at temperatures between 400 and 800 °C, and at different states of lithiation between x = 0 and 1. Chemical delithiation of pure $LiFePO_4$, without the addition of binder or conductor, was performed with $K_2S_2O_8$. The stability of Li_xFePO_4 for various values of x was investigated by heating samples in an argon-filled tube furnace, and then analyzing them with x-ray diffraction (XRD) and Mössbauer spectrometry. Additional XRD measurements were performed *in situ* with a high temperature XRD stage purged with argon. Different iron phosphate phases were formed from $Li_{0.0}FePO_4$ when heated above 400 °C, and these changes may be irreversible due to gas loss, or possibly because these phases are more

stable than heterosite at low temperature. However, $Li_{1.0}FePO_4$ itself was very stable, and remained virtually unchanged after the heat treatment.

5.2 Experimental

5.2.1 Chemical Delithiation

$LiFePO_4$ material was prepared by Argonne National Laboratory, by a solid-state reaction consisting of a mixture of iron(II) oxalate $Fe(C_2O_4)\cdot 2H_2O$, ammonium dihydrogen phosphate $NH_4H_2PO_4$, and lithium carbonate Li_2CO_3 in the molar ratio (1:1:0.5) [61, 29]. This material was delithiated chemically by use of potassium persulfate ($K_2S_2O_8$) in an aqueous solution, as follows:

$$LiFePO_4 + \frac{y}{2}(K_2S_2O_8) \rightarrow (1-y)LiFePO_4 + yFePO_4 + \frac{y}{2}(Li_2SO_4 + K_2SO_4), \quad 0 < y < 1. \tag{5.1}$$

The $K_2S_2O_8/K_2SO_4$ redox couple has a Nernst standard potential of approximately 5 V vs. Li/Li^+, which is higher than the 3.5 V vs. Li/Li^+ for $Li_{0.0}FePO_4/Li_{1.0}FePO_4$ couple. Therefore, $K_2S_2O_8$ can oxidize $LiFePO_4$ to full delithiation. An aqueous solution of $K_2S_2O_8$ and $LiFePO_4$ was mixed at ambient temperature for 24 hours, allowing equilibrium to be reached. By altering the molar ratio of $K_2S_2O_8/LiFePO_4$, samples with different amounts of lithium were prepared. Table 5.1 shows the molar ratios, along with the resulting x in Li_xFePO_4 for the samples, obtained from the experimental methods described below:

		Lithiation, x, Measured by Each Method		
Sample Label	$LiFePO_4$/ $K_2S_2O_8$ Ratio	ICP	Mössbauer	XRD
$x = 0.00$	2.00	0.01	0.00	0.00
$x = 0.20$	2.66	—	0.21	0.20
$x = 0.48$	4.00	0.43	0.44	0.48
$x = 0.71$	8.00	—	0.69	0.71
$x = 1.00$	no $K_2S_2O_8$	0.99	1.00	1.00

Table 5.1: The state of lithiation, x in Li_xFePO_4, was measured by three different methods for five samples. The results were similar for all three methods. The molar ratio of $LiFePO_4/K_2S_2O_8$ used in the sample preparation is also shown.

5.2.2 Heat Treatment

Three different methods were used for heat treating the samples. In the first, the samples were heat treated in a tube furnace, with an argon flow to create an inert environment. The samples were placed in the tube furnace, in a ceramic container, and then quickly heated up to the specified temperature, held at that temperature for one hour, and then cooled to room temperature in the furnace. Since the samples were furnace cooled, they were slowly cooled down, possibly allowing for atomic rearrangement to more thermodynamically stable phases. In the second method, samples were sealed in quartz glass ampoules in vacuum, after first purging several times with argon. These samples were heated for one hour to a specified temperature and then quenched in water, without breaking the ampoule. This quick cooling was more promising for keeping intact the thermodynamically stable phases at the heat treatment temperature. Finally, x-ray diffraction measurements were performed *in situ* using a high temperature stage, between room temperature and 800 °C, at 100 °C increments.

5.2.3 X-ray Diffraction, Mössbauer Spectrometry, Intercoupled Plasma Emission Spectroscopy

X-ray diffractometers with Cu K_α radiation (Rigaku Co. R2000 and PANalytical X'Pert PRO X'Celerator) were used to analyze and identify the phases of the material. After phase identification, Rietveld analysis was used to determine phase fractions present in the samples, by using Xpert Plus software (PANalytical). For *in situ* high temperature XRD measurements a high temperature stage (HTK-1200) was used on the PANalytical diffractometer. The sample chamber was filled with argon gas during the experiments, and the sample was heated in increments of 100 °C. The temperature was ramped at a rate of 5 °C per minute and then after 30 minutes at each temperature, the XRD pattern was then measured by a 50-minute scan.

^{57}Fe Mössbauer spectra were obtained in transmission geometry with a ^{57}Co γ-ray source. The velocity calibration was performed using the measurements taken from an α-Fe sample at room temperature. The spectra were fit to Lorentzian peaks, with the Igor Pro

multipeak fitting package, and the integrated areas of doublets for Fe^{2+} or Fe^{3+} valencies were measured. Intercoupled plasma emission spectroscopy (ICP) was used to determine Li/Fe ratios to deduce compositional makeup of several samples before heat treatment, using a Jobin Yvon JY 2000 ICP spectrometer. ICP measurements matched well with XRD and Mössbauer results.

5.2.4 Electrochemical Performance

The performance of samples in electrochemical cells was evaluated using coin-type cells (2034) with lithium metal anodes. The cathodes were made of a mixture of active material:acetylene black:polyvinylidene fluoride (PVDF) with weight ratio 80:15:5, and the electrolyte was a 1.2 M $LiPF_6$ EC:DEC 3:7 solution. The material was mixed with carbon by ball milling. The method was similar to that used by Masquelier in other iron phosphate electrode preparation [62]. The charge-discharge cycling was performed at room temperature between 2.5 and 4.0 V.

5.3 Results

Five samples prepared by chemical delithiation were studied. The states of lithiation of the Li_xFePO_4 were $x = 0.00$, 0.20, 0.48, 0.71, and 1.00. For Li_xFePO_4, x signifies the material lithiation and reasonably matches the fraction of material in the triphylite phase. Each of the samples was analyzed by XRD, Mössbauer spectrometry and ICP spectroscopy. Figure 2.2 (in section 2.2), compares the XRD patterns for all five samples, labeled $x = 1.00$ to $x = 0.00$. Sample $x = 1.00$ was the original $LiFePO_4$ material, while $x = 0.00$ was a fully delithiated $FePO_4$ sample. As expected, the XRD measurements showed that the starting material, $LiFePO_4$, began as the triphylite phase. The structure refinement gave the crystal parameters of the orthorhombic structure listed in table 5.2, in agreement with known data [13, 31, 50]. After delithiation, a two-phase mixture was observed, including triphylite and another orthorhombic phase, heterosite, which has the composition $FePO_4$. The heterosite crystal parameters are also given in table 5.2, and match the values found in the literature [13, 31, 50]. The lithiation of each material was obtained from Rietveld refinement of the

XRD patterns. The triphylite and heterosite phases can also be distinguished by Mössbauer spectrometry. The iron valency varies between the two phases, with Fe^{2+} in the triphylite phase, and Fe^{3+} in the heterosite phase. The phase fractions were determined by comparing the integrated areas of the doublets corresponding to Fe^{2+} and Fe^{3+} for $LiFePO_4$ and $FePO_4$. Figure 2.3 (in section 2.2) shows the Mössbauer spectra of the series of samples. The phase fractions determined by XRD and Mössbauer spectrometry were in good agreement with each other and with the chemical compositions measured by ICP analysis, assuming these two phases were present on the basis of the lithium concentration. Table 5.1 shows the state of charge of each of the five samples, and the correspondence between the results measured by the three different techniques.

					Lattice Parameters (Ang)			Angles			
	Mineral Name	Crystal System	Space Group	Iron Valency	a	b	c	α	β	γ	Reference
$LiFePO_4$	Triphylite	Orthorhombic	Pnma	Fe^{2+}	10.322	6.004	4.689	90	90	90	current work
$FePO_4$	Heterosite	Orthorhombic	Pnma	Fe^{3+}	9.809	5.786	4.780	90	90	90	current work
$Fe_7(PO_4)_6$	Iron phosphate	Triclinic	P-1	3 Fe^{2+}, 4 Fe^{3+}	6.314	7.967	9.546	66.9	68.9	78.9	[63, 64]
$Fe_2P_2O_7$	Iron phosphate	Triclinic	P-1	Fe^{2+}	5.517	5.255	4.488	98.7	98.3	103.81	[65, 66]
$FePO_4$, hex	Rodolicoite	Hexagonal	P321	Fe^{3+}	5.021	5.021	11.229	90	90	120	[67]

Table 5.2: Crystal systems, space groups, iron valency, and lattice parameters for phases resulting due to heat treatment of Li_xFePO_4.

Heat treatments were then performed on each of the samples. The heat treatments were 60 minutes at the specified temperatures in an argon atmosphere, followed by furnace cooling. The fully lithiated sample, $Li_{1.0}FePO_4$, was very stable upon heating in an inert argon environment. Figure 5.1 shows that triphylite is stable after heating to 400 °C, 500 °C, 600 °C, or 800 °C. The XRD patterns for $Li_{0.48}FePO_4$ for various heat treatments are shown in figure 5.2. The sample was unstable upon heating to 400 °C and above. At 400 °C, the intermediate disordered solid solution phase forms, and was measured from a sample quenched from that temperature. However, if allowed to slowly cool down, some phase separation occurs; the lithium separates somewhat into the triphylite and heterosite phases, although it can be seen that this separation was not completed. As the sample was heated above 400 °C, the delithiated heterosite phase disappeared and formed two other phases. On the other hand, the lithiated portion of the material, which was composed of the triphylite

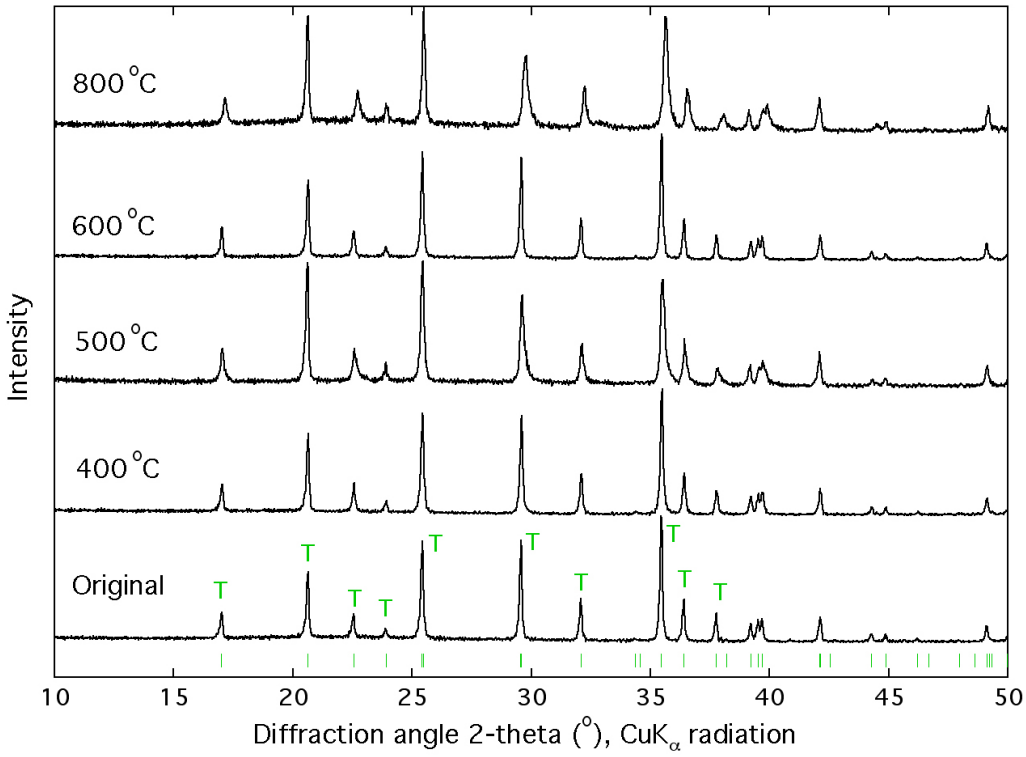

Figure 5.1: XRD spectra of $Li_{1.0}FePO_4$ sample after heat treatments at the indicated temperatures. Peaks from the triphylite phase are indicated (T), as well as the vertical bars below.

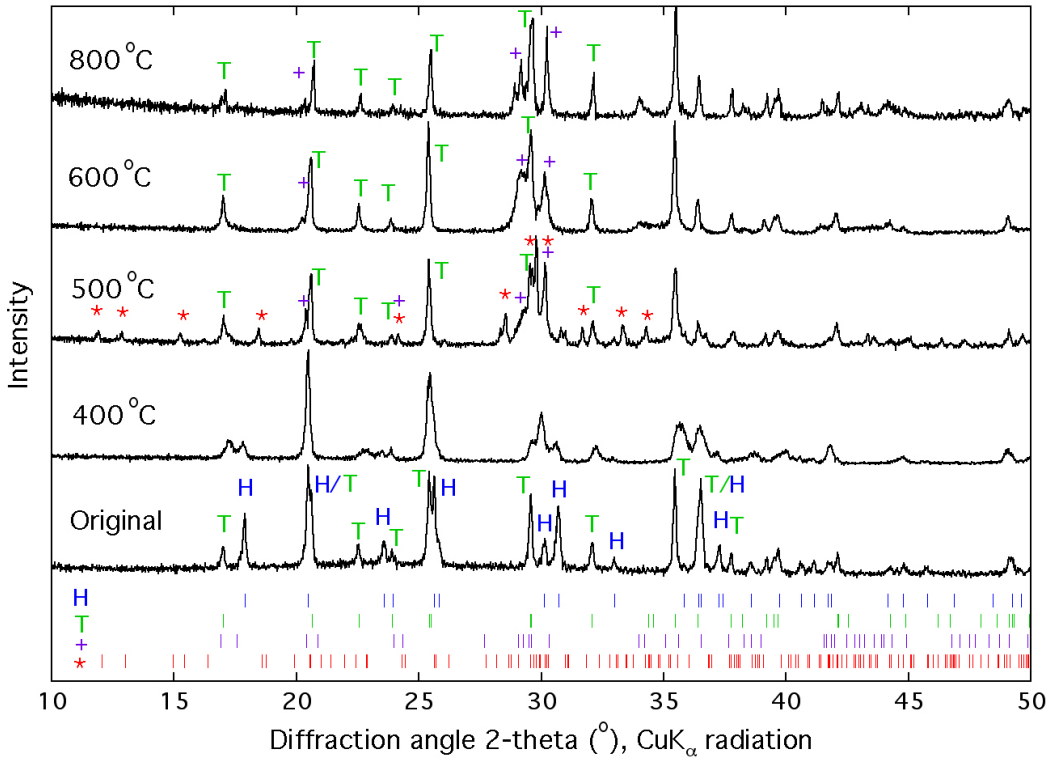

Figure 5.2: XRD spectra of $Li_{0.48}FePO_4$ sample after heat treatments at the indicated temperatures. Peaks from different phases are indicated: T: triphylite, H: heterosite, *: $Fe_7(PO_4)_6$, and +: $Fe_2P_2O_7$.

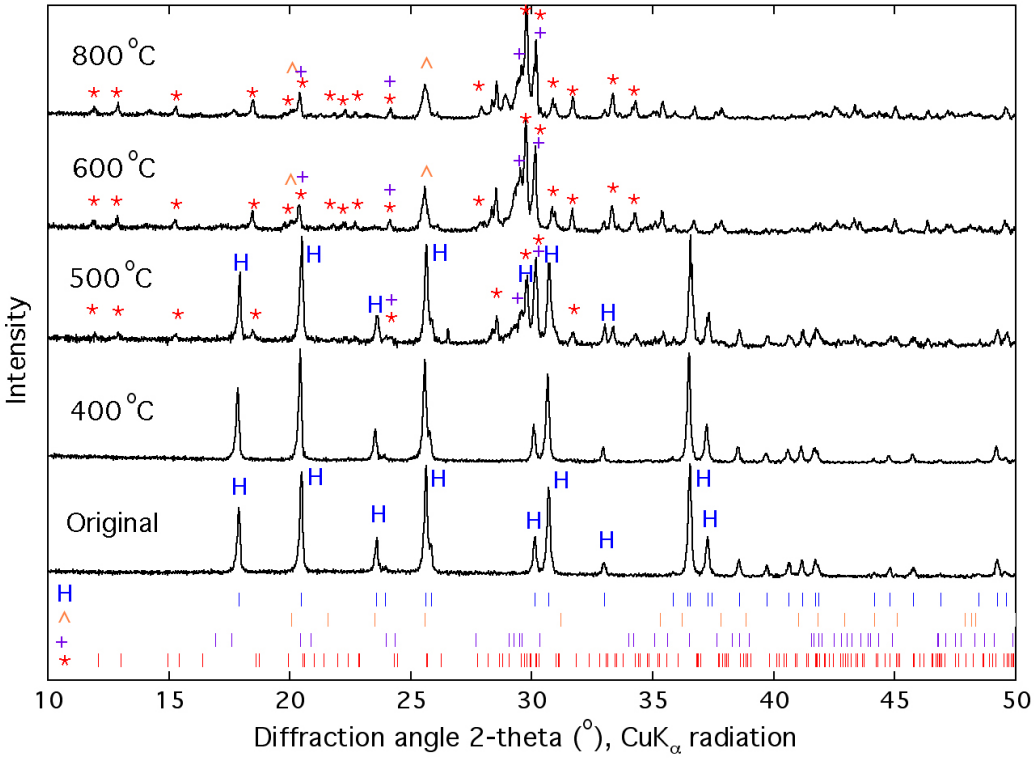

Figure 5.3: XRD spectra of $Li_{0.0}FePO_4$ sample after heat treatments at the indicated temperatures. Peaks from different phases are indicated: H: heterosite, *: $Fe_7(PO_4)_6$, +: $Fe_2P_2O_7$, and ∧: $FePO_4$ hexagonal.

phase, seemed to be stable upon heating, just as for the $Li_{1.0}FePO_4$ sample. The delithiated portion of the sample formed the phase $Fe_7(PO_4)_6$ [63, 64], which includes many diffraction peaks due to the large size of its primitive unit cell. Samples that were heated to higher temperatures, 600 °C or 800 °C, tended to predominantly form another phase, $Fe_2P_2O_7$ [65, 66]. Finally, $Li_{0.0}FePO_4$ formed a mixture of phases upon heating. It was stable up to 400 °C, but after heat treatment at 500 °C, the $Fe_7(PO_4)_6$ and $Fe_2P_2O_7$ phases appeared. Heat treatment to 600 °C and 800 °C seemed to form a three-phase mixture, which also included another $FePO_4$ phase, a hexagonal structure called rodolicoite [67]. XRD patterns for $Li_{0.0}FePO_4$ after these heat treatments are shown in figure 5.3.

Mössbauer spectra of heat treated samples were also measured, and are compared in figure 5.4. The Mössbauer spectra showed good agreement with the XRD results for the fraction of Fe^{2+} and Fe^{3+} present in each sample. Table 5.3 shows the calculated Fe^{2+} valency breakdown for each sample, comparing XRD and Mössbauer spectrometry measurements.

	Original Sample		600 °C Heat Treated		800 °C Heat Treated	
Sample Label	XRD	Mössbauer	XRD	Mössbauer	XRD	Mössbauer
$x = 0.00$	0	0	54	51	56	55
$x = 0.20$	20	21	82	79	84	79
$x = 0.48$	48	44	100	100	100	100
$x = 0.71$	71	69	100	100	100	100
$x = 1.00$	100	100	100	100	100	100

Table 5.3: Calculated Fe^{2+} percentage in each sample, as measured by XRD and Mössbauer.

Additional x-ray diffractometry work was performed using a high temperature stage (HTK-1200) on a PANalytical diffractometer. The sample chamber was filled with argon gas during the experiments, and the sample was heated in increments of 100 °C to check for phase stability of $Li_{0.0}FePO_4$ or $Li_{0.48}FePO_4$ samples. For the $Li_{0.0}FePO_4$ sample, the heterosite phase was stable up to 400 °C, in agreement with earlier measurements. Between 500 and 800 °C, the same phases were formed, as discussed above and as shown in figure 5.3. However, the ratio of the composition differed at 600 °C and greater, the sample was mostly composed of the hexagonal $FePO_4$ phase. For the $Li_{0.48}FePO_4$ sample, structural changes

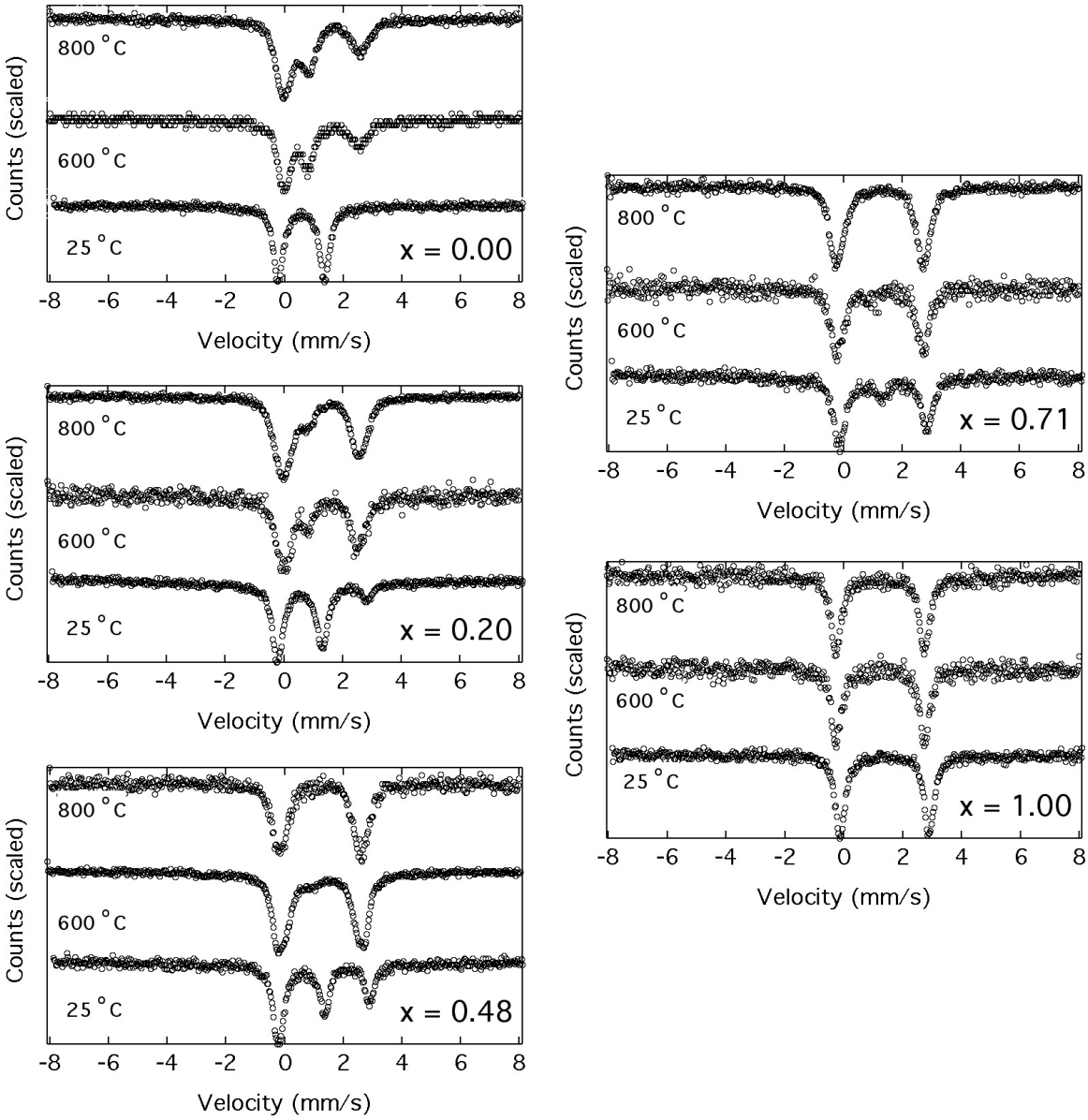

Figure 5.4: Mössbauer spectra of different compositions, $x = 0.00$, 0.20, 0.48, 0.71, and 1.00, as labeled. All spectra were measured at room temperature. Included are spectra of the original samples (labeled 25 °C) as well as samples after a one-hour heat treatment at 600 °C or 800 °C followed by furnace cooling.

were visible even as low as 200 °C. For 300-400 °C the disordered solid solution Li_xFePO_4 was present, similar to Delacourt's work [48]. At 500 °C and above, the triphylite phase reemerged, in addition to $Fe_2P_2O_7$ and $Fe_7(PO_4)_6$, in agreement with our results described earlier.

To find out whether the phases formed during heat treatment contribute to the capacity fade of a $LiFePO_4$ cell, we tested the electrochemical performance of the new phases. The intent was to see if lithium could be inserted into and extracted out of their structures. The samples from heat treatments were used for making electrochemical cells. The fully delithiated sample after heat treatment at 800 °C was tested. It has a composition of 52% $Fe_7(PO_4)_6$, and 48% $Fe_2P_2O_7$, and a small amount of rodolicoite. The resulting coin cells did not have much capacity at all, only about 5 mAh/g. Samples of $Li_{0.48}FePO_4$ heat treated at 600 °C were also tested for electrochemical performance. This material contained 52% $LiFePO_4$ and 48% $Fe_2P_2O_7$. The coin cells with this material showed only 35 mAh/g specific capacity, not enough to account for the 52% $LiFePO_4$ in the sample.

5.4 Discussion

After preparation at elevated temperature, $LiFePO_4$ has the triphylite structure. This triphylite phase is stable at room temperature, and remains stable in an argon environment after heating at intermediate temperatures up to 800 °C. In delithiated material, other phases were observed after heating, and appear to be the thermodynamically stable structures for the composition Li_xFePO_4 when $x < 1$.

When lithium is extracted from $LiFePO_4$ at room temperature, regions of triphylite transform to heterosite, $FePO_4$. There appear to be no other phases, such as amorphous phases invisible to x-ray diffractometry, because the fraction of heterosite determined by XRD follows accurately the fraction of Fe^{3+} measured by Mössbauer spectrometry. The crystal structures of heterosite and triphylite are similar, and share a common framework of Fe atoms and PO_4 groups. Lithium extraction from the triphylite produces the heterosite structure without further atom rearrangements, and the reverse lithiation reaction seems to be largely reversible at room temperature, as has been reported by many groups in the

recent past. This does not mean, however, that the heterosite is the thermodynamically stable phase at room temperature. The evidence from the present research is that heterosite is only metastable.

For mixed phase compositions at room temperature, where $0 < x < 1$, the peak widths of both triphylite and heterosite diffractions are broadened. Figure 5.5 shows that in mixed-phase compositions, all three diffraction peaks investigated (200, 311, and 211/020) were broadened. These diffraction peaks were specifically chosen because of their relative high intensities and since they do not overlap with other peaks. The broadening can be attributed to increased strain of each phase when in a two phase mixture, or can indicate that in such a mixture each phase has smaller crystallite sizes and less structural coherence. This peak broadening can explain the driving force for atom rearrangement to form an intermediary phase between the heterosite and triphylite phases. Heating to temperatures between 200 and 400 °C, thus increasing atom mobility, allows the formation of this intermediary phase. When heated above 400 °C, additional phase transformation occurs for the delithiated portions of the material, due to their instability.

After the partially delithiated materials were heated to temperatures above 400 °C, the heterosite transformed to one of the three phases: $Fe_7(PO_4)_6$, $Fe_2P_2O_7$ or hexagonal $FePO_4$. Table 5.2 presents some properties of these phases. The fraction of phases formed at 600 °C are presented in figure 5.6 for various lithium concentrations in the material before heating. After heating to 600 °C, samples with more lithium tend to form more $Fe_2P_2O_7$ and less $Fe_7(PO_4)_6$ than samples having less lithium. Figure 5.7 presents an overview of the phases observed in all materials at all temperatures, along with table 5.4, which outlines the percentage of each phase found after each heat treatment.

There was no evidence for reversibility of these heterosite decomposition reactions (i.e., we did not observe any reformation of heterosite upon cooling). It appears that these product phases are more stable than heterosite, and will form if atom mobility is induced by temperature. Transformations of heterosite to the phases $Fe_7(PO_4)_6$ or $Fe_2P_2O_7$ involves the loss of oxygen or PO_4 groups from the structure, as is possible for an open system, perhaps especially at low partial pressures of oxygen. It is relevant to note that heterosite with an iron-rich composition of $(Fe,Mn)PO_4$ is a mineral found in nature, and it could

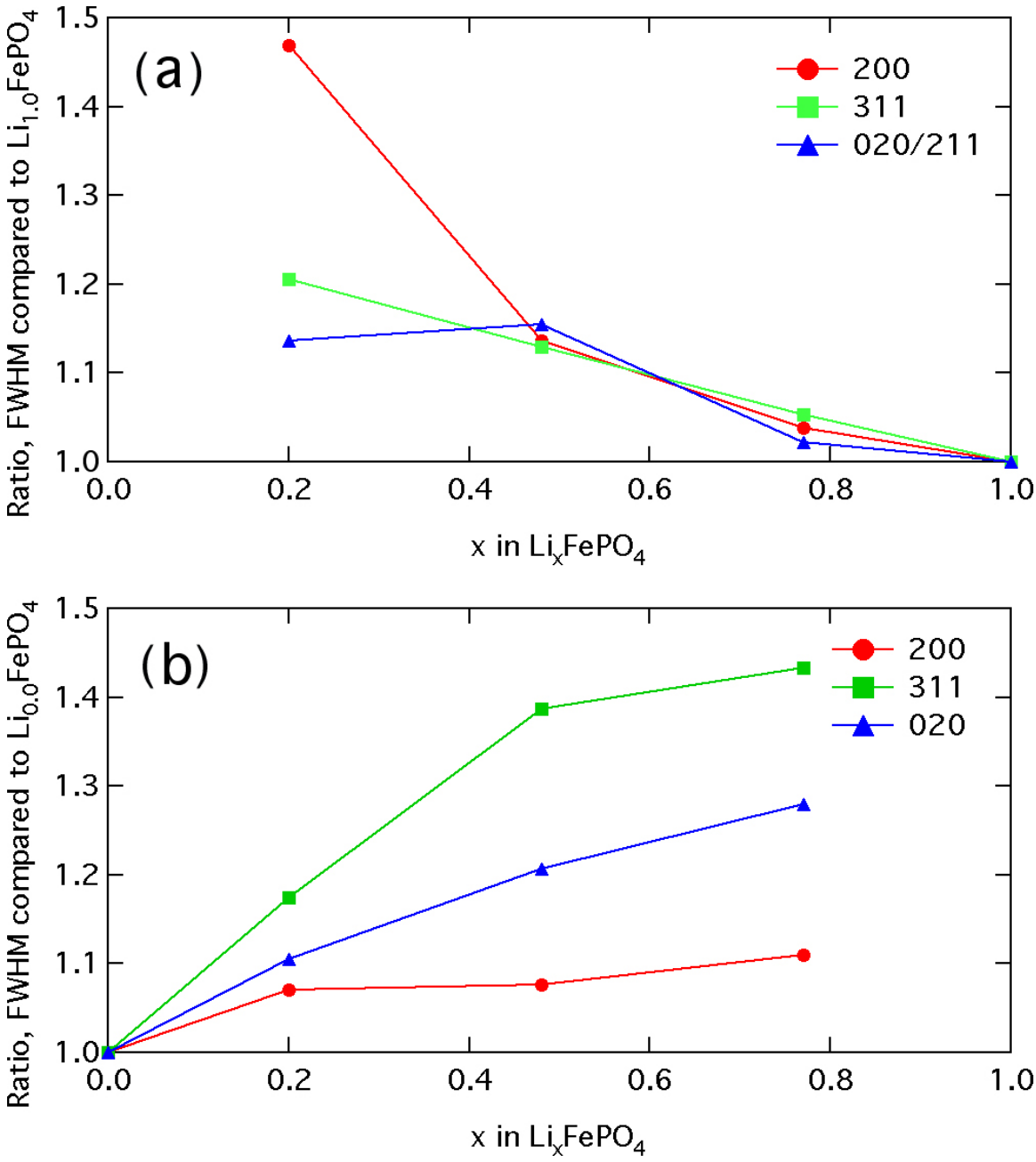

Figure 5.5: Ratio of FWHM for Li_xFePO_4 sample compared to pure phase, $Li_{1.0}FePO_4$ for triphylite (a) and $Li_{0.0}FePO_4$ for heterosite (b).

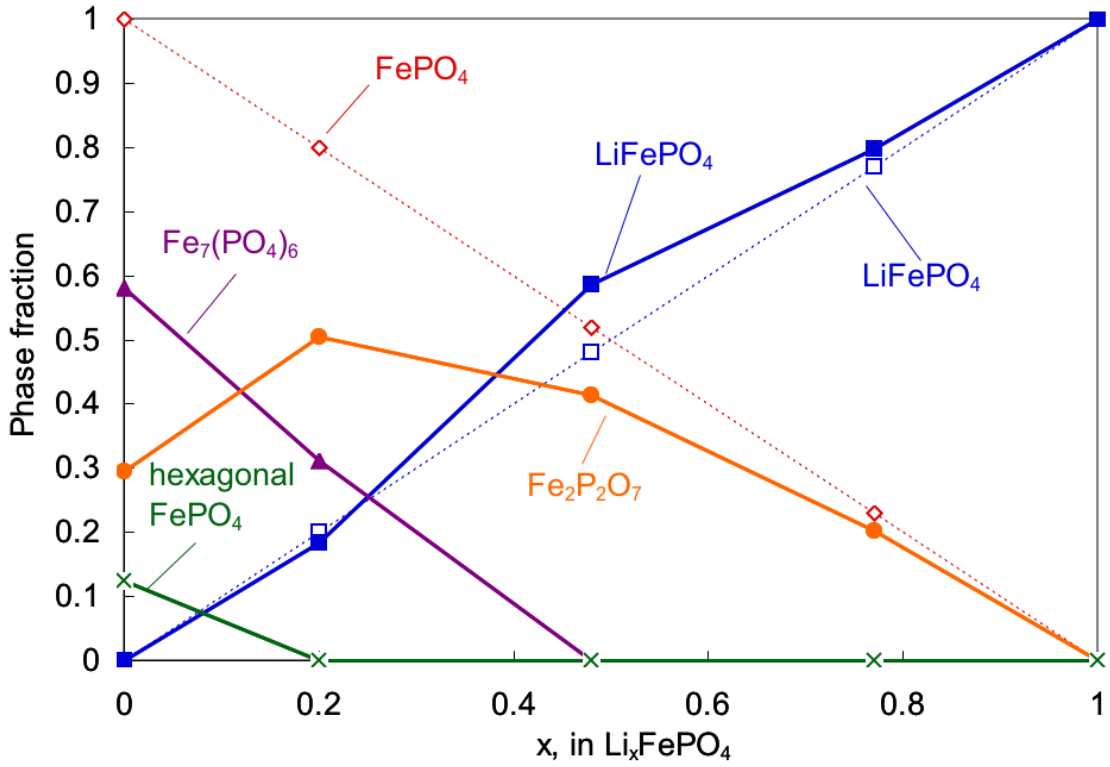

Figure 5.6: Comparison of phase composition before and after heat treatment at 600 °C. The dashed lines and open symbols correspond to the original phase fractions versus x, the sample lithiation, while the solid lines and dark symbols correspond to phase fractions after heating. The phases are labeled, including: triphylite, heterosite, $Fe_7(PO_4)_6$, $Fe_2P_2O_7$, and hexagonal $FePO_4$.

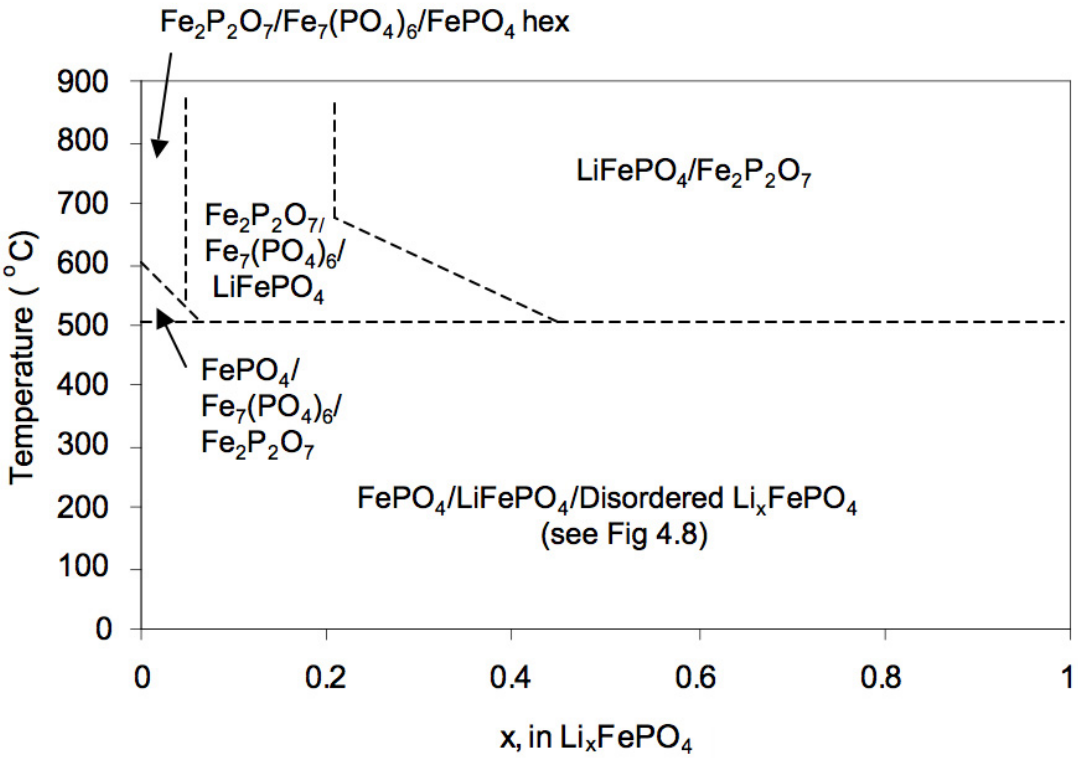

Figure 5.7: Phases found in Li_xFePO_4 material, after heat treatment at various temperatures.

Heat Treatment, Furnace Cooled						
Heat Treatment Temperature (°C)	x	$LiFePO_4$	$FePO_4$	$Fe_7(PO_4)_6$	$Fe_2P_2O_7$	$FePO_4$ hex
500	1.00	100	0	0	0	0
	0.71	80	0	5	14	0
	0.48	45	0	36	19	0
	0.20	17	0	62	21	0
	0.00	0	54	29	17	0
600	1.00	100	0	0	0	0
	0.71	73	5	3	19	0
	0.48	57	0	0	43	0
	0.20	19	0	32	50	0
	0.00	0	0	62	28	10
800	1.00	100	0	0	0	0
	0.71	80	0	0	20	0
	0.48	55	0	0	45	0
	0.20	18	0	29	54	0
	0.00	0	2	59	30	9

Heat Treatment, Quenched						
Heat Treatment Temperature (°C)	x	$LiFePO_4$	$FePO_4$	$Fe_7(PO_4)_6$	$Fe_2P_2O_7$	$FePO_4$ hex
600	1.00	100	0	0	0	0
	0.79	86	0	0	14	0
	0.48	56	0	0	44	0
	0.30	36	0	33	31	0
	0.00	0	0	47	53	0
800	1.00	100	0	0	0	0
	0.79	84	0	0	17	0
	0.48	56	0	0	44	0
	0.30	41	0	9	50	0
	0.00	0	0	37	63	0

In situ High Temperature XRD						
Measurement Temperature (°C)	x	$LiFePO_4$	$FePO_4$	$Fe_7(PO_4)_6$	$Fe_2P_2O_7$	$FePO_4$ hex
600	0.48	55	0	0	45	0
700	0.48	59	0	0	41	0
800	0.48	58	0	0	42	0
600	0.00	0	0	58	12	30
700	0.00	0	0	45	22	34
800	0.00	0	0	45	10	44

Table 5.4: Percentages of each phase for different heat treatment samples, including: heat treated and furnace cooled, heat treated and quenched, and *in situ* high temperature XRD measurements.

be that heterosite is more stable in an oxygenated environment. However, in the case of lithium batteries, oxygen levels are minimized, so our studies in an argon environment are applicable to battery systems. The product phases ($Fe_7(PO_4)_6$, $Fe_2P_2O_7$, plus free oxygen or other compounds having phosphorous and oxygen) are more stable than heterosite. The formation of the hexagonal $FePO_4$ suggests that the heterosite structure is also less stable thermodynamically than hexagonal $FePO_4$ in a closed system. Since the hexagonal $FePO_4$ sample is only seen in small amounts in furnace-cooled or quenched samples, it must be unstable at room temperature. At 600-800 °C, *in situ* XRD measurements showed a large amount of the sample was of the hexagonal $FePO_4$ phase, however, so it is a stable phase for delithiated $FePO_4$ materials we measured.

It appears that the new phases formed upon heat treatment are more stable thermodynamically than the heterosite phase at operating conditions of a rechargeable electrochemical cell. Transformation to these more stable phases would alter the electrochemical performance of a cell. Many different iron phosphate phases have been shown capable of lithium insertion, including $FePO_4 \cdot nH_2O$ [62, 68], $Li_3Fe_2(PO_4)_3$ [69, 70], $Li_3Fe_4(P_2O_7)_3$ [71], $Fe_4(P_2O_7)_3 \cdot 4H_2O$ [62], and $LiFeP_2O_7$ [71]. Although these other iron phosphate materials are capable of electrochemical cycling, they have only modest specific capacities (between 60 and 145 mAh/g), less than that of the orthorhombic system of $LiFePO_4$. Unfortunately, the present results on electrochemical capacity show that the products of heterosite decomposition, $Fe_7(PO_4)_6$, $Fe_2P_2O_7$ and the rodolicoite hexagonal $FePO_4$, are not good candidates for lithium insertion, although further studies are warranted on single phase materials. Transformation of heterosite into these stable phases is a possible reason for capacity fade in $LiFePO_4$ cells.

During electrochemical cycling, the heterosite phase is highly metastable, but the atom movements needed to transform heterosite to the equilibrium state are generally suppressed at room temperature. Nevertheless, different combinations of electrolyte, repetitive strains of lithiation and delithiation, and operation at elevated temperatures could promote the transformation of the orthorhombic form of heterosite to equilibrium phases. Describing the combination of kinetic factors that promote the transformation of heterosite would be speculation. Nevertheless, if a crystal structure is not in its equilibrium state, it is generally

possible for equilibrium to be achieved by an irreversible change of structure.

5.5 Conclusion

Crystal structure transformations in Li_xFePO_4 were studied after samples were heated to temperatures up to 800 °C. The triphylite form of $LiFePO_4$ was stable at all temperatures up to 800 °C. At room temperature, delithiation produces a fraction of orthorhombic heterosite, $FePO_4$, which has the same structural framework as triphylite. Heating two-phase mixtures of heterosite and triphylite to temperatures between 200 and 400 °C induces the formation of an intermediary phase between the two original phases. However, by heating above 400 °C, the delithiated $FePO_4$ heterosite phase transforms into other phases including $Fe_7(PO_4)_6$, $Fe_2P_2O_7$ and the rodolicoite hexagonal $FePO_4$. There was no evidence for reversibility of these transformations of heterosite, indicating that the product phases are stable thermodynamically, but their formation is suppressed kinetically at low temperatures. Preliminary evidence is that these product phases have poor capacity for lithium intercalation, and would act as inactive regions of an electrode in an electrochemical cell.

Chapter 6

Entropy of Lithiation in Li_xFePO_4

6.1 Introduction

Thermodynamic measurements, including entropy and enthalpy measurements, can give a detailed fingerprint of phase transitions and chemical reactions in a material. By measuring these properties at different states of lithiation, we can gain insight into the ordering of lithium in the material, as well as information of phase composition as lithium is added. In addition, the change in entropy versus lithiation can be an indicator of the intrinsic safety of the material, with larger entropy changes being associated with lower safety. A cathode material with a smaller enthalpy of lithiation also would be safer due to less heat generation as lithium is reinserted. This is especially important for high rate applications, as well as when a cell is short-circuited.

We have measured the entropy of lithiation ($\Delta S(x)$) and enthalpy of lithiation ($\Delta H(x)$) of Li_xFePO_4 and $Li_xMn_{0.2}Fe_{0.8}PO_4$ for $0 < x < 1$. These measurements were performed with half cells of the cathodes cycled vs. lithium metal. The temperature dependence of the open-circuit voltage (OCV) was used to determine $\Delta S(x)$ and $\Delta H(x)$. For Li_xFePO_4 these measurements point to the existence of single-phase regions at the ends of the compositional range ($x < 0.05$ and $x > 0.85$). For intermediate compositions, $0.1 < x < 0.85$, the measured $\Delta S(x)$ is not a constant value, as would be expected for a two-phase mixture. The $Li_xMn_{0.2}Fe_{0.8}PO_4$ system is more difficult to analyze, especially since there is a large hysteresis between charge and discharge of this cathode material.

Thus far in this thesis, only the $LiFePO_4$ cathode material has been studied. However,

the redox potential of 4.1 V vs. Li^+/Li for $LiMnPO_4$ makes it a good candidate for a cathode material. Due to its higher redox potential compared to $LiFePO_4$ (3.4 V vs. Li^+/Li) it has the possibility of being a higher power density material. Unfortunately, poor electrochemical performance has been reported for this material [13, 72, 73]. Li et al. were able to get a reversible capacity of 140 mAh/g by adding carbon black to the synthesis precursors and optimizing the sintering process [74]. Solid solutions of Mn and Fe, $Li[Mn_yFe_{1-y}]PO_4$ have shown more promising results [75, 76, 77]. For such a system, plateaus at 3.4 V vs. Li^+/Li and 4.1 V vs Li^+/Li can be attributed to the oxidation of Fe^{2+} and Mn^{2+}, respectively. The room temperature two-dimensional phase diagram of the olivine-type solid-solution, $Li_x[Mn_yFe_{1-y}]PO_4$ was evaluated by Yamada et al. [78], finding single-phase regions for a part of the Fe^{3+}/Fe^{2+} reaction, which is significantly different from the two-phase reaction for Li_xFePO_4. Reaction through a single phase with mixed valence (Fe^{3+}/Fe^{2+}) could result in improved rate capability of the electrode. Due to the interesting single-phase regions we wanted to measure the entropy and enthalpy of lithiation in a $Li_x[Mn_yFe_{1-y}]PO_4$ material, and electrodes with Mn content y = 0.2 were tested.

6.2 Experimental

Electrodes were received from Dr. Atsuo Yamada's group (Tokyo Institute of Technology). For their material synthesis, lithium, iron, manganese, and phosphate sources, were mixed by high energy ball milling along with a carbon powder, Ketjen Black (Lion Corporation), for 24 hours. Then the mixture was heated at 550 °C for 2 hours in argon gas flow. The active material was coated, along with conductive carbon and binder on an aluminum foil current collector. The composition of the cathodes was 82% LiFePO4, 9% conductive carbon, and 9% polyvinylidene difluoride (PVDF) binder. The coatings were made very thin (on average 0.012 mg/mm^2, so only 2-3 mg for a 16 mm diameter electrode) in order to get enable higher capacities, approaching the full theoretical capacity.

Coin cells of 20 mm diameter and 1.6 mm thickness (CR 2016-type) were used as half cells in this study. The cells consisted of the cathode cycled vs. a lithium metal counter electrode, with a microporous polyethlyene separator soaked with an electrolyte solution of

1M lithium bis(oxalato)borate (LiBOB) in propylene carbonate (PC) in between.

The cells were cycled from 2.0 to 4.5 V at a constant current C/20 rate, with a constant voltage charge at 4.5 V until a C/200 cutoff was achieved. The cell capacity was determined after cycling the cell five times to make sure the capacity was stable. The cells were then ready for thermodynamic measurements. The electrochemical thermodynamic measurement system (ETMS) was used for our study. The system was developed previously in our laboratory and is explained in more detail by Reynier et al. [79]. A brief explanation of the measurement methods is also given in section 3.4.4.

For each measurement, the cells were charged or discharged at C/20 rate to a different states of lithiation in increments of 0.05 (5% charge/discharge steps). After each change of lithiation, the cells were left at rest for open-circuit voltage equilibration for several hours. Then for each entropy/enthalpy measurement, the cells were cooled with a Peltier plate to five temperatures between room temperature and 12 °C, allowing a temperature equilibration of 20 minutes at each temperature. The voltage profile for the cells during the OCV vs. temperature measurements usually showed an overall downward slope, due to self-discharge of the cells. The downward slope was fit linearly and subtracted from the voltage profile, giving us a corrected OCV, which was plotted versus temperature, resulting in a linear curve.

6.3 Results

6.3.1 $LiFePO_4$ entropy and enthalpy measurements

The OCV of $LiFePO_4$ was measured during charge and discharge of the material. Figure 6.1 shows the OCV vs. x, for four-hour voltage equilibration times after a C/20 charge or discharge. It is evident that the OCV measured during charge is approximately 0.015 V higher than the OCV measured during discharge. The real equilibrium OCV should lie between the two. An equilibration time of four hours or greater was used for thermodynamic measurements, since it was found that measured values after 4 hours of equilibration were similar to those after 10 or 20 hours of equilibration.

After correction of the OCV for self-discharge, the OCV was plotted vs. temperature for

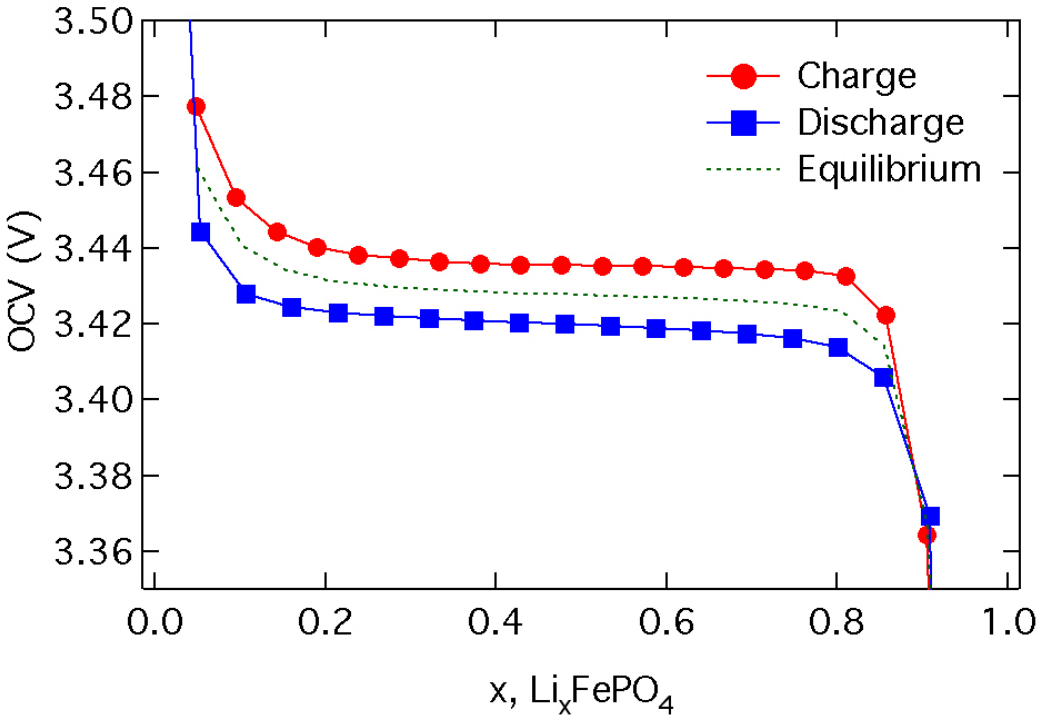

Figure 6.1: Open-circuit voltage vs. lithiation, x, plotted after charge or discharge at a C/20 rate, and then 4 hours of equilibration time. The OCV measured during charge and discharge differ by approximately 0.015 V.

all measurements. Figure 6.2 shows examples of OCV vs. temperature for Li_xFePO_4, for compositions $x = 0.10$ and $x = 0.80$. The OCV and temperature have a linear relationship.

By use of OCV vs. temperature plots, the entropy and enthalpy of lithiation were measured. The Gibbs free energy, $\Delta G(x)$ is related to the OCV, E_0, by the expression

$$\Delta G(x) = -FE_0(x) = \Delta H(x) - T\Delta S(x). \tag{6.1}$$

Therefore, the entropy of the addition of lithium in Li_xFePO_4, $\Delta S(x)$, can be expressed as

$$\Delta S(x) = F\left(\frac{\partial E_0}{\partial T}\right)_x, \tag{6.2}$$

while the enthalpy of the addition of lithium in Li_xFePO_4, $\Delta H(x)$, is

$$\Delta H(x) = F\left[T\left(\frac{\partial E_0}{\partial T}\right)_x - E_0(x)\right], \tag{6.3}$$

where F is the Faraday constant (96,485 C/mole), E_0 is the OCV, and T is the temperature. The entropy of lithiation is plotted for Li_xFePO_4 in Figure 6.3(b). The corresponding enthalpy of lithiation is also shown, in Figure 6.3(c). The values are expressed in terms of entropy and enthalpy per mole of lithium in the cathode. Measurements made in between charge steps were similar to those made between discharge steps. Therefore, the values from measurements taken during charge and discharge were averaged.

The entropy of lithiation has three characteristic regions. As lithium is first added to the material (near $x = 0$), the entropy increases slightly. For $0.05 < x < 0.85$, $\Delta S(x)$ gradually becomes more and more negative, down to -14 J/(mol K). At $x > 0.85$, there is a sharp change in $\Delta S(x)$, with an increase in its value at $x = 0.9$ and then a sharper decrease again as x approaches 1. Similarly, the enthalpy of lithiation indicates these three regions, with a relatively flat value of between -331 and -334 kJ/mol for $0.05 < x < 0.85$, and varying values of $\Delta H(x)$ for $x < 0.05$ and $x > 0.85$.

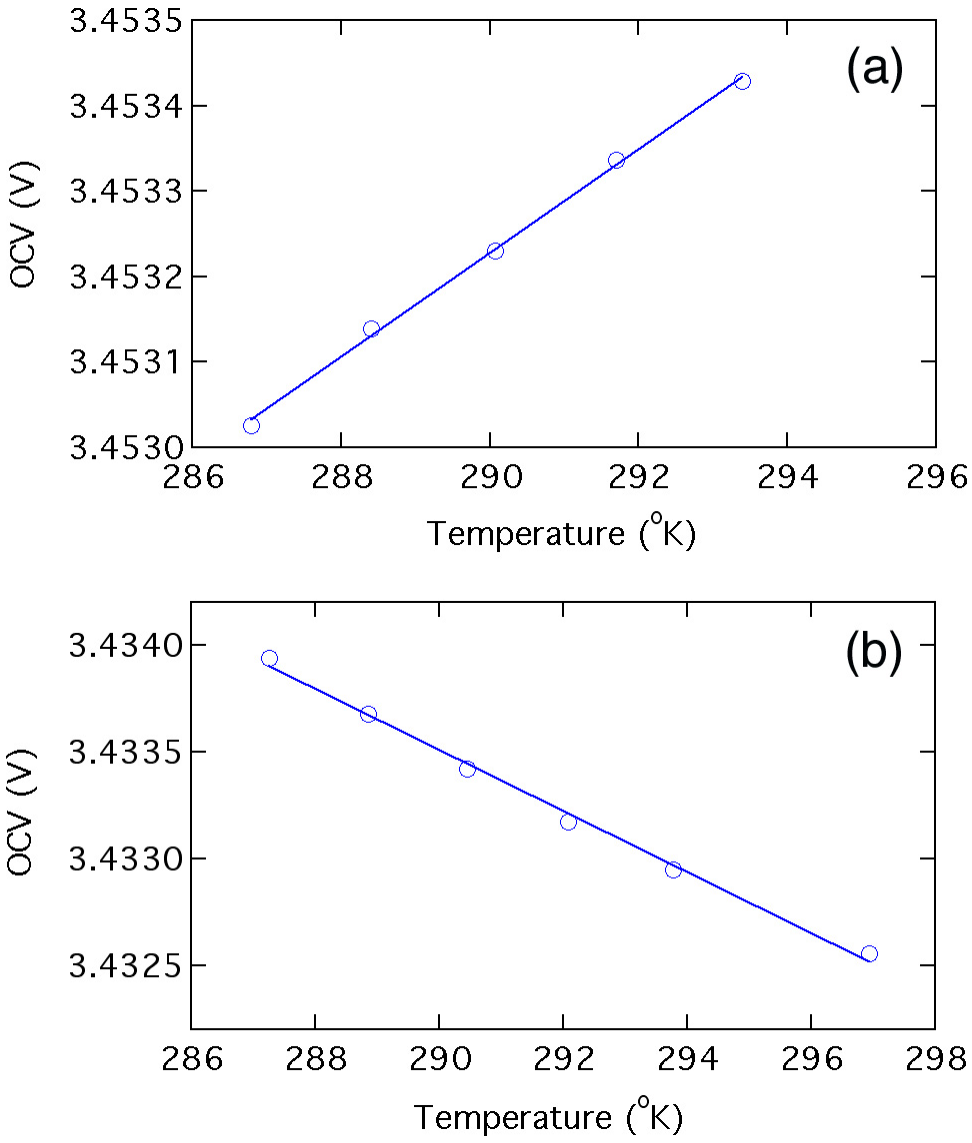

Figure 6.2: Open-circuit voltage vs. temperature for Li_xFePO_4 material with compositions $x = 0.10$ (a) and $x = 0.80$ (b). Linear fits are also shown for each case, with R^2 values of 0.998 and 0.995 for parts a and b, respectively.

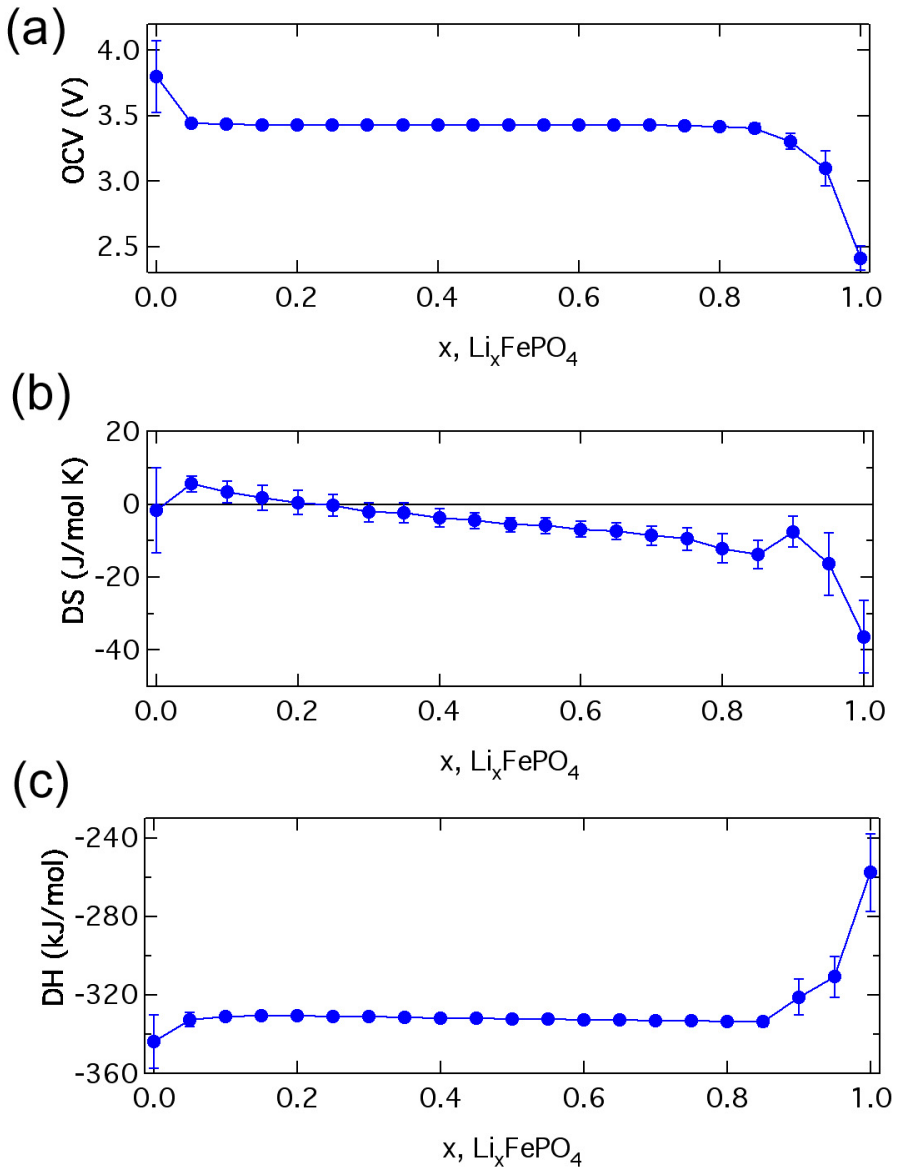

Figure 6.3: (a) The open-circuit voltage of Li_xFePO_4 vs. lithium content. (b) Average values of the entropy of lithiation, $\Delta S(x)$, and (c) the enthalpy of lithiation, $\Delta H(x)$, for Li_xFePO_4. Measurements were taken at intervals during charge or discharge of $LiFePO_4$ cells, with either 4-hour or 20-hour equilibration times at each state of lithiation. All such measurements were averaged, and standard deviations are indicated by error bars.

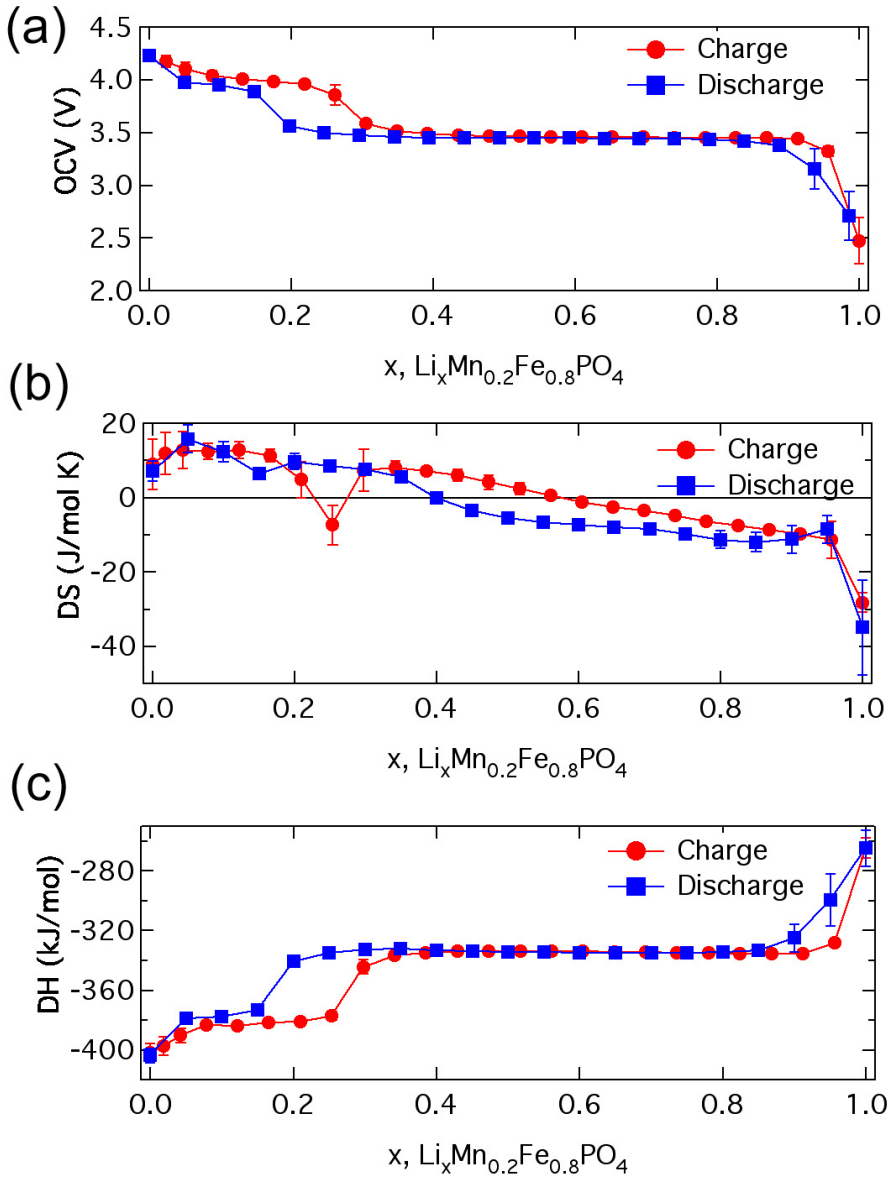

Figure 6.4: (a) The open-circuit voltage of $Li_xMn_{0.2}Fe_{0.8}PO_4$ vs. lithium content. (b) Average values of the entropy of lithiation, $\Delta S(x)$, and (c) average values of the enthalpy of lithiation, $\Delta H(x)$, for $Li_xMn_{0.2}Fe_{0.8}PO_4$. Measurements were taken after 4-hour voltage equilibration times, after charge or discharge at a C/20 rate. Measurements taken during charge were averaged separately from those taken during discharge. Standard deviations are indicated by error bars.

6.3.2 $Li_xMn_{0.2}Fe_{0.8}PO_4$ entropy and enthalpy measurements

Thermodynamic measurements were similarly performed on $Li_xMn_{0.2}Fe_{0.8}PO_4$ cathodes. Right away, from looking at the OCV vs. x, a large hysteresis is noticeable between charge and discharge of the material, especially near $x = 0.2$ (see Figure 6.4(a). Lithium is electrochemically extracted first at a potential of approximately 3.45 V due to the Fe^{3+}/Fe^{2+} redox reaction (for $0.2 < x < 1$), and then at approximately 4.0 V due to the Mn^{3+}/Mn^{2+} redox reaction (for $0 < x < 0.2$). The boundary of $x = 0.2$ is only approximate, however, and varies depending upon whether the cell is charged or discharged.

The entropy of lithiation of $Li_xMn_{0.2}Fe_{0.8}PO_4$ is also different when measured during charge and discharge (see Figure 6.4(b). In both cases, however, there is a sharp change in $\Delta S(x)$ at $x < 0.10$ and $x > 0.95$, which is similar to the Li_xFePO_4 measurements, which also showed a sharp change in entropy near $x = 0$ and 1. In addition, there are jumps in the entropy values, between $x = 0.25$ and 0.30 during charge, and between $x = 0.15$ and 0.20 during discharge. These jumps in values correspond to where the enthalpy, $\Delta H(x)$, also shows a distinct change (see Figure 6.4(c).

6.4 Discussion

6.4.1 $LiFePO_4$

The entropy and enthalpy of lithiation point to three regions of Li_xFePO_4, namely $x < 0.05$, $0.05 < x < 0.85$, and $x > 0.85$. The sharp changes in entropy and enthalpy at the ends of the composition ($x < 0.05$ and $x > 0.85$) are indicative of a transition from the two-phase system to single-phase regions. This result is in agreement with the work by Yamada et al. [51], where the site occupancies for lithium in each phase of the two-phase electrode reaction were measured by neutron diffraction, and refined to be 0.05 and 0.89. Due to a deviation of the OCV from a constant equilibrium potential of 3.42 V and also an anomaly in heat flow at end regions of lithiation, they also indicated that there are solid solution regions from $x < 0.05$ and $x > 0.89$ at room temperature. Our measurements indicate solid solution regions for $x < 0.05$ and $x > 0.85$. Since the miscibility gap appears to be dependent upon particle size (see section 2.5.2) it is important to note that the particles

used in these thermodynamic studies had an average diameter of 70 nm, as shown by the scanning electron microscopy image in Figure 6.5(a). The extent of solid solution regions near $x = 0$ and 1 are similar to what has been reported by others [51, 52].

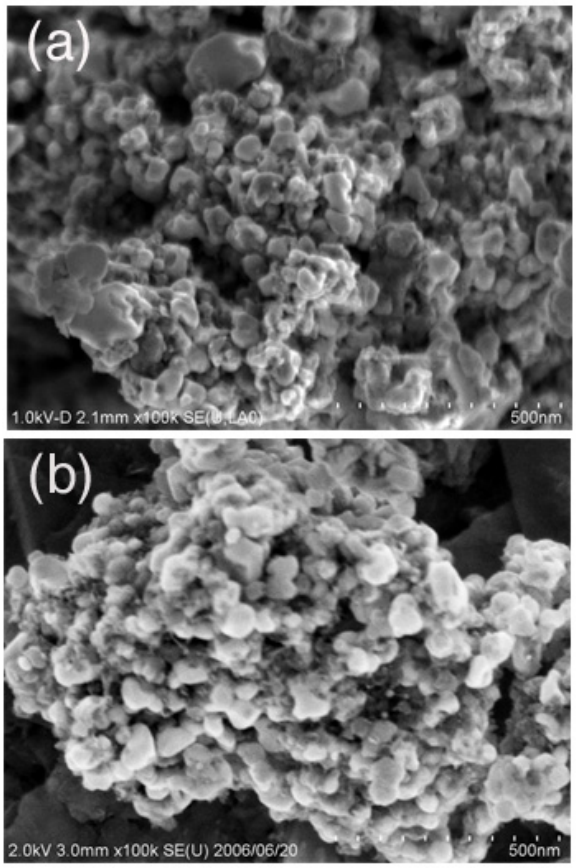

Figure 6.5: Scanning electron microscopy images of (a) LiFePO4 and (b) $LiMn_{0.2}Fe_{0.8}PO_4$ powders, at 100,000× magnification. Both powders had particles with an average diameter of 70 nm.

For the intermediate region, $0.05 < x < 0.85$, a two-phase system is expected. For a two-phase system, a constant entropy of lithiation would be expected as lithium is added or extracted from one phase to the other. However, we have repeatedly seen a slope in the entropy of lithiation, as shown in Figure 6.3(b). We have made many different measurements of the entropy, during charge and discharge of the half cells, and also with different equilibration times (between 4 hours and 20 hours) and found similar results. Possible explanations for the change in $\Delta S(x)$ with lithium composition will be discussed in section

6.4.4.

The enthalpy for compositions in this intermediate region, $0.05 < x < 0.85$, (Fig. 6.3(c)) is quite flat, as expected for a two-phase region with a first-order transition. However, there is a slight slope in this region, with values varying between -331 and -334 kJ/mol. It is unclear whether or not this variation is significant. Certainly though, for $x < 0.05$ and $x > 0.85$ there are large changes in $\Delta H(x)$ values, indicating single-phase regions.

6.4.2 $\mathbf{Li}_x\mathbf{Mn}_{0.2}\mathbf{Fe}_{0.8}\mathbf{PO}_4$

The $Li_xMn_{0.2}Fe_{0.8}PO_4$ cathode has distinctly different thermodynamic characteristics when measured during charge and discharge. The transition between the Fe and Mn redox reactions should occur at around $x = 0.20$, due to the manganese content of the material. However, during charge, the OCV rises above 3.45 V starting at around $x = 0.35$. This gradual change in potential is somewhat consistent with the single-phase region reported by Yamada et al. for $0.2 < x < 0.55$ [78]. However, the OCV measurements do not indicate that the single-phase region extends as high as $x = 0.55$. During discharge of the material, the change between 4.0 and 3.45 V occurs at a lower state of lithiation, between approximately $x = 0.15$ and 0.30, approaching 3.45 V at a lower lithium content than seen during charge.

Similarly to the Li_xFePO_4 material, sharp changes in $\Delta S(x)$ indicate single-phase regions for $x < 0.10$ and $x > 0.95$. For intermediate x ($0.10 < x < 0.95$), the entropy values are more complicated. They are different when measured during charge and discharge, suggesting that there may be differences in the manner by which lithium is inserted into and extracted from the material. During charge, there is a sharp change in the entropy profile between $x = 0.25$ and 0.30, corresponding to the transition between lithium extraction from nearby Fe atoms to extraction from nearby Mn atoms. Between $x = 0.15$ and 0.25, $\Delta S(x)$ varies with a steeper slope, indicating a single-phase region. When measured during the discharge process, there is a change in the entropy profile at $x = 0.15$, although not as distinctive as measured during the charge process. Also during discharge, the two regions, $0.20 < x < 0.35$ and $0.55 < x < 0.95$ have flatter profiles of $\Delta S(x)$, while between 0.35 and 0.55 there is a steeper profile, possibly due to a single-phase region. In general, it is difficult to analyze the

$Li_xMn_{0.2}Fe_{0.8}PO_4$ material, since there are so many regions with different characteristics. The following section will focus on the intermediate region of Li_xFePO_4 ($0.05 < x < 0.85$) but similar concepts may also apply to manganese substituted compounds, for expected two-phase regions.

6.4.3 Configurational Entropy Contributions

Within a single phase, the configurational entropy of mixing can be calculated in the point approximation for a fully disordered lattice of lithium atoms and vacant sites, as

$$S_{cf}(x) = -k_B(x_2 - x_1)\left[\chi ln\chi + (1-\chi)ln(1-\chi)\right],\ with\ \chi \equiv \frac{x - x_1}{x_2 - x_1}, \tag{6.4}$$

where x_1 and x_2 are the lithium concentrations of the structures that are modified by lithium atom-vacancy disorder when $x_1 < x < x_2$ [79]. For the $\Delta S(x)$ of lithiation which we measured, a configurational entropy contribution would be the derivative of $\Delta S_{cf}(x)$ with respect to x, which is shown here, in equation (6.5):

$$\frac{\Delta S(x)_{cf}}{\Delta x} = k_B ln\left(\frac{x_2 - x}{x - x_1}\right). \tag{6.5}$$

Li_xFePO_4 has been shown to be a two-phase system, but our entropy measurements resemble values for single phase systems. Figure 6.6 is a plot of the measured $\Delta S(x)$ along with two versions of calculated $\Delta S_{cf}(x)$ values using equation 6.5. For version A, $\Delta S_{cf}(x)$ is split into three single-phase regions: $x < 0.05$, $0.05 < x < 0.85$, and $x > 0.85$. For version B, $\Delta S_{cf}(x)$ is calculated for $0 < x < 1$. Since no differences in lithium sites are known for Li_xFePO_4 with $0 < x < 1$, version B of $\Delta S_{cf}(x)$ would be expected for the single-phase end regions of $x < 0.05$ and $x > 0.85$. However, version A seems to fit the $x > 0.85$ data better. We expect a single phase for $x > 0.85$, since it has been indicated by Yamada's work [51]. Since version A fits the data well, it is possible that there is some ordered pattern of filled lithium sites near $x = 0.85$, and when x exceeds this amount there is a slightly increased $\Delta S(x)$, as seen in version A of $\Delta S_{cf}(x)$. A single-phase solid solution is also expected for $x < 0.05$ [51]. We would need to measure several values of entropy for $x < 0.05$ to confirm

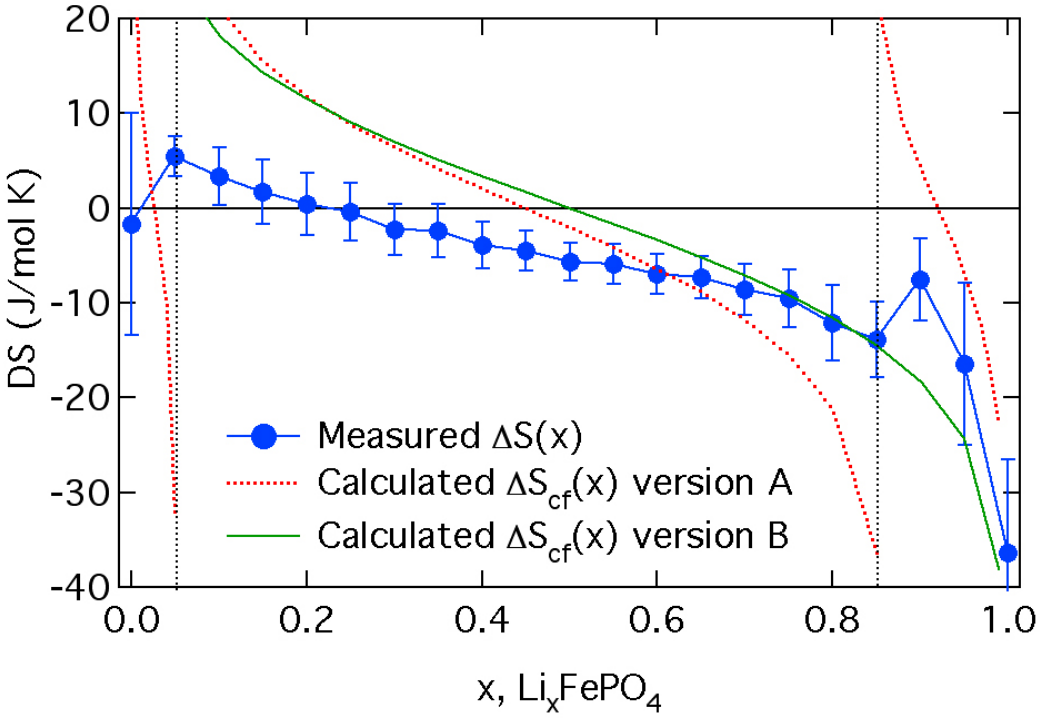

Figure 6.6: Comparison of measured $\Delta S(x)$ to calculated $\Delta S(x)_{cf}$ for $x < 0.05$, $0.05 < x < 0.85$, and $x > 0.85$ (version A) and for $0 < x < 1$ (version B).

whether it is a single-phase region, but this is difficult to do, especially since the $x < 0.05$ region is at the end of charge, requiring nearly all of the lithium to be extracted from the cathode. The actual value of x is less accurate in this region, which could also possibly explain the large error bars for our measurements taken at full charge ($x = 0$). It is possible that we have measured $\Delta S(x)$ for a variety of x near 0, and that the spread of our measured $\Delta S(x)$ values could be due to the sharp change of the $\Delta S_{cf}(x)$ curve shown (for $x < 0.05$). Similarly, the error bars for $x > 0.85$ are much larger than for $0.05 < x < 0.85$. This can be attributed to some variation in measured x, causing larger error bars since the entropy varies sharply in this area.

The slope in entropy measured for $0.05 < x < 0.85$ bears a resemblance to what the configurational entropy ($\Delta S_{cf}(x)$) would look like if the system were a single phase in this region (see Figure 6.6). However, the slope of the measured entropy is not as steep in comparison to the $\Delta S_{cf}(x)$. It may be possible that there is some contribution of configurational entropy, but this would not be expected for a strictly two-phase system.

6.4.4 Varying $\Delta S(x)$ in the Intermediate Region, $0.05 < x < 0.85$

6.4.4.1 Interface Contributions

Contributions to the entropy from the interface between the heterosite and triphylite phases could possibly account for some of the variation in $\Delta S(x)$ with x. Laffont et al. have looked closely at interfacial regions, finding that for an approximately 200 x 100 x 50 nm $LiFePO_4$ particle, the interfaces were between 10 and 20 nm in size [34]. Therefore, the particles Laffont investigated had significant interfacial volumes, at 10%-20% of the total volume. From high-resolution electron energy loss spectroscopy (EELS) measurements, they inferred that the interfacial zone was composed of both end-member phases ($LiFePO_4$ and $FePO_4$), with the combinations of phases gradually changing. However, it is unclear how large the phase domains are in the interface, and the lithium may actually be disordered at the atomic scale, giving a higher configurational entropy at the interface. Therefore, a larger percentage of interface in the material could shift the entropy of lithiation in the positive direction. According to this hypothesis and our entropy measurements, we would expect a

larger interfacial volume for lower lithium contents in the range of $0.05 < x < 0.85$.

In Laffont's work, there was some variation in the size of the interface compared to the state of lithiation. However, it is uncertain whether this is a true effect or if it is coincidental. The size of the interface was larger for the $x = 0.26$ compared to $x = 0.45$ and 0.75 samples. However, the interface volumes for $x = 0.45$ and 0.75 were similar. According to their model, the heterosite phase forms at the core of the particle, with triphylite surrounding it. For a lower x, there is a smaller portion of triphylite surrounding the heterosite phase. It is under compressive strain, since heterosite has a smaller unit cell. A thinner triphylite shell would result in a larger strain, and possibly a larger interface to transition between the two phases. A better understanding of the material strains, the interface volumes, as well as the delithiation mechanism of $LiFePO_4$ is necessary in order to support this idea.

If the size of the interface is a cause for the variation in $\Delta S(x)$ with x, different morphologies or particle sizes of $LiFePO_4$ could have an effect on the entropy of lithiation. For example, for larger crystal sizes, the interface volume percentage of total volume will be largely reduced. The high-resolution transmission electron microscopy (TEM) work by Chen et al. showed an approximately 10 nm dimension for the interface, for large platelike particles ($\sim$2-5 μm diameter for *ac* plane, $\sim$200 nm thick in *b* direction) [80]. They also suggest that there may be numerous nucleation sites, where the phase transformation from one phase to the other begins. These nucleation sites would be located where the *ac* faces are well connected to the conducting matrix of the electrode. Therefore, it is difficult to try to estimate the interfacial volume for such large crystals, but it should be much lower compared to nanosized crystals. It is important to note that more dislocations were found for these larger particles as well, indicating that the interface is not coherent for larger crystal sizes. An incoherent interface is expect to have smaller dimension, due to stress relief from formed dislocations. However, a coherent interface serves as a buffer region, supporting the lattice mismatch between heterosite and triphylite. Thus for smaller particles where charge and discharge occurs with a coherent interface, the interface is expected to be wider.

6.4.4.2 Nonequilibrium effects

Another possible cause for a sloping $\Delta S(x)$ with lithiation could be nonequilibrium effects in the electrode. As was seen from the OCV, there is a difference between our measured OCV during charge and discharge. The system is not in equilibrium, but in a quasi equilibrium. Therefore, we can make good estimates on the thermodynamic properties of the material, but there could be some variations in these properties due to kinetic effects. First of all, there are different transport rates in the heterosite and triphylite phases. Therefore, the rate at which the interface moves during the electrochemical lithium insertion may be different on each front (on the heterosite and triphylite sides). This would result in a change in the interface size vs. x. As the interface size changes, the gradient of the two phases in the interfacial region varies. This could also be a reason for the varying $\Delta S(x)$ vs. lithiation.

In addition, it has been reported that the equilibrium composition of the triphylite phase is $Li_{0.89}FePO_4$ and for the heterosite phase it is $Li_{0.05}FePO_4$. However, under nonequilibrium conditions, the phase compositions may not necessarily be constant. The triphylite phase composition can vary from $x = 1$ to $x = 0.89$, and the heterosite phase composition can vary from $x = 0$ to $x = 0.05$. If this is the case, it certainly would have an effect on the entropy of lithiation.

6.4.4.3 Possible thermal strain effects

Another explanation for the varying $\Delta S(x)$ for $0.05 < x < 0.85$ is that strain energy effects, including strain associated with thermal expansion differences between heterosite and triphylite, may be affecting the temperature dependence of the OCV. Since the triphylite and heterosite structures are different, unequal thermal expansion can cause thermal strains. Anisotropic thermal expansion may be important, too. An increase in strain energy causes a decrease in the OCV (E_0) of the material, with the relationship $\Delta E_{strain} = -F\Delta E_0$. The strain energy can be expressed as

$$E_{strain} = \frac{1}{2} B v (\epsilon_o)^2, \tag{6.6}$$

where B is the bulk modulus of the material, ϵ_o is the material strain, and v is the specific volume. Considering a thermal strain effect, an additional strain, $\epsilon_{thermal}$, must be added, giving the following:

$$E_{strain+thermal} = \frac{1}{2} Bv \left(\epsilon_o + \epsilon_{thermal}\right)^2, \tag{6.7}$$

$$\Delta E_{thermal} = Bv\epsilon_o\epsilon_{thermal} + \frac{v}{2} B\epsilon_{thermal}^2. \tag{6.8}$$

The thermal strain contribution should be much smaller than the original material strain ($\epsilon_{thermal} << \epsilon_o$), so for small $\epsilon_{thermal}$, the second term in equation (6.8) is negligible. From Figure 6.3(b), the values of $\Delta S(x)$ at $x = 0.10$ and $x = 0.80$ are 5.9 J/(mol K) and -13.8 J/(mol K), respectively (note: the OCV vs. T curves for these two compositions are found in Figure 6.2). For a two-phase system when $0.05 < x < 0.85$ we would expect a constant value of $\Delta S(x)$ in this region. However, we have a measurable difference. If these differences are due to thermal strain effects, it would be necessary that at $x = 0.80$ there be a much larger strain than at $x = 0.10$, such that the negative slope of the OCV vs. T curve is due to thermal strain contributions.

First-principle calculations have been performed for $LiFePO_4$ and $FePO_4$ in order to determine their elastic properties. Maxisch and Ceder found that the lithiated triphylite phase has a significantly larger bulk modulus than delithiated heterosite. Their calculations gave bulk moduli of $B_T \sim 95$ GPa for triphylite and $B_H \sim 70$ GPa for heterosite [81]. We have measured the bulk moduli of $LiFePO_4$ and $FePO_4$ by high-pressure XRD work with a diamond-anvil cell (see A), finding a similar trend, with $B_T = 106 \pm 8$ and $B_H = 61 \pm 3$. In this further discussion on thermal strain effects, our experimental values of B were used.

Using the $x = 0.10$ and 0.80 compositions of Li_xFePO_4 as an example, we wanted to see if thermal strain effects could account for the difference between $\Delta S(0.10)$ and $\Delta S(0.80)$. Due to the higher stiffness of triphylite compared to heterosite, we expect a lower strain in the triphylite phase. In addition, since it is under compressive strain, ϵ_o would be negative. In our entropy measurements, the cell temperature was reduced from room temperature to around 13 °C, so any thermal strain in our samples would be for at most $\Delta T = 10$ °C at the lowest temperature. If thermal strains are an artifact which is causing the change of $\Delta S(x)$

between 0.10 and 0.80, subtracting thermal strain effects from the OCV values should give us the real $\Delta S(x)$, which would be constant for the two-phase region of $0.05 < x < 0.85$. Table 6.1 shows two examples of hypothetical strain values for which thermal strains could account for the changing entropy of lithiation values, along with what the value of $\Delta S(x)$ would be if thermal strain effects were subtracted for each case. Figure 6.7 shows the original OCV vs. T curves, along with the curves after subtracting off thermal strain effects according to these two examples.

	$\epsilon_{thermal}$ per °K	ϵ_o, Triphylite	ϵ_o, Heterosite	$\Delta S(x)$ J/(mol K)
Example 1	0.0008	-0.003	0.025	-17
Example 2	0.0004	-0.003	0.011	-19

Table 6.1: Example strain values, in considering thermal strain effects on the entropy of lithiation.

Overall, thermal strain effects could have an effect on the OCV as temperature is decreased. However, accounting for the full change in the entropy of lithiation between $x = 0.10$ and 0.80 would require extremely large thermal strains. It also would require a much higher strain in the heterosite phase compared to the triphylite phase. Thermal strain values for $LiFePO_4$ have not been calculated, but many ceramic materials have thermal expansion coefficients of $\sim 10^{-5}$ K^{-1}, only one order of magnitude lower than the hypothetical $\epsilon_{thermal}$'s necessary for large enough thermal strain effects in the case of Li_xFePO_4.

6.5 Conclusion

Thermodynamic measurements of Li_xFePO_4 and $Li_xMn_{0.2}Fe_{0.8}PO_4$ give interesting information about the phase composition of the materials. The entropy and enthalpy of lithiation of Li_xFePO_4 both indicate that there are single-phase regions for $x < 0.05$ and $x > 0.85$. Similar measurements for $Li_xMn_{0.2}Fe_{0.8}PO_4$ indicate single-phase regions for $x < 0.10$ and $x > 0.95$. For both materials, entropy values for the intermediate regions are less predictable. We investigated this region for Li_xFePO_4 in more detail. Since Li_xFePO_4 is a two-phase system in between $x = 0.05$ and 0.85, we would expect $\Delta S(x)$ to be a constant

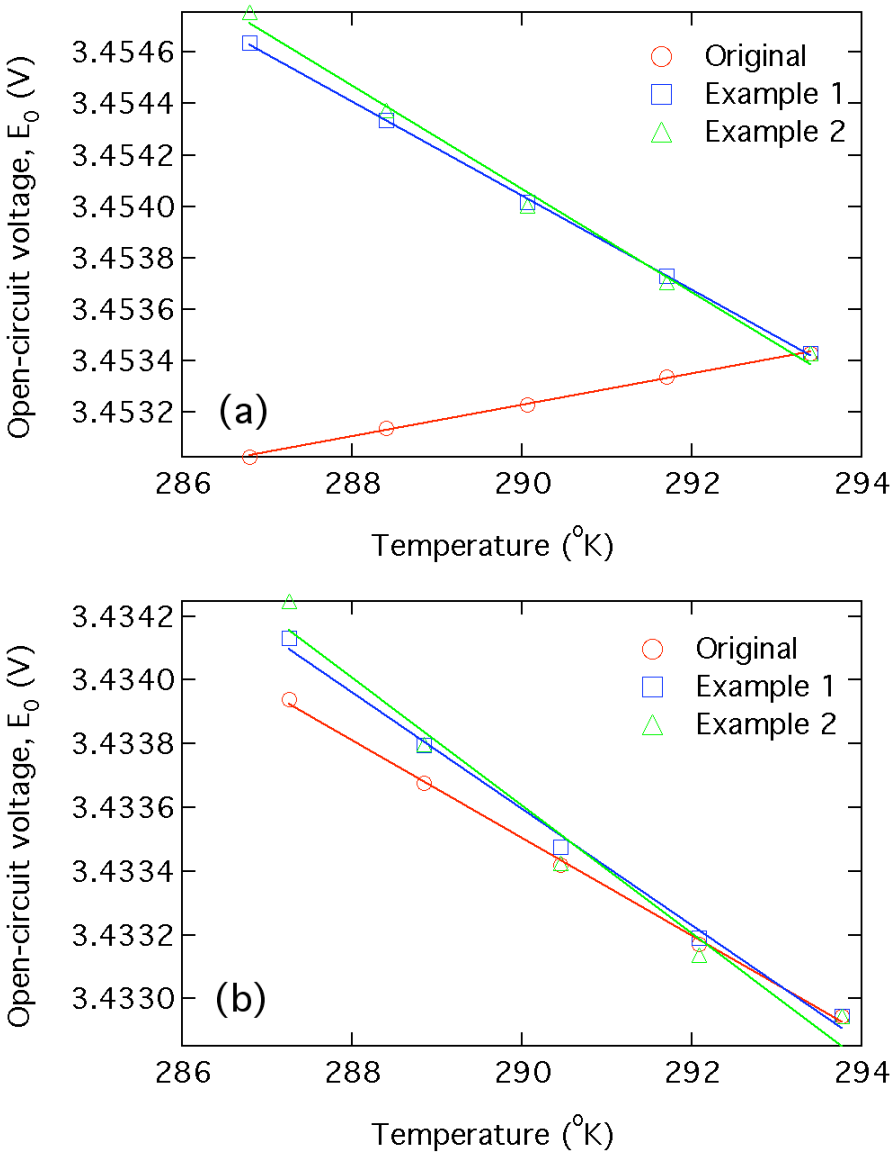

Figure 6.7: OCV vs. T curves for (a) $x = 0.10$ and (b) $x = 0.80$. The original OCV vs. T is plotted, along with curves which were adjusted by subtracting off hypothetical thermal strain effects.

value in that region, but we see a decrease of $\Delta S(x)$ as more lithium is added. The thermal strain effect vs. change in composition is a candidate for further study. It may be a cause for this sloping $\Delta S(x)$. It may also be possible that the interface between triphylite and heterosite contributes to this decrease of $\Delta S(x)$ with lithiation. Further investigations on the effect of x on interfacial volume and phase strains should be pursued. Also, further studies thermodynamic measurements of $LiFePO_4$ materials with different morphologies could be helpful in understanding the mechanisms of how lithium is inserted into the material.

Chapter 7

Valence Fluctuations of ^{57}Fe in Li_xFePO_4

7.1 Introduction

Although $LiFePO_4$ has many advantages as a cathode material, including it being nontoxic, highly stable, and inexpensive [13], a major disadvantage remaining is its low intrinsic electrical conductivity [30, 36]. As was discussed in an earlier section (2.4), much work has been done to improve the electrical performance of $LiFePO_4$ by particle-size minimization [23], carbon coating [38, 39], or by doping the material with supervalent cations [30]. In contrast to seemingly low intrinsic electrical conductivity, first-principles calculations indicate a high intrinsic ionic and electric mobility with relatively low activation energies for free Li and free polaron transport (175-270 meV)[32, 82]. In addition, several groups have measured the activation energy for electrical conductivity in pristine $LiFePO_4$, resulting in a wide range of values between 150-630 meV [21, 30, 36, 83, 84].

When lithium is inserted or extracted at room temperature, Li_xFePO_4 changes its fraction x of lithiated triphylite phase ($LiFePO_4$), and its fraction $1-x$ of delithiated heterosite phase ($FePO_4$). Both phases are olivine-type orthorhombic structures, but the lithiated triphylite structure contains chains of lithium ions. Recently a single-phase Li_xFePO_4 solid solution, with random lithium occupation of lithium sites, was discovered at temperatures of around 200 °C [48, 49], and its phase stability assessed [60, 59]. The electrical and ionic conductivity of this new phase has generated widespread interest.

Portions of this chapter have been published in the journal article: J. L. Dodd, I. Halevy, and B. Fultz, *J. Phys. Chem. C Lett.*, **111**, 1563 (2007).

During our previous study of phase diagrams, described in chapter 4, we found that the high temperature disordered solid solution phase of Li_xFePO_4 could be preserved at low temperatures, owing to the sluggish kinetics of the unmixing processes at temperatures below 200 °C. This is especially true for the composition of $Li_{0.6}FePO_4$, for which the disordered solid solution is stable at relatively low temperatures, much as for a eutectoid transformation. A previous study looked at Mössbauer measurements of Li_xFePO_4 disordered solid solution at temperatures greater than 200 °C [85], but here we were able to compare the disordered and two-phase materials at the same temperature between room temperature and 200 °C. In this chapter we report that the Mössbauer spectrum from the quenched, disordered phase is very similar to the spectrum from the two-phase material at room temperature. Our comparison of the local electronic structures of disordered and two-phase samples at elevated temperatures revealed fluctuations in local electronic structure within the time window of ^{57}Fe Mössbauer spectrometry, which is from 1 to 100 ns. We report large electronic fluctuations in the disordered sample at temperatures above 130 °C to 240 °C, and only weak effects in the two-phase sample at these temperatures.

Small polaron hopping is expected to contribute to the electrical conductivity in Li_xFePO_4, much as for other iron oxides. The atoms neighboring an iron ion have different distances and angles from Fe^{2+} and Fe^{3+}. These distortions accompany the motion of charge between iron ions, and promote the localization of charge. Likewise, neighboring Li^+ ions also cause local distortions of atom positions, electronic structure, and charge mobility. It is likely that the diffusional motions of Li^+ ions are coupled to charge transport, and hence electrical conductivity. Maxisch et al. [82] have found by first-principles calculations that there is strong binding between Li^+ and polarons (370 meV), as well as strong hole-vacancy binding (>500 meV). Altering the state of order should affect the diffusivity of Li^+ ions.

7.2 Experimental

Powders of $LiFePO_4$ were prepared by a solid-state reaction, and delithiated chemically by use of potassium persulfate, as described in section 3.3.2. The material had average particle sizes of 100-200 nm. Samples of composition $Li_{0.6}FePO_4$ were used in this study.

The composition was determined by x-ray diffraction measurements with Cu Kα radiation (PANalytical X'Pert PRO X'Celerator) and Rietveld refinement with X'pert Plus software (PANalytical). At low temperatures the system is a two-phase mixture, with nearly all the lithium in the triphylite phase. The fraction of triphylite ($LiFePO_4$) in the sample before heat treatment was determined by Rietveld analysis, and was used as a measure of the concentration of lithium in the sample. After heat treatment, samples were again analyzed with Rietveld analysis. A portion of this material was prepared as a disordered solid solution by heating to 380 °C in an evacuated glass ampoule, and quenching the sealed ampoule in water.

Mössbauer spectrometry was performed using a conventional constant acceleration spectrometer with sources of ^{57}Co in Rh, and velocity calibration to α-Fe at room temperature. All samples had natural ^{57}Fe abundance. An electrical resistance furnace was constructed to enable measurements of transmission spectra at elevated temperatures. The sample was taped in contact with aluminum foil with Kapton tape (figure 7.1(a)). The aluminum foil was wrapped around an aluminum plate and the sample was aligned with a lead plate to only allow gamma rays to pass through the sample. Two power resistors (25 W, 150 ohm) were placed in contact with the aluminum plate with heat sink silicone grease to ensure good thermal conduction (figure 7.1(b)). While heating, the power resistors were connected in parallel with alligator clips to a constant voltage/constant current power supply (0-45 V, 0-0.5 A). Finally, glass-wool insulation was wrapped around the aluminum plate and resistors to enable measurements at elevated temperatures. The setup of the instrument is shown in figure 7.1(c), with the radioactive source to the left and the detector to the right of the sample.

Temperature homogeneity was checked with multiple thermocouples, and was found to be approximately ±5 °C. The measurement times varied between 8 to 20 hours, with measurements at elevated temperatures requiring longer times, due to the absorption of some of the gamma rays by the furnace insulation material before reaching the detector. Spectra were acquired again after cooling, to ensure that the heating did not cause changes to the spectra at 25 °C. After measurements with Mössbauer spectrometry at elevated temperatures, the samples were analyzed again with XRD and Rietveld analysis to determine phase

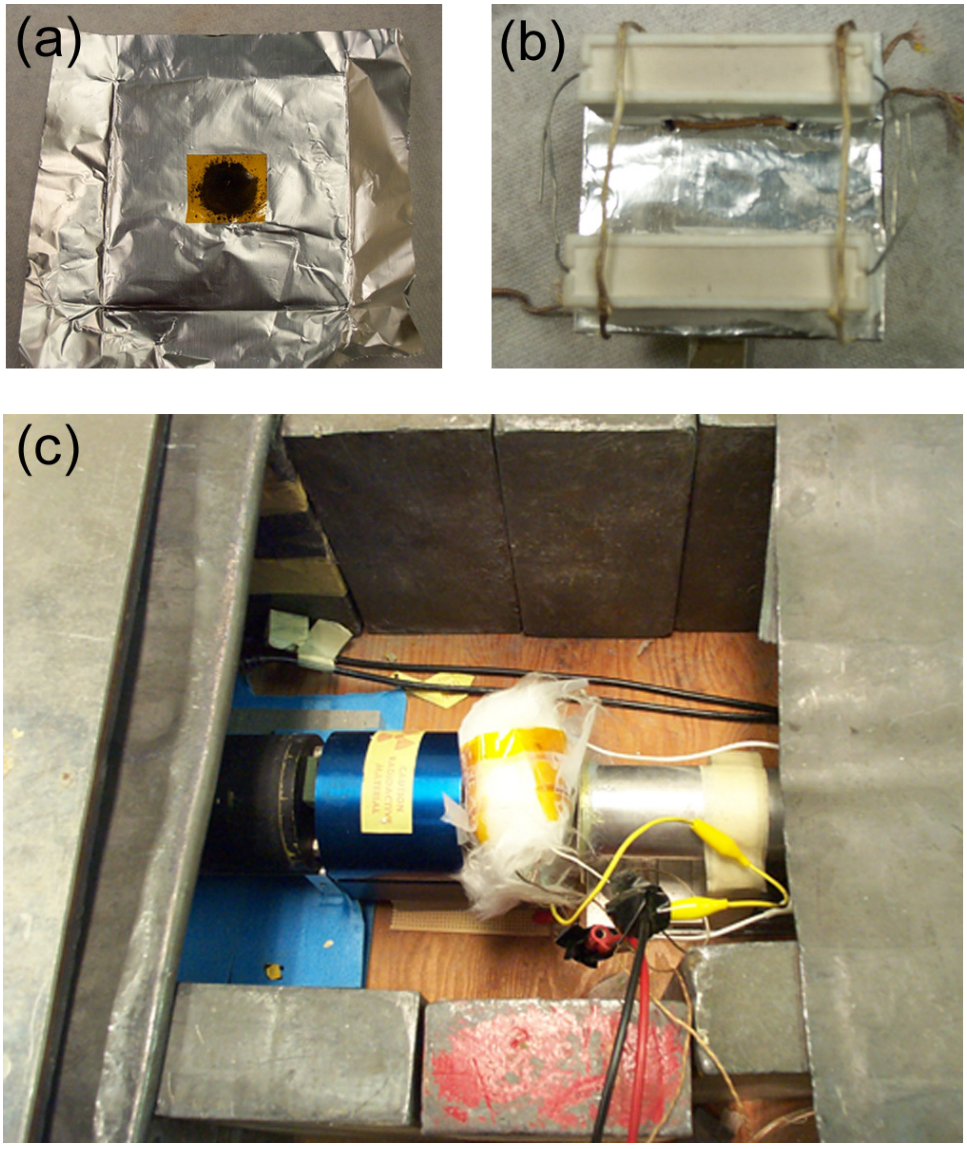

Figure 7.1: Pictures of furnace setup. (a) $Li_{0.6}FePO_4$ sample taped to aluminum foil. (b) Power resistors placed in contact with the aluminum foil and an aluminum plate. (c) The sample wrapped in glass-wool insulation and placed in line with the ^{57}Co radioactive source (to the left) and the detector (to the right).

fractions.

7.3 Results

XRD patterns of the two-phase and disordered solid solution $Li_{0.6}FePO_4$ samples are shown in figure 7.2. The XRD patterns of triphylite ($x = 1.0$)and heterosite ($x = 0$) are also shown for comparison. Both $x = 0.6$ samples were measured further with Mössbauer spectrometry at various temperatures.

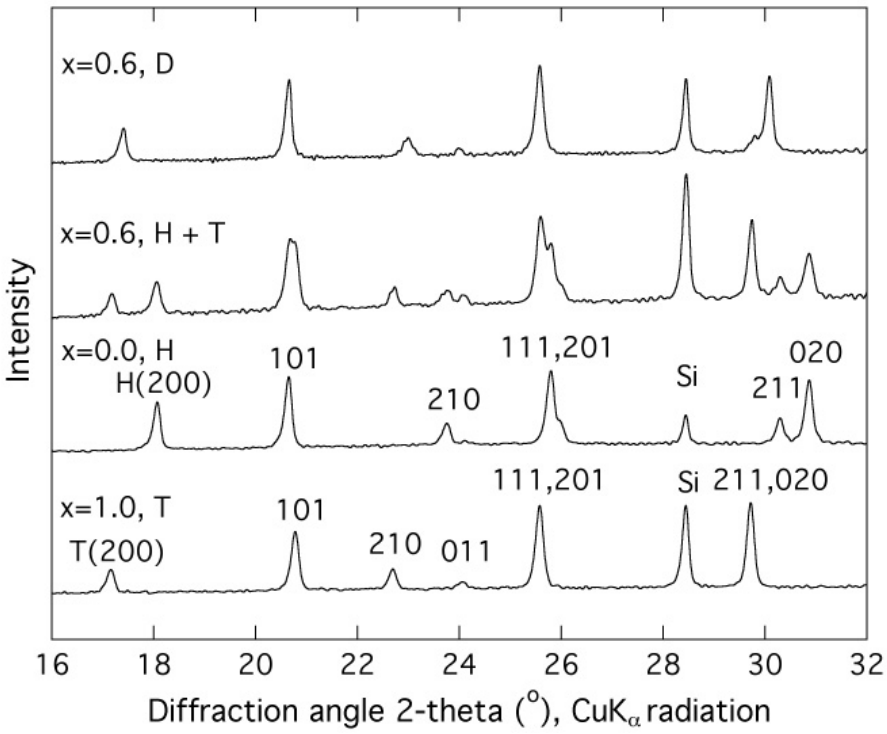

Figure 7.2: XRD patterns of Li_1FePO_4 triphylite (T), $FePO_4$ heterosite (H), and samples of Li_xFePO_4 prepared as hetrosite plus triphylite (H+T), and as disordered solid solution (D).

The Mössbauer spectrum of the two-phase mixture of Li_xFePO_4 is well known [31], and is simple to interpret as two quadrupole-split doublets; one doublet from Fe^{2+} in Li_1FePO_4 and a second doublet from Fe^{3+} in $FePO_4$. For our two-phase sample of $Li_{0.6}FePO_4$, there was little difference between the Mössbauer spectra measured at 25 and 200 °C, other than a

slight peak broadening with temperature. On the other hand, the disordered solid solution of $Li_{0.6}FePO_4$ showed a big change at temperatures between 130 and 240 °C. Figure 7.3 shows Mössbauer spectra from the two-phase sample and the disordered solid solution at various temperatures.

The Mössbauer spectra were fit with two Lorentzian doublets corresponding to the Fe^{2+} and Fe^{3+} in the sample. For each doublet the amplitudes and peak widths were constrained to be equal, but the peak width, amplitude, splitting and centroid were allowed to vary. For the two-phase sample measured at room temperature, the two doublets matched well those for Fe^{2+} and Fe^{3+} reported previously [31]. Figure 7.3 shows that the disordered solid solution at 25 °C has similar doublet positions to the two-phase material at 25 °C.

Isomer shifts and quadrupole splittings are presented for the Fe^{2+} and Fe^{3+} as functions of temperature in Figs. 7.4(a) and 7.4(b). The isomer shift is a measure of the electron density at the ^{57}Fe nucleus, and is useful for determining the valence of Fe atoms [86, 54]. In general the isomer shift does not change with temperature, except for the thermal redshift [87, 88] shown in figure 7.4(a). The isomer shift for the two-phase sample follows closely the thermal redshift, as does the isomer shift for the disordered sample up to 130 °C. There is, however, a large change in the isomer shifts for the doublets of the disordered sample between 160 and 240 °C as the isomer shifts of the Fe^{2+} and Fe^{3+} merge together. In a separate analysis, first moments, $\langle v \rangle \equiv \int vI(v)\mathrm{d}v$, were calculated from the total spectra, $I(v)$, where $I(v)$ is the number of counts at velocity v. The values of $\langle v \rangle$ were consistent with predictions of the thermal redshift for all samples, even for the spectra from the disordered solid solution at temperatures between 180 and 240 °C, indicating that the overall valence of the samples did not change with temperature.

7.4 Discussion

The anomalous temperature dependencies of the line widths, isomer shifts, and quadrupole splittings from the disordered solid solution are signatures of a "relaxation process," where a dynamical process or processes involving the ^{57}Fe occurs within the Mössbauer time window of $\tau_M = 1$ to 100 ns. Mössbauer spectra are sensitive to several dynamical processes in solids,

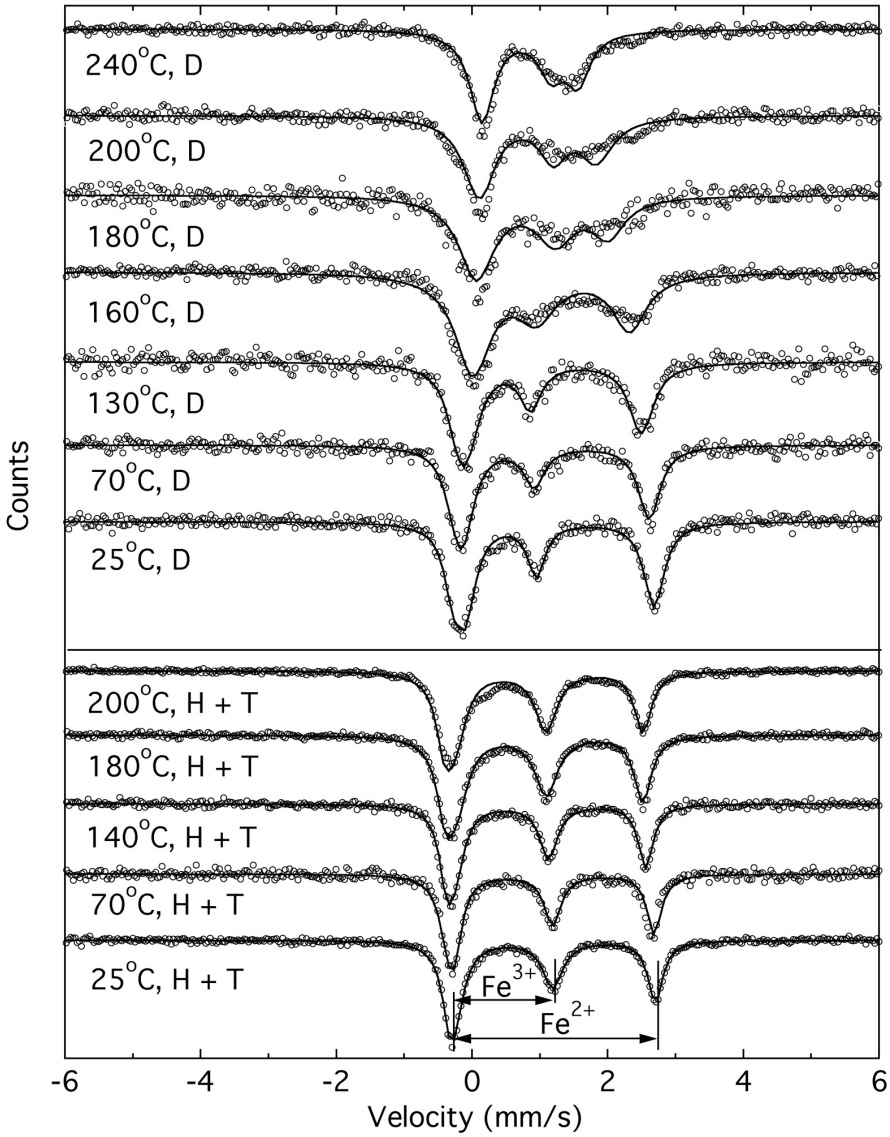

Figure 7.3: Mössbauer spectra of samples of $Li_{0.6}FePO_4$ prepared as two-phase mixture (H+T) and disordered solid solutions (D).

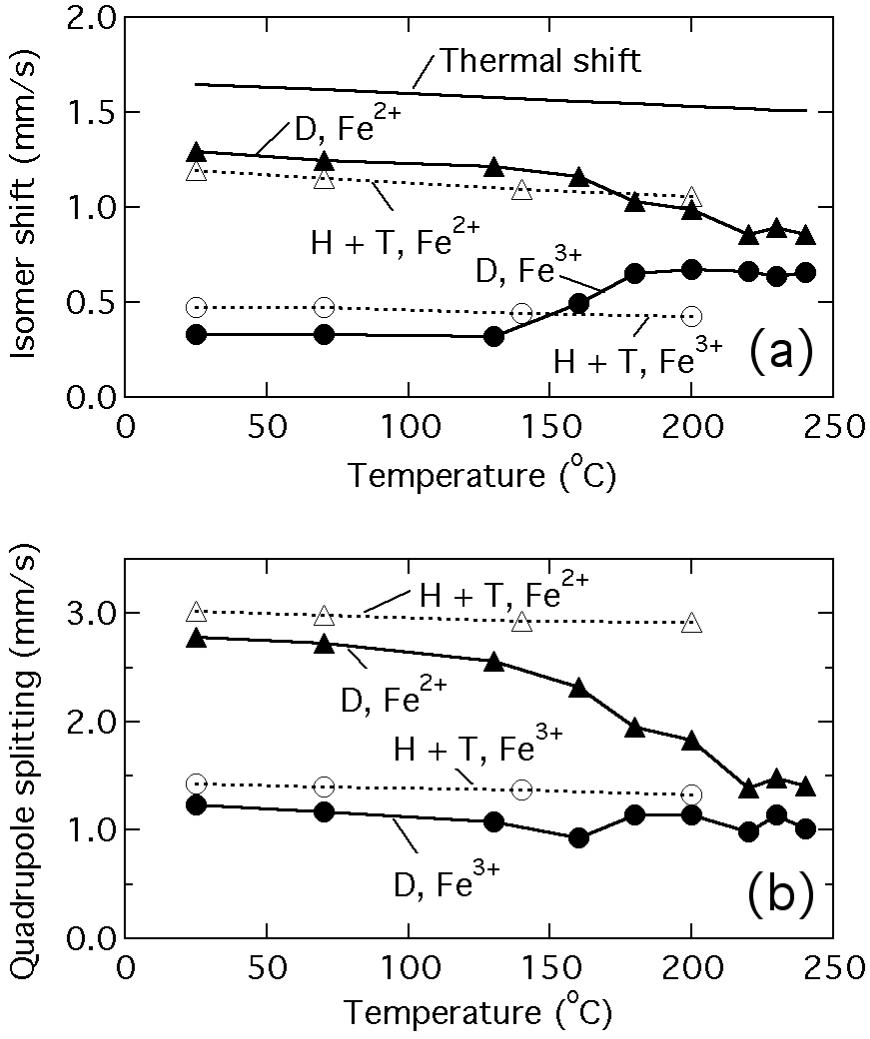

Figure 7.4: (a) Isomer shift and (b) quadrupole splitting versus temperature. Data from disordered sample labeled "D," two-phase sample labeled "H+T."

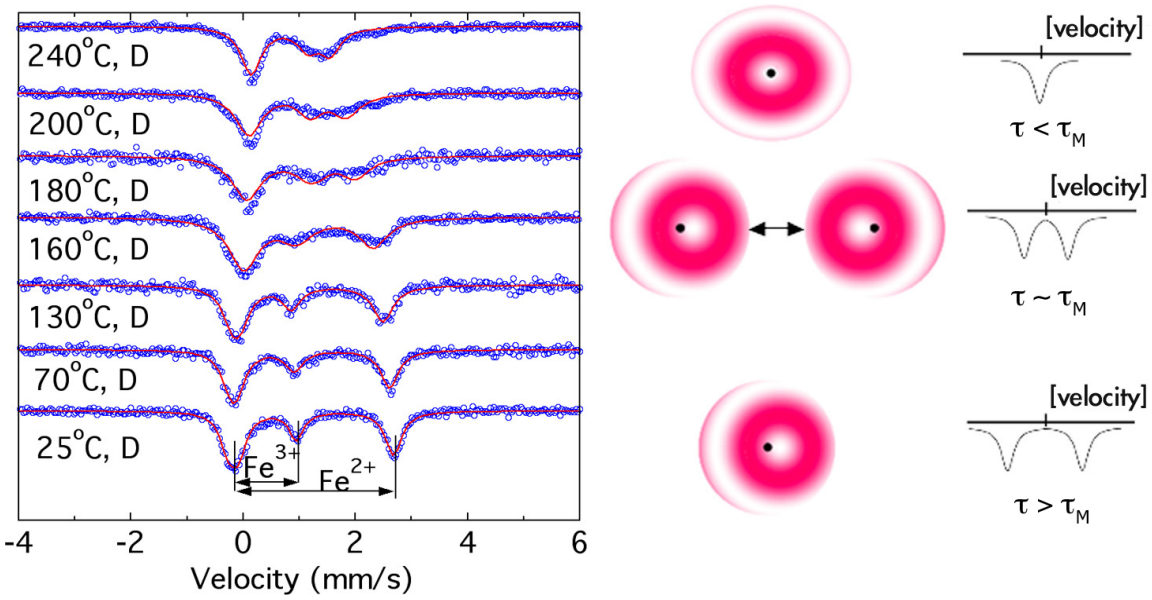

Figure 7.5: Mössbauer spectra for disordered solid solution of $Li_{0.6}FePO_4$ show valence fluctuations when heated at 130 °C and above.

including atom motions and valence fluctuations. Figure 7.5 shows the Mössbauer spectra of the disordered solid solution phase at different temperatures, along with depictions of the electron density which would be measured as the time scale of atom or valence hopping (τ) approaches the Mössbauer time window (τ_M). At around 130 °C, the Mössbauer spectra begin to show valence fluctuations as dynamics in the sample approach the time scale of 1 to 100 ns. When dynamics occur faster than the Mössbauer time window ($\tau < \tau_M$), a blur of the Fe^{2+} and Fe^{3+} valence states results.

The Mössbauer spectra of the disordered solid solution show a relaxation from 130 to 200 °C as a reduction of the quadrupole splitting, especially for the Fe^{2+} doublet (Fig. 7.4b). At slightly higher temperatures, the isomer shifts of the two doublets begin to merge (Fig. 7.4a). Owing to their similar temperature ranges, it is possible that the merging of the isomer shifts and the fluctuations of the electric quadrupole splittings originate with the same underlying physical process. Candidate processes are the motion of Li^+ ions, and charge hoppings from Fe^{2+} to Fe^{3+}, although these two processes are plausibly interrelated.

It is interesting, however, that after accounting for the thermal redshift, the relaxation of the electric quadrupole splittings starts at a lower temperature than the isomer shifts.

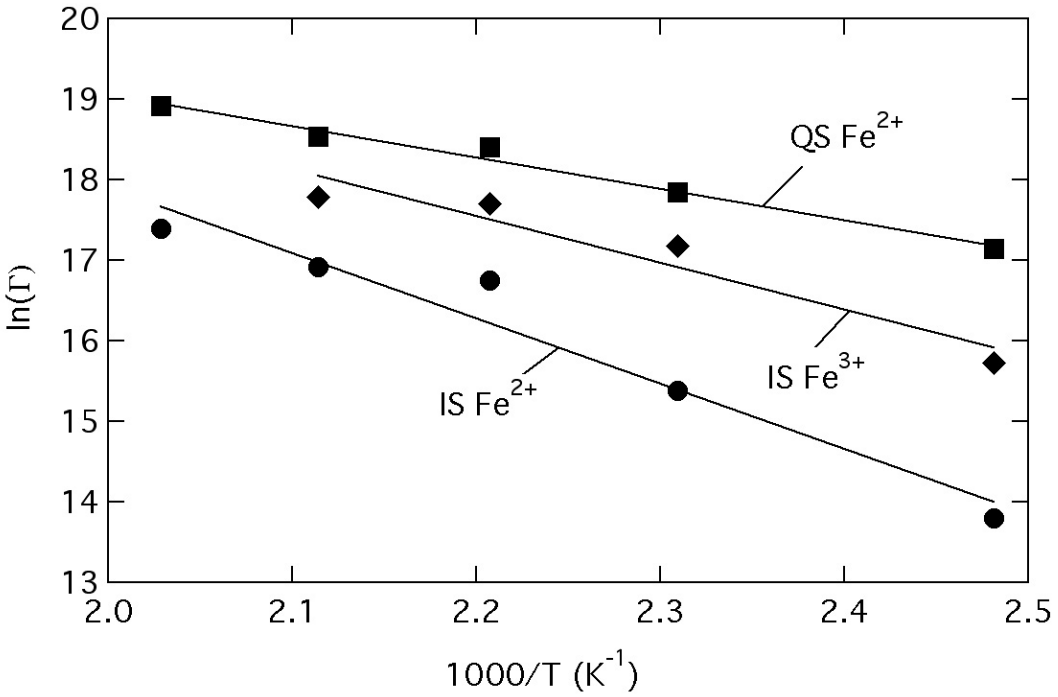

Figure 7.6: Arrhenius plot of $\ln(\Gamma)$ vs. $1000/T$ using hopping frequencies obtained from Fe^{2+} quadrupole splitting energies (QS) and from isomer shift energies of Fe^{2+} and Fe^{3+} (IS). Isomer shift energies are scaled with respect to their values at room temperature accounting for the thermal redshift.

This observation is supported by Arrhenius plots of the form

$$\Gamma(T) = \nu \, \mathrm{e}^{-E^*/k_\mathrm{B}T} \, , \tag{7.1}$$

where $\Gamma(T)$ is a rate, equal to an inverse characteristic time $1/\tau$. The characteristic relaxation time is $\tau = h/\Delta E$. The temperature range for the relaxation of the electric quadrupole splitting is between 130 and 220 °C. Taking the difference in quadrupole splitting energies at room temperature and temperature T as ΔE, we plot the relaxation of the Fe^{2+} electric quadrupole splitting as $\ln(\Gamma)$ vs. $1/T$ in Fig. 7.6. A straight line gives a good fit, with an R^2 value of 0.98, an activation energy E^* of 335 ± 25 meV, and an attempt frequency ν of 5×10^{11} Hz. This activation energy exceeds those for free polarons and free Li ions (175-270 meV) [32, 82], as expected, since it includes binding between Li ions and polarons.

Arrhenius plots for the isomer shift were less reliable because the measured effects were smaller. From 130 to 200 °C the activation energies were 700 and 500 meV with attempt frequencies 6×10^{14} and 1×10^{13} Hz for Fe^{2+} and Fe^{3+}, respectively (Fig. 7.6). The errors in activation energy were ±100 meV and the values of R^2 were around 0.92. Because charge is conserved, the relaxations for the Fe^{2+} and Fe^{3+} subspectra should have the same activation energy, and this is possible within the error bars of the measurement. These activation energies are within the range measured experimentally by others for lithium diffusion in $LiFePO_4$ (400-690 meV) [21, 89], and give us room-temperature diffusion coefficients of 8×10^{-13} to 3×10^{-11} cm^2/s.

In another Mössbauer study on $LiFePO_4$, Ellis et al. reported an activation energy of 775 ± 108 meV, which is a bit higher than our results [85]. They measured relaxations of Mössbauer spectra in a higher temperature regime than we did (between 220 and 400 °C), starting with two-phase materials composed of heterosite and triphylite. Since the kinetics of lithium disordering is slow between 200 and 300 °C, their samples were a mixture of phases during measurements in that temperature range. They looked at the narrowing of the disordered solid solution phase line width vs. temperature for 280-400 °C to calculate the activation energy for Fe valence hopping, which is presumed to be correlated to lithium hopping. The source of dynamics of the line width is unclear and could originate from different mechanisms than our measurements of the isomer shift and quadrupole splitting. One possible explanation for the narrowing line width could be homogenization of quadrupole splitting as the temperature is raised.

Ionic and polaronic motions should be coupled [82], so it is expected that lithium ion movement correlates with Fe^{2+} valence movement. It appears that the ionic mobility can account for the electrical conductivity in the material. Using our values of activation energy and diffusion coefficients, and the Nernst-Einstein relation,

$$\sigma = c_i D_i \left(\frac{Z_i^2 e^2}{kT} \right) , \tag{7.2}$$

where c_i is the concentration, D_i is the diffusion constant, and Z is the charge of Li^+, we can relate these diffusion coefficients for Li^+ to the electrical conductivity of the material,

resulting in values of 10^{-6} to 10^{-4} S/cm. These conductivity values are much larger than the 10^{-9} S/cm values previously measured for fully lithiated $LiFePO_4$ [30, 36].

The isomer shift and the electric quadrupole splitting need not have the same activation energy, however. A possible difference could occur if the Li^+ ion were to hop back and forth between two sites having the same Fe^{2+} neighbor. This would change the direction of the electric field gradient at the ^{57}Fe, but the ^{57}Fe valence, and its isomer shift, would not change. With higher temperature, however, we would expect migration of the Li^+ ion to affect both the quadrupole splitting and the isomer shift, and indeed these two quantities show the same trend at the highest temperatures.

The line widths for the Lorentzian peak fits to the Mössbauer spectra are presented in Fig. 7.7. The changes are small on the scale of the velocity range of the Mössbauer spectra. The peak width for the disordered sample is a maximum around 160 °C, but no trend can be seen for the two-phase sample. Usually the broadening of Mössbauer line widths, ΔE, is associated with diffusional movements of atoms with characteristic time τ through the uncertainty relation $\tau = \hbar/\Delta E$. A second criterion is that the amount of motion of the ^{57}Fe atom must be comparable to the wavelength of the photon. In the case of Li_xFePO_4, it is not expected that the ^{57}Fe atoms will be undergoing rapid diffusional motion, although there is a small displacement owing to differences in the distances and angles to the oxygen atoms around the Fe^{2+} and Fe^{3+}. This is not a big effect, however. Even more puzzling is the decrease in line width at temperatures above 160 °C. This cannot be explained by a mechanism of rapid atom movements, especially considering the high frequencies of phonons in comparison to the Mössbauer timescale. Instead, we attribute the broadening shown in Fig. 7.7 to inhomogeneities in the larger relaxations of the electric quadrupole splitting, associated with possible variations in temperature or composition. The peak in the line-width plot of Fig. 7.7 is at the temperature where the electric quadrupole splitting is changing most rapidly (Fig. 7.4(b)).

Figure 7.3 shows that the average dynamical processes at ^{57}Fe in either the triphylite or heterosite in the two-phase sample are clearly slower than in the disordered sample. In the two-phase sample, only minor relaxations are evident at 180 and 200 °C, and much of the behavior at 200 °C may be caused by the presence of a small amount of disordered phase

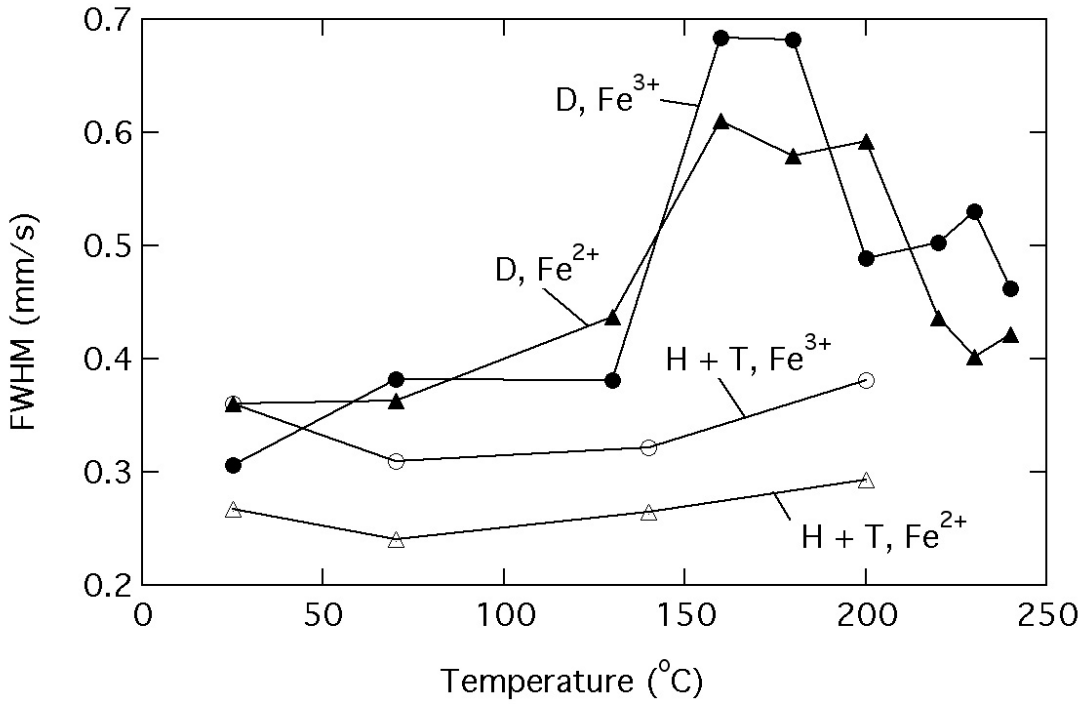

Figure 7.7: line widths of the peaks used in spectral fitting versus temperature. Data from disordered sample labeled "D," two-phase sample labeled "H+T."

that was found after the sample was cooled to room temperature. It is possible, however, that in the vicinity of local defects in the triphylite or heterosite (vacancies or isolated Li^+ ions, respectively), the dynamical processes are similar to those in the disordered sample. These defect concentrations should be around 10% for $Li_{0.6}FePO_4$ at room temperature, according to Yamada et al. [51]. By adding a spectral contribution of 10% in area from the disordered sample to the spectrum of the two-phase sample measured at 140 °C, we could account for the broadening of the Mössbauer peaks at 180 °C in the two-phase sample (see Fig. 7.8). It is likely that a higher concentration of defects would be present at 180 °C, however, suggesting that the dynamical processes around defects in the two-phase sample may be a bit slower than in the disordered sample.

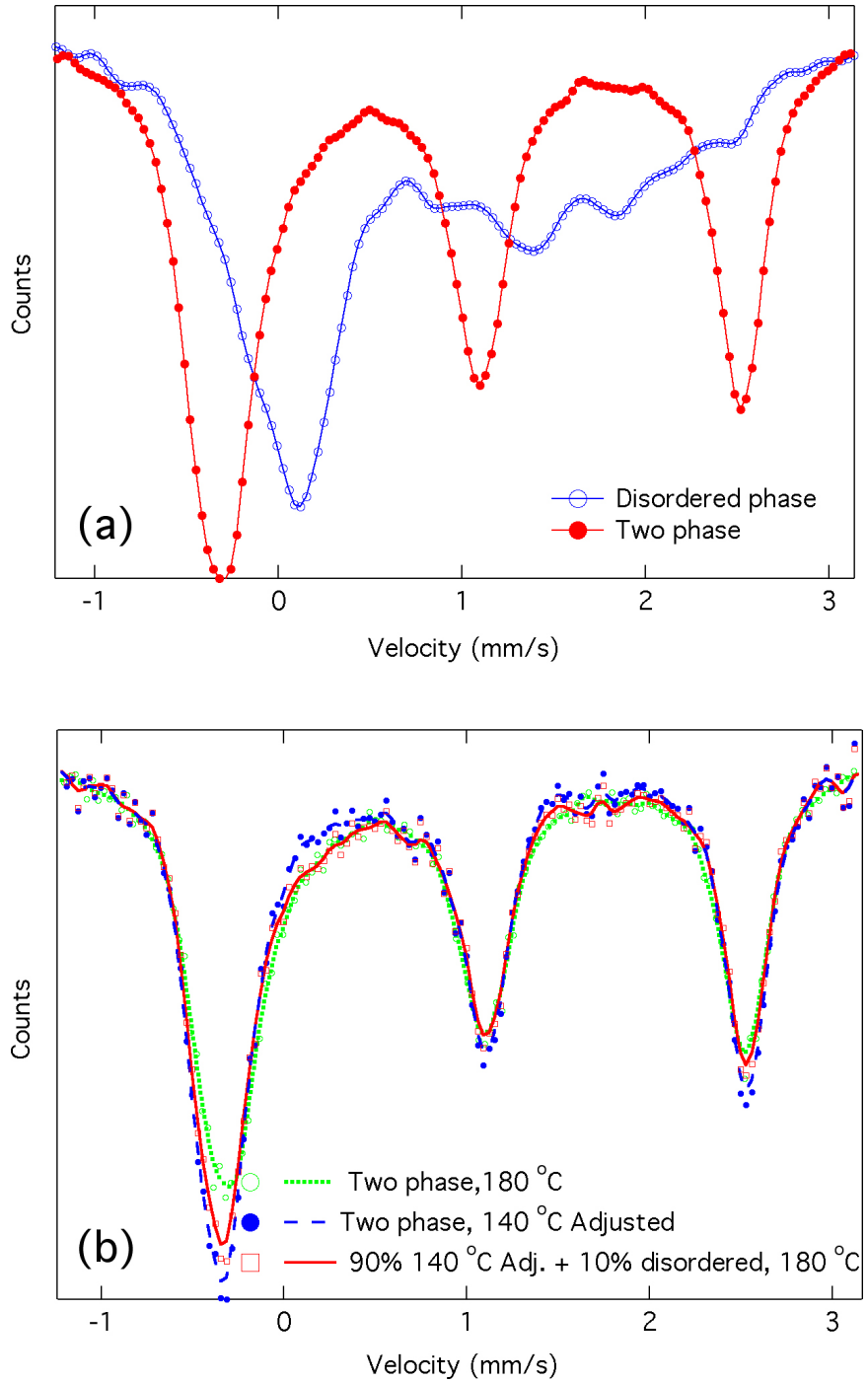

Figure 7.8: (a) Comparison of Mössbauer spectra for disordered phase and two-phase material at 180 °C. (b) Spectrum of two-phase sample at 180 °C is compared to spectrum at 140 °C, adjusted to thermal shift at 180 °C. There is a slight shoulder in the data which is consistent with the first peak of the 180 °C disordered phase measurement, indicating that 10% of the Fe in the material has valence fluctuation.

7.5 Conclusion

We have found substantial valence fluctuations in the disordered solid solution compared to the two-phase mixture of $Li_{0.6}FePO_4$. In the disordered solid solution phase, starting at around 130 °C, the quadrupole splitting of the Fe^{2+} doublet decreases. At a slightly higher temperature a merging of the isomer shifts of the Fe^{2+} and Fe^{3+} doublets begins. The change of the electric field gradient at a slightly lower temperature than the change in isomer shift can be explained by Li^+ hopping, first around the same Fe^{2+} atom, and then at higher temperatures as a diffusive motion, such that valence changes would occur. Relating the valence fluctuations to the electrical conductivity of the material gives values of 10^{-6} to 10^{-4} S/cm, 3 to 5 orders of magnitude higher than the measured value of 10^{-9} for fully lithiated $LiFePO_4$. Thus, if the disordered solid solution phase could be stabilized at cell operating temperature, and lithium could cycle electrochemically in this single phase, the cell rate capability could be improved substantially.

Chapter 8

Conclusions

8.1 Summary

There is still a great deal to be learned about $LiFePO_4$ as a cathode material for lithium-ion batteries. In the past few years many improvements have led to consistent cycling capabilities, even at high rates. $LiFePO_4$ is being commercialized as a cathode material in batteries for power tools, and is a serious candidate for the future batteries of hybrid-electric or electric vehicles. It can also be commercialized for other applications requiring a low-cost and safe battery.

Nevertheless, there is still room for improvement. At this point, many groups have shown good performance by addition of carbon, during synthesis or by later carbon coating through various techniques to improve electrical conductivity. Simplification or even minimization of carbon-coating methods is one area of improvement which could help to reduce cost. This can be achieved through improvement of the intrinsic material conductivity.

The phase composition during electrochemical cycling is still a topic of interest which is not fully understood. The mechanism of the transformation between the two phases (triphylite and heterosite) becomes more complicated as particle sizes approach nanometer dimensions. This appears to be a good thing, since improved results have been found with nanoparticles, probably both due to faster kinetics with shorter length scales, and also a change in the phase composition and cycling mechanisms. $LiFePO_4$ was initially believed to only be capable of cycling at low rates due to its poor kinetics and low electrical conductivity. However, now it is touted as a high-rate capability material, due to several

methods of improvement (these were discussed in section 2.4).

In this work, we have probed the phase composition up to a temperature of 800 °C. The triphylite phase is quite stable even up to 800 °C, however, the heterosite (delithiated) phase is unstable above 400 °C. It is important to note the phases formed due to phase instability, since they could eventually form after a long-time cycling of the cathode.

Between room temperature and 400 °C, the phase diagram of Li_xFePO_4 was determined. The phase diagram is eutectoid-like, with the eutectoid point at $x = 0.6$ and 200 °C. Knowing the increased stability of the disordered phase at $x = 0.6$ allowed further studies of this phase at lower temperatures. We found some exciting dynamics in the material through a Mössbauer spectrometry experiment. Comparing the two-phase material to a quenched disordered solid solution at elevated temperatures showed much faster dynamics in the disordered phase.

Finally, we measured the entropy and enthalpy of lithiation in both $LiFePO_4$ and $LiMn_{0.2}Fe_{0.8}PO_4$. The thermodynamic measurements gave us some insight about probable phase boundaries, but this system is actually quite complicated. For the intermediate region (for Li_xFePO_4, $0.05 < x < 0.85$) we do not see a flat $\Delta S(x)$ as would be expected for a normal two-phase system. It is possible that interface contributions, thermal strain effects, or non-equilibrium conditions could be the cause for such abnormality. Further investigations these areas of analysis would help in understanding the operation mechanisms of lithium insertion into and extraction from $LiFePO_4$.

8.2 Future Work

8.2.1 Further Characterization of Disordered Solid Solution of Li_xFePO_4

8.2.1.1 Mössbauer spectrometry

We have studied the dynamics of the $Li_{0.6}FePO_4$ material, both in the two-phase and disordered solid solution phase. We found interesting results, with a change in the electric quadrupole splitting beginning at 130 °C, as well as isomer shift merging beginning at 160 °C, indicating valence fluctuation on the time scale of Mössbauer spectrometry. Further work can be done to understand lithium or electron motion in the disordered solid solution

phase for other fractions of lithium ($0 < x < 1$). In addition it would be interesting to see the particle size dependence of the effect.

8.2.1.2 Li-Nuclear Magnetic Resonance Spectroscopy (Li-NMR)

Another future study of potential importance would be to determine lithium motion in the material by measuring motional narrowing of the Li-NMR signal with increasing temperature. We made an attempt at this study. However, we found very broad peaks, and no evidence of motional narrowing. The coupling of the paramagnetism of Fe with the Li nucleus probably causes the broadened spectra. Therefore, measurements in a smaller magnetic field (less than 4.7 T) would help to reduce this coupling, and we can possibly separate the nucleus and paramagnetic effect.

8.2.1.3 Conductivity Measurements

We are currently collaborating with the Laboratory for Electrostatics and Dielectric Materials (LEMD-CNRS) in Grenoble, France, on conductivity measurements of $LiFePO_4$ materials at temperatures between room temperature and 310 °C. We are interested in determining whether the disordered solid solution phase has a higher conductivity compared to the two-phase mixture. Preliminary results are promising, although further work is necessary before making conclusions.

8.2.2 Stabilization of Disordered Solid Solution

The disordered solid solution phase has promise for faster kinetics and higher electrical conductivity compared to the regular two-phase mixture of $LiFePO_4/FePO_4$. If it could be cycled as a single phase cathode vs. lithium, it could have considerably better rate capability compared to the current material. The disordered solid solution phase Li_xFePO_4 is stable above 200 °C. Unfortunately, at this time, cycling a lithium-ion cell at 200 °C does not seem practical. Even if it were possible, maybe with future generation polymer electrolytes, such an elevated temperature is much higher than any likely application would desire.

It is difficult to model this system by ab-initio electronic structure calculations due to its large unit cell, so a systematic study of different compositions would be useful. Doping,

or substitution with transition metals to the left or right of Fe on periodic table, namely Mn, Co, Cr, or Ni, could be useful in stabilizing the disordered solid solution.

At room temperature, the heterosite and triphylite phases are the thermodynamically stable phases. However, kinetics are so slow that after a disordered solid solution phase is quenched to room temperature, it remains stable for several months! Due to the quasi-stability of the disordered phase at room temperature, cycling this phase vs. lithium was attempted. Figure 8.1 compares charge and discharge profiles for samples which were quenched disordered solid solution phase at $x = 0.6$ and two-phase samples from the same powder (without disordering). The cells were cycled at a C/5 rate, with the C-rate based on the active material weights and the theoretical capacity of 170 mAh/g. With this $LiFePO_4$ material, the two-phase control sample reached 140 mAh/g (no special carbon-coating techniques were used for these electrodes). The disordered phase cell reached only around 30 mAh/g for the first two cycles. By reducing the rate to C/20 for subsequent cycles, the disordered phase cells cycled with around 60 mAh/g capacities. Analysis of XRD patterns of the disordered phase electrode after electrochemical cycling (figure 8.2) showed that the disordered phase reverted to the heterosite and triphylite phases. Therefore, we could not determine whether the disordered phase has a higher rate capability than the two-phase mixture since it is not thermodynamically stable at room temperature. We would need to stabilize the disordered phase or measure its rate capability at elevated temperature.

Overall, there are still many exciting areas of study dealing with the $LiFePO_4$ cathode material.

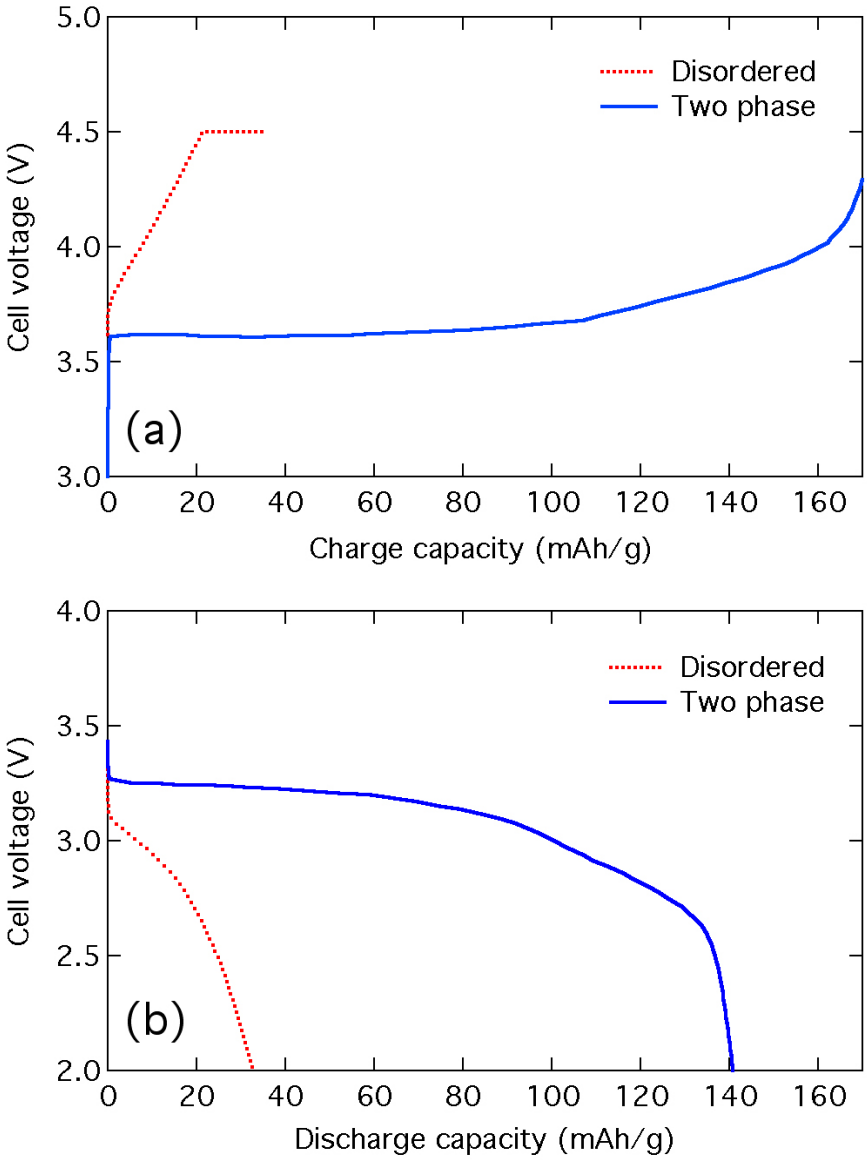

Figure 8.1: Charge (a) and discharge (b) profiles comparing the first cycle of a disordered phase electrode to a two-phase electrode. The electrodes were cycled vs. lithium, at a C/5 rate.

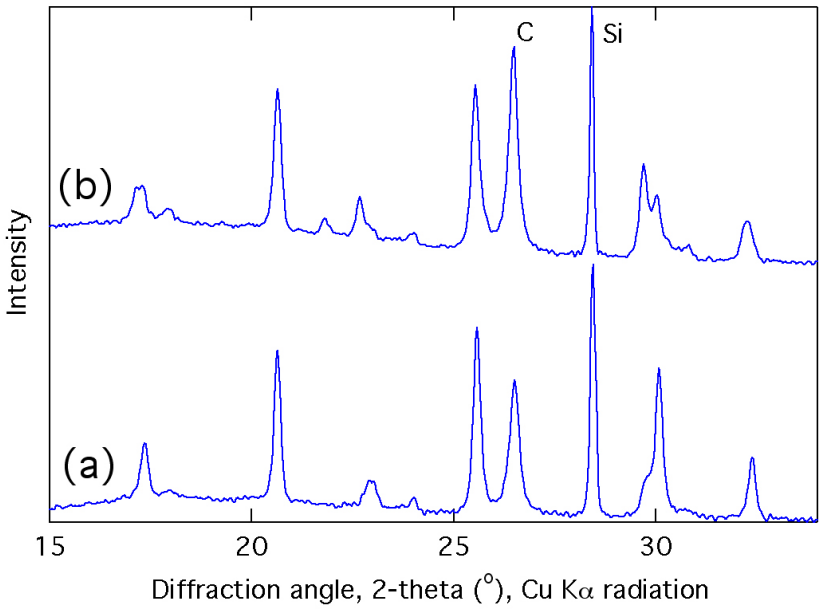

Figure 8.2: XRD patterns of the disordered phase electrode before cycling (a) and after cycling (b) at C/5 then C/20 rates. The patterns show a reversion of the disordered solid solution to the heterosite and triphylite phases. Rietveld refinement showed only 35% of disordered phase remaining after the electrode was cycled.

Appendix A

High Pressure Measurements of $LiFePO_4$

A.1 Introduction

The elastic properties of $LiFePO_4$ are an important contributor to a better understanding of the material's thermodynamic properties. Since the $LiFePO_4$ crystal structure is anisotropic, material strains could play an important role during charge and discharge of the material. We measured the bulk modulus of Li_xFePO_4 materials with compositions $x = 0$, 0.6, and 1 to see the effect of lithiation on material compressibility. We were also very interested in seeing the phase stability of this material under pressure. Samples with intermediate x (between 0 and 1) consist of a two-phase mixture at room temperature, heterosite ($FePO_4$) and triphylite ($LiFePO_4$). When heated to temperatures above 200 °C, the two phases merge to form one, which we term a disordered phase, since it is a disordered solid solution with lithium mixed throughout the structure, rather than separated into only the triphylite phase. For this study, samples with different lithium contents were prepared, and a $Li_{0.6}$FePO4 sample was heat-treated and quenched to obtain the disordered phase at room temperature. At composition $x = 0.6$ we have found the disordered phase to be especially stable, which is the reason for our choice of this composition. It would be interesting to see whether the disordered phase is the more stable phase at high pressure as well as high temperature, or if the two-phase system has a higher stability at high pressures.

A.2 Experimental

The $LiFePO_4$ samples used in high pressure studies were prepared as discussed in section 3.3. X-ray powder diffraction measurements were taken at ambient pressure with a PANalytical X'Pert PRO X'Celerator D500, using Cu-K_α radiation.

High-pressure energy dispersive x-ray diffraction studies were performed at the X17 beamline of the National Synchrotron Light Source (NSLS) at Brookhaven National Laboratory. X-ray diffraction patterns were measured at several values of pressure, at between 0 and 30 GPa. The pressure was applied using a Merrill-Bassett, 'Tel-Aviv'-type diamond-anvil-cell (DAC) and measured by the fluorescence ruby technique, with similar techniques as described by Halevy et al. [90]. Specifically, diamonds with 500 μm culets were used. Stainless steel gaskets were indented with the diamonds and 150 μm holes were drilled through the center of the gasket indentation before high pressure measurements. The sample was placed in the center of the 150 μm hole, along with several ruby chips and natural mineral oil, which was employed as a pressure medium. The pressure on the sample was measured before and after each set of scans by the ruby fluorescence technique [91] to confirm pressure stability during the measurement. The data at NSLS was collected with a Ge detector at a fixed Bragg angle ($2\theta = 13\,^\circ$).

A.3 Results

The materials used in the high-pressure experiment were measured with the PANalytical X'Pert PRO X'Celerator. These XRD patterns are shown in figure A.1. Rietveld refinement was used to determine the phase composition of the samples.

XRD patterns measured at various pressures are compiled for each sample in figures A.2, A.3, A.4 and A.5. These measurements were all done at the NSLS facility at Brookhaven National Lab, using a diamond-anvil-cell to increase pressure. As expected, the unit cell volumes decreased for all samples as the pressure was increased. The two-phase $Li_{0.6}FePO_4$ remained a two-phase system and did not indicate a disordering of lithium to form a single phase as pressure was increased. From these results, it does not seem that pressure instigates the mixing of lithium in Li_xFePO_4.

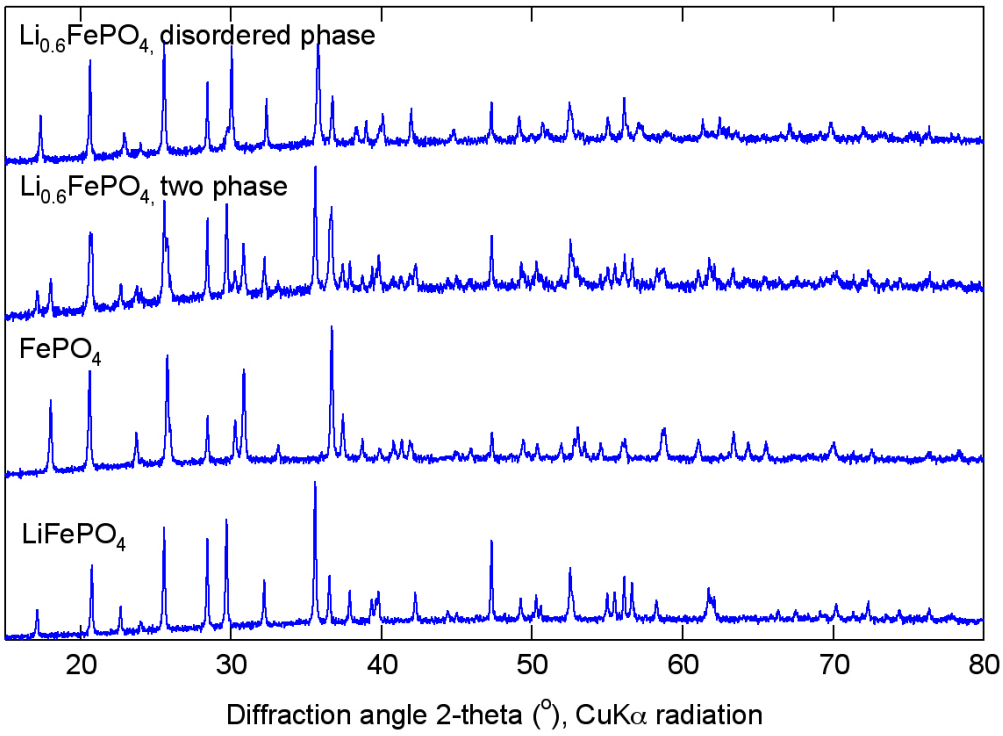

Figure A.1: XRD patterns of triphylite ($LiFePO_4$), heterosite ($FePO_4$), $Li_{0.6}FePO_4$ two-phase and $Li_{0.6}FePO_4$ disordered phase materials.

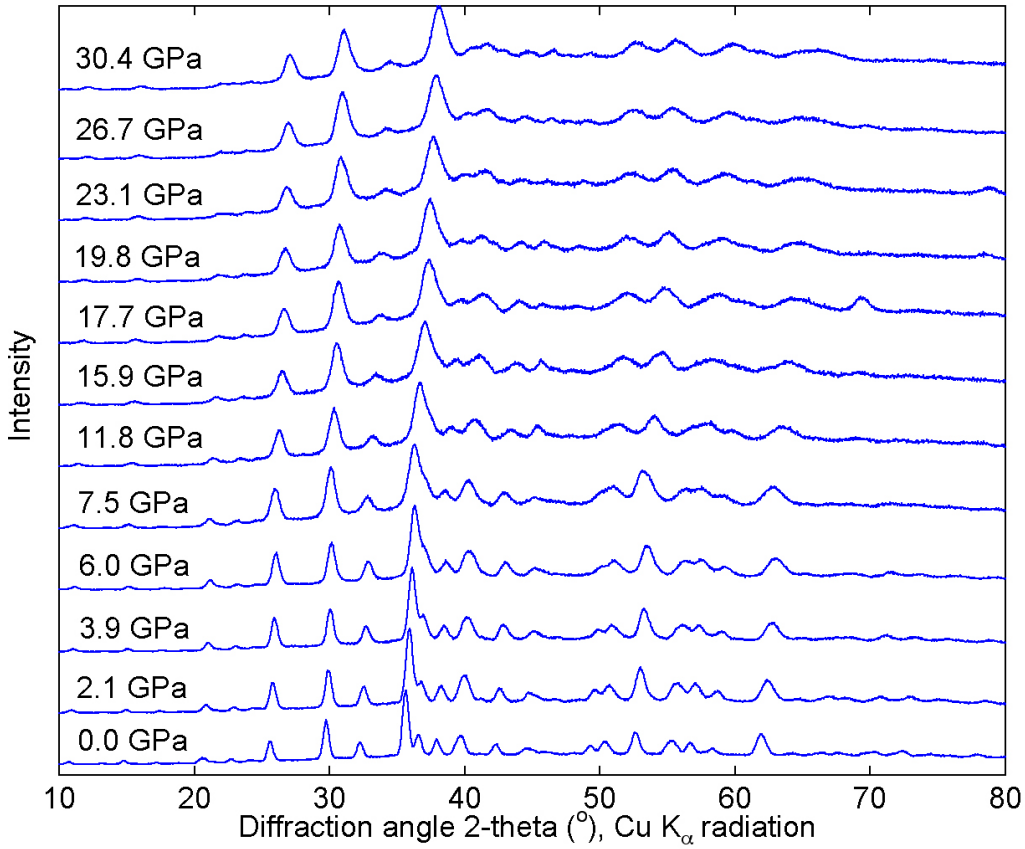

Figure A.2: XRD patterns of triphylite ($LiFePO_4$) material at various pressures.

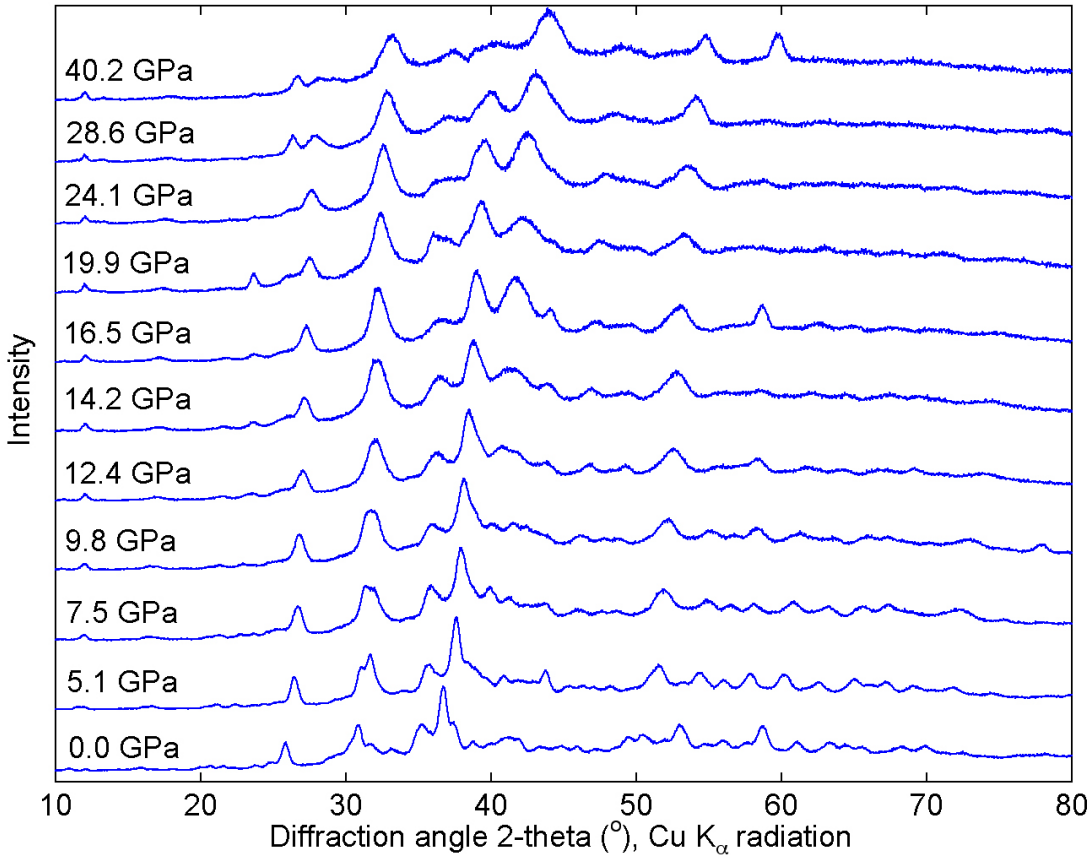

Figure A.3: XRD patterns of heterosite ($FePO_4$) material at various pressures.

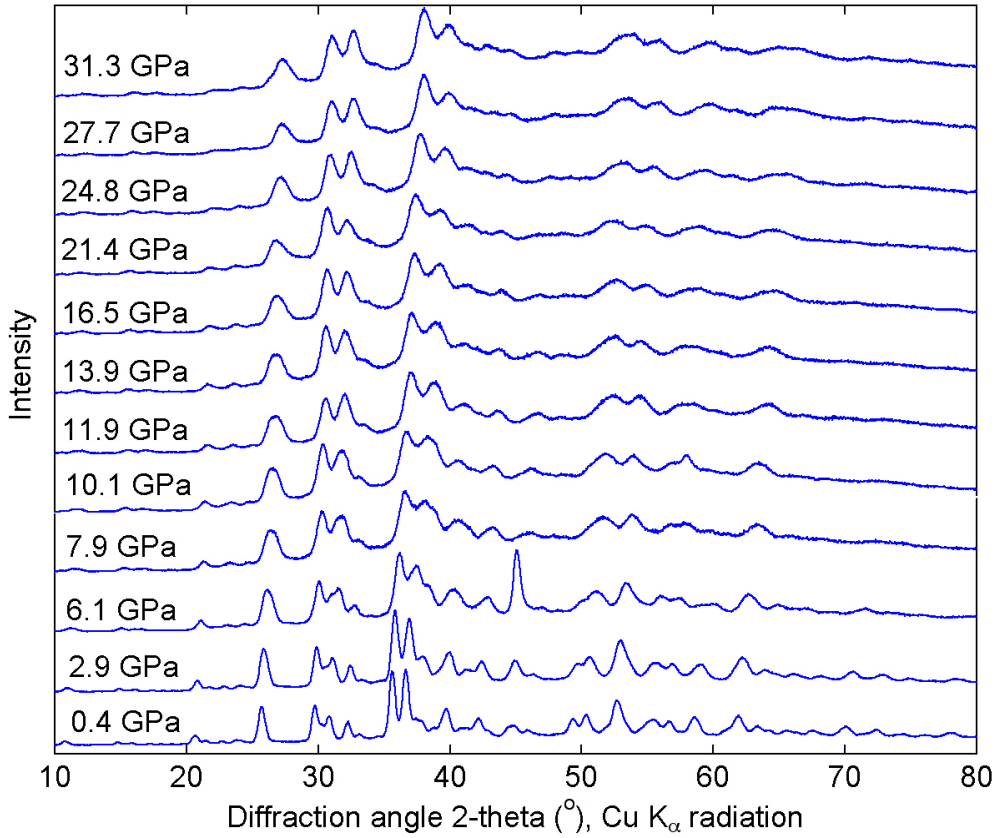

Figure A.4: XRD patterns of two-phase $Li_{0.6}FePO_4$ material at various pressures.

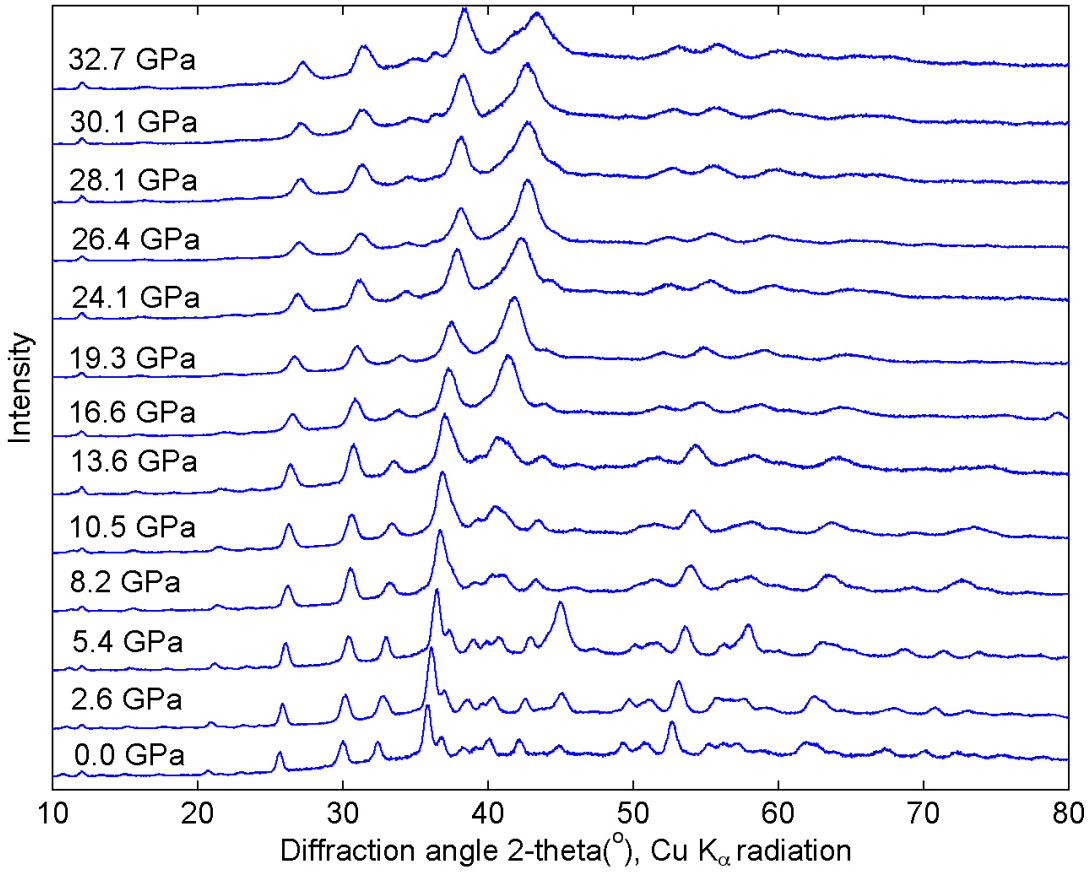

Figure A.5: XRD patterns of disordered-phase $Li_{0.6}FePO_4$ material at various pressures.

After Rietveld refinement of the XRD patterns at all different pressures, the elastic properties of the material could be examined further. In comparing the effect of pressure on the a, b, and c directions, it is apparent that the a direction is affected most and the b direction is affected least by pressure. Figure A.6 summarizes the relative values of a, b, and c lattice parameters vs. their values at zero pressure.

The relationship between pressure and volume change was fit with the modified Vinet equation of state [92] shown in equation A.1:

$$P = 3 * B * (V/V_0)^{-2/3} * \left(1 - (V/V_0)^{1/3}\right) * exp\left(3/2 * (B' - 1)\left(1 - (V/V_0)^{1/3}\right)\right), \quad \text{(A.1)}$$

where P is pressure, V is cell volume, V_0 is cell volume at zero pressure, B is the bulk modulus, and B' is $\frac{\partial B}{\partial P}_{P=0}$. From this equation, the bulk modulus of $LiFePO_4$, $FePO_4$ and disordered phase $Li_{0.6}FePO_4$ were computed to be 106 ± 8, 61 ± 3, and 120 ± 4 GPa, respectively. The values for $LiFePO_4$ and $FePO_4$ correspond well with values calculated by first principles by Maxisch et al. [81]. Their values were 96 GPa for $LiFePO_4$ and 66 GPa for $FePO_4$.

A.4 Conclusion

High pressure measurements were used to determine the elastic properties of $LiFePO_4$ materials, finding that the fully delithiated material, $FePO_4$ is a much softer material, with bulk modulus of 61 GPa vs. 106 GPa for $LiFePO_4$. The disordered phase $Li_{0.6}FePO_4$ material was found to be slightly stiffer than $LiFePO_4$, with a bulk modulus of 120 GPa, however, this value is not significantly different from the value for $LiFePO_4$.

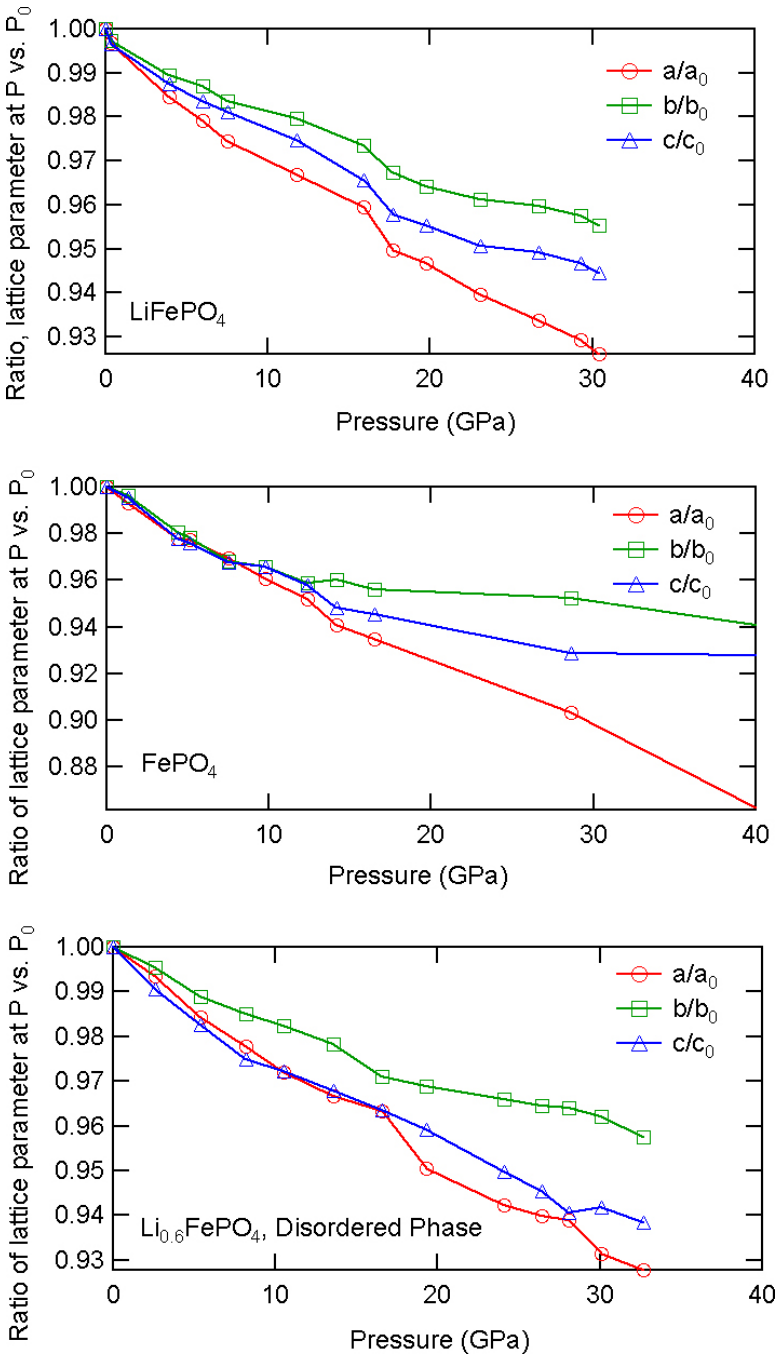

Figure A.6: Lattice parameters at pressure P compared to their values at P_0 (0 GPa), for $LiFePO_4$, $FePO_4$, and $Li_{0.6}FePO_4$.

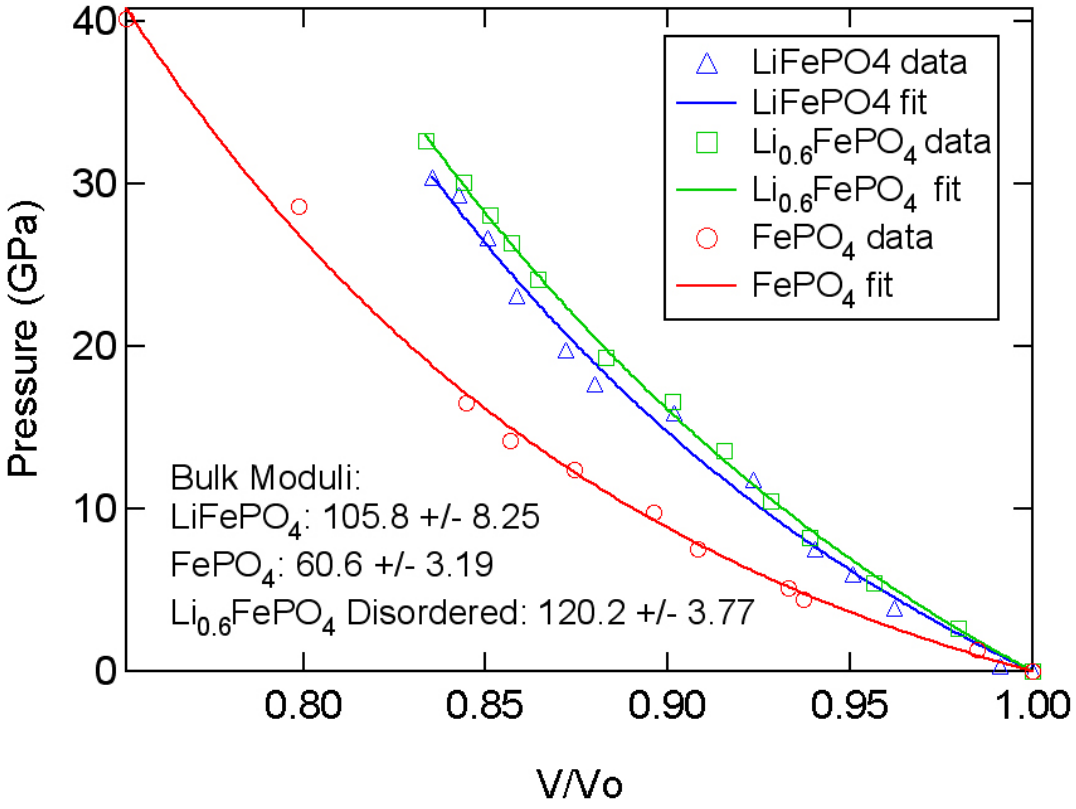

Figure A.7: Bulk moduli were computed from P vs. V/V_0 data.

Bibliography

[1] C. Julien, *Materials for Lithium-Ion Batteries*. Kluwer Academic Publishers, The Netherlands, 2000.

[2] D. Linden, *Handbook of Batteries*. McGraw-Hill, 2002.

[3] M. S. Whittingham, "Electrical energy storage and intercalation chemistry," *Science* **192** (1976) 1126–1127.

[4] K. Mizushima, P. C. Jones, P. J. Wiseman, and J. B. Goodenough, "Li_xCoO_2 $(0 < x < 1)$—A New Cathode Material for Batteries of High-Energy Density," *Mater. Res. Bull.* **15** (1980) 783–789.

[5] I. Belharouak, W. Q. Lu, D. Vissers, and K. Amine, "Safety characteristics of $Li(Ni_{0.8}Co_{0.15}Al_{0.05})O_2$ and $Li(Ni_{1/3}Co_{1/3}Mn_{1/3})O_2$," *Electrochem. Comm.* **8** (2006) 329–335.

[6] M. S. Whittingham, "Lithium batteries and cathode materials," *Chemical Reviews* **104** (2004) 4271–4301.

[7] M. Y. Saidi, J. Barker, H. Huang, J. L. Swoyer, and G. Adamson, "Electrochemical properties of lithium vanadium phosphate as a cathode material for lithium-ion batteries," *Electrochem. Solid-State Lett.* **5** (2002) A149–A151.

[8] E. Plichta, S. Slane, M. Uchiyama, M. Salomon, D. Chua, W. B. Ebner, and H. W. Lin, "An improved Li/Li_xCoO_2 rechargeable cell," *J. Electrochem. Soc.* **136** (1989) 1865–1869.

[9] M. G. S. R. Thomas, W. I. F. David, J. B. Goodenough, and P. Groves, "Synthesis and structural characterization of the normal spinel $Li[Ni_2]O_4$," *Mater. Res. Bull.* **20** (1985) 1137–1146.

[10] C. Delmas and I. Saadoune, "Electrochemical and physical-properties of the $Li_xNi_{1-y}Co_yO_2$ phases," *Solid State Ionics* **53-6** (1992) 370–375.

[11] T. Ohzuku and Y. Makimura, "Layered lithium insertion material of $LiCo_{1/3}Ni_{1/3}Mn_{1/3}O_2$ for lithium-ion batteries," *Chem. Lett.* (2001) 642–643.

[12] B. Scrosati, *Electrochemistry of Novel Materials*, ch. X. Insertion Compounds for Lithium Rocking Chair Batteries, pp. 111–140. Wiley-VCH, New York, NY, 1994.

[13] A. K. Padhi, K. S. Nanjundaswamy, and J. B. Goodenough, "Phospho-olivines as positive-electrode materials for rechargeable lithium batteries," *J. Electrochem. Soc.* **144** (1997) 1188–1194.

[14] A. Manthiram, *Lithium Batteries Science and Technology*, ch. 1, pp. 3–41. Kluwer Academic Publishers, Norwell, Massachusetts, 2004.

[15] R. Yazami and P. H. Touzain, "A reversible graphite-lithium negative electrode for electrochemical generators," *J. Power Sources* **9** (1983) 365–371.

[16] T. Ohzuku, A. Ueda, and N. Yamamoto, "Zero-strain insertion material of $Li[Li_{1/3}Ti_{5/3}]O_4$ for rechargeable lithium cells," *J. Electrochem. Soc.* **142** (1995) 1431–1435.

[17] J. Graetz, C. C. Ahn, R. Yazami, and B. Fultz, "Highly reversible lithium storage in nanostructured silicon," *Electrochem. Solid-State Lett.* **6** (2003) A194–A197.

[18] J. Graetz, C. C. Ahn, R. Yazami, and B. Fultz, "Nanocrystalline and thin film germanium electrodes with high lithium capacity and high rate capabilities," *J. Electrochem. Soc.* **151** (2004) A698–A702.

[19] M. Holzapfel, H. Buqa, W. Scheifele, P. Novak, and F. M. Petrat, "A new type of nano-sized silicon/carbon composite electrode for reversible lithium insertion," *Chem. Comm.* (2005) 1566–1568.

[20] K. Amine, H. Yasuda, and M. Yamachi, "Olivine $LiCoPO_4$ as 4.8 V electrode material for lithium batteries," *Electrochem. Solid-State Lett.* **3** (2000) 178–179.

[21] M. Takahashi, S. Tobishima, K. Takei, and Y. Sakurai, "Reaction behavior of $LiFePO_4$ as a cathode material for rechargeable lithium batteries," *Solid State Ionics* **148** (2002) 283–289.

[22] D. D. MacNeil, Z. H. Lu, Z. H. Chen, and J. R. Dahn, "A comparison of the electrode/electrolyte reaction at elevated temperatures for various Li-ion battery cathodes," *J. Power Sources* **108** (2002) 8–14.

[23] A. Yamada, S. C. Chung, and K. Hinokuma, "Optimized $LiFePO_4$ for lithium battery cathodes," *J. Electrochem. Soc.* **148** (2001) A224–A229.

[24] J. R. Dahn, E. W. Fuller, M. Obrovac, and U. VonSacken, "Thermal-stability of Li_xCoO_2, Li_xNiO_2, and lambda-MnO_2 and consequences for the safety of Li-ion cells," *Solid State Ionics* **69** (1994) 265–270.

[25] A. S. Andersson, J. O. Thomas, B. Kalska, and L. Haggstrom, "Thermal stability of $LiFePO_4$-based cathodes," *Electrochem. Solid-State Lett.* **3** (2000) 66–68.

[26] N. Iltchev, Y. K. Chen, S. Okada, and J. Yamaki, "$LiFePO_4$ storage at room and elevated temperatures," *J. Power Sources* **119** (2003) 749–754.

[27] Y. Y. Xia and M. Yoshio, "Studies on Li-Mn-O spinel system (obtained from melt-impregnation method) as a cathode for 4 V lithium batteries. Part IV. High and low temperature performance of $LiMn_2O_4$," *J. Power Sources* **66** (1997) 129–133.

[28] M. Koltypin, D. Aurbach, L. Nazar, and B. Ellis, "On the stability of $LiFePO_4$ olivine cathodes under various conditions (electrolyte solutions, temperatures)," *Electrochem. Solid-State Lett.* **10** (2007) A40–A44.

[29] K. Amine, J. Liu, and I. Belharouak, "High-temperature storage and cycling of C-$LiFePO_4$/graphite Li-ion cells," *Electrochem. Comm.* **7** (2005) 669–673.

[30] S. Y. Chung, J. T. Bloking, and Y. M. Chiang, "Electronically conductive phospho-olivines as lithium storage electrodes," *Nat. Mater.* **1** (2002) 123–128.

[31] A. S. Andersson, B. Kalska, L. Haggstrom, and J. O. Thomas, "Lithium extraction/insertion in $LiFePO_4$: an x-ray diffraction and Mössbauer spectroscopy study," *Solid State Ionics* **130** (2000) 41–52.

[32] D. Morgan, A. Van der Ven, and G. Ceder, "Li conductivity in Li_xMPO_4 (M = Mn, Fe, Co, Ni) olivine materials," *Electrochem. Solid-State Lett.* **7** (2004) A30–A32.

[33] C. Y. Ouyang, S. Q. Shi, Z. X. Wang, X. J. Huang, and L. Q. Chen, "First-principles study of Li ion diffusion in $LiFePO_4$," *Phys. Rev. B* **69** (2004) 104303.

[34] L. Laffont, C. Delacourt, P. Gibot, M. Y. Wu, P. Kooyman, C. Masquelier, and J. M. Tarascon, "Study of the $LiFePO_4/FePO_4$ two-phase system by high-resolution electron energy loss spectroscopy," *Chem. Mater.* **18** (2006) 5520–5529.

[35] P. P. Prosini, "Modeling the voltage profile for $LiFePO_4$," *J. Electrochem. Soc.* **152** (2005) A1925–A1929.

[36] C. Delacourt, L. Laffont, R. Bouchet, C. Wurm, J. B. Leriche, M. Morcrette, J. M. Tarascon, and C. Masquelier, "Toward understanding of electrical limitations (electronic, ionic) in $LiMPO_4$ (M = Fe, Mn) electrode materials," *J. Electrochem. Soc.* **152** (2005) A913–A921.

[37] J. Molenda, A. Stoklosa, and T. Bak, "Modification in the electronic-structure of cobalt bronze Li_xCoO_2 and the resulting electrochemical properties," *Solid State Ionics* **36** (1989) 53–58.

[38] H. Huang, S. C. Yin, and L. F. Nazar, "Approaching theoretical capacity of $LiFePO_4$ at room temperature at high rates," *Electrochem. Solid-State Lett.* **4** (2001) A170–A172.

[39] Z. H. Chen and J. R. Dahn, "Reducing carbon in $LiFePO_4$/C composite electrodes to maximize specific energy, volumetric energy, and tap density," *J. Electrochem. Soc.* **149** (2002) A1184–A1189.

[40] N. Ravet, J. B. Goodenough, S. Besner, M. Simoneau, P. Hovington, and M. Armand in *The Electrochemical Society and the Electrochemical Society of Japan Meeting Abstracts, vol. 99-2, (Abstract no 127)*. Honolulu, HI, 1999.

[41] I. Belharouak, C. Johnson, and K. Amine, "Synthesis and electrochemical analysis of vapor-deposited carbon-coated $LiFePO_4$," *Electrochem. Comm.* **7** (2005) 983–988.

[42] D. H. Kim and J. Kim, "Synthesis of $LiFePO_4$ nanoparticles in polyol medium and their electrochemical properties," *Electrochem. Solid-State Lett.* **9** (2006) A439–A442.

[43] S. Y. Chung, J. T. Bloking, and Y. M. Chiang, "From our readers—On the electronic conductivity of phosphoolivines as lithium storage electrodes—Reply," *Nat. Mater.* **2** (2003) 702–703.

[44] N. Meethong, H.-Y. S. Huang, S. A. Speakman, W. C. Carter, and Y. M. Chiang, "Strain accommodation during phase transformations in olivine-based cathodes as a materials selection criterion for high-power rechargeable batteries," *Adv. Functional Mat.* (2007).

[45] N. Ravet, A. Abouimrane, and M. Armand, "From our readers—On the electronic conductivity of phosphoolivines as lithium storage electrodes," *Nat. Mater.* **2** (2003) 702–702.

[46] P. S. Herle, B. Ellis, N. Coombs, and L. F. Nazar, "Nano-network electronic conduction in iron and nickel olivine phosphates," *Nat. Mater.* **3** (2004) 147–152.

[47] C. Delacourt, C. Wurm, L. Laffont, J. B. Leriche, and C. Masquelier, "Electrochemical and electrical properties of Nb- and/or C-containing $LiFePO_4$ composites," *Solid State Ionics* **177** (2006) 333–341.

[48] C. Delacourt, P. Poizot, J. M. Tarascon, and C. Masquelier, "The existence of a temperature-driven solid solution in Li_xFePO_4 for $0 \leq x \leq 1$," *Nat. Mater.* **4** (2005) 254–260.

[49] C. Delacourt, J. Rodriguez-Carvajal, B. Schmitt, J. M. Tarascon, and C. Masquelier, "Crystal chemistry of the olivine-type Li_xFePO_4 system ($0 \leq x \leq 1$) between 25 and 370 degrees C," *Solid State Sciences* **7** (2005) 1506–1516.

[50] A. Yamada, H. Koizumi, N. Sonoyama, and R. Kanno, "Phase change in Li_xFePO_4," *Electrochem. Solid-State Lett.* **8** (2005) A409–A413.

[51] A. Yamada, H. Koizumi, S. I. Nishimura, N. Sonoyama, R. Kanno, M. Yonemura, T. Nakamura, and Y. Kobayashi, "Room-temperature miscibility gap in Li_xFePO_4," *Nat. Mater.* **5** (2006) 357–360.

[52] N. Meethong, H.-Y. S. Huang, W. C. Carter, and Y. M. Chiang, "Size-dependent lithium miscibility gap in nanoscale $Li_{1-x}FePO_4$," *Electrochem. Solid-State Lett.* **10** (2007) A134–A138.

[53] R. L. Mössbauer, "Kernresonanzfluoreszenz von Gammastrahlung in Ir-191," *Z. Phys.* **151** (1958) 124–143.

[54] B. Fultz, "Mössbauer Spectrometry," in *Methods in Materials Research*, E. N. Kaufmann, editor, vol. Section 9c.1.1. John Wiley and Sons, 2000.

[55] D. P. E. Dickson and F. J. Berry, *Mössbauer Spectrometry*. Cambridge University Press, 1986.

[56] Y. Reynier, *Thermodynamics and kinetics of electrodes for lithium-ion batteries*. Ph.D. thesis, Institut National Polytechnique de Grenoble, 2005.

[57] J. L. Dodd, R. Yazami, and B. Fultz, "Thermostability of $LiFePO_4$," in *The Electrochemical Society Meeting Abstracts*. Honolulu, HI, 2004.

[58] R. Stevens, J. L. Dodd, M. G. Kresch, R. Yazami, B. Fultz, B. Ellis, and L. F. Nazar, "Phonons and thermodynamics of unmixed and disordered $Li_{0.6}FePO_4$," *J. Phys. Chem. B* **110** (2006) 22732–22735.

[59] F. Zhou, T. Maxisch, and G. Ceder, "Configurational electronic entropy and the phase diagram of mixed-valence oxides: The case of Li_xFePO_4," *Phys. Rev. Lett.* **97** (2006) 155704.

[60] J. L. Dodd, R. Yazami, and B. Fultz, "Phase diagram of Li_xFePO_4," *Electrochem. Solid-State Lett.* **9** (2006) A151–A155.

[61] I. Belharouak, J. Dodd, H. Tsukamoto, and K. Amine in *Extended Abstracts, 14th Int. Conf. on Solid-State Ionics*, vol. 90. Monterey, CA, 2003.

[62] C. Masquelier, P. Reale, C. Wurm, M. Morcrette, L. Dupont, and D. Larcher, "Hydrated iron phosphates $FePO_4 \cdot nH_2O$ and $Fe_4(P_2O_7)_3 \cdot nH_2O$ as 3 V positive electrodes in rechargeable lithium batteries," *J. Electrochem. Soc.* **149** (2002) A1037–A1044.

[63] I. A. Gorbunov, B. A. Maximov, I. K. Kabalov, A. N. Ivashchenko, O. K. Melnikov, and N. V. Belov, "Crystal-structure of $Fe_3(2+)Fe_4(3+)[PO_4]_6$," *Doklady Akademii Nauk Sssr* **254** (1980) 873–877.

[64] G. J. Redhammer, G. Roth, G. Tippelt, M. Bernroider, W. Lottermoser, and G. Amthauer, "The mixed-valence iron compound $Na_{0.1}Fe_7(PO_4)_6$: crystal structure and Fe-57 Mössbauer spectroscopy between 80 and 295 K," *J. Solid-State Chem.* **177** (2004) 1607–1618.

[65] J. T. Hoggins, J. S. Swinnea, and H. Steinfink, "Crystal-structure of $Fe_2P_2O_7$," *J. Solid-State Chem.* **47** (1983) 278–283.

[66] T. Stefanidis and A. G. Nord, "The crystal-structure of iron(II) diphosphate, $Fe_2P_2O_7$," *Zeitschrift Fur Kristallographie* **159** (1982) 255–264.

[67] A. Goiffon, J. C. Jumas, and E. Philippot, "Alpha-quartz type phases—Structure of $FePO_4$ and Fe-57 Mössbauer spectrometry," *Revue de Chimie Minerale* **23** (1986) 99–110.

[68] P. Reale, B. Scrosati, C. Delacourt, C. Wurm, M. Morcrette, and C. Masquelier, "Synthesis and thermal behavior of crystalline hydrated iron(III) phosphates of interest as positive electrodes in Li batteries," *Chem. Mater.* **15** (2003) 5051–5058.

[69] C. Masquelier, A. K. Padhi, K. S. Nanjundaswamy, and J. B. Goodenough, "New cathode materials for rechargeable lithium batteries: The 3-D framework structures $Li_3Fe_2(XO_4)_3$ (X = P, As)," *J. Solid-State Chem.* **135** (1998) 228–234.

[70] S. F. Yang, P. Y. Zavalij, and M. S. Whittingham, "Hydrothermal synthesis of lithium iron phosphate cathodes," *Electrochem. Comm.* **3** (2001) 505–508.

[71] A. K. Padhi, K. S. Nanjundaswamy, C. Masquelier, S. Okada, and J. B. Goodenough, "Effect of structure on the Fe^{3+}/Fe^{2+} redox couple in iron phosphates," *J. Electrochem. Soc.* **144** (1997) 1609–1613.

[72] S. Okada, S. Sawa, M. Egashira, J. Yamaki, M. Tabuchi, H. Kageyama, T. Konishi, and A. Yoshino, "Cathode properties of phospho-olivine $LiMPO_4$ for lithium secondary batteries," *J. Power Sources* **97-8** (2001) 430–432.

[73] M. Yonemura, A. Yamada, Y. Takei, N. Sonoyama, and R. Kanno, "Comparative kinetic study of olivine Li_xMPO_4 (M = Fe, Mn)," *J. Electrochem. Soc.* **151** (2004) A1352–A1356.

[74] G. H. Li, H. Azuma, and M. Tohda, "$LiMnPO_4$ as the cathode for lithium batteries," *Electrochem. Solid-State Lett.* **5** (2002) A135–A137.

[75] A. Yamada, Y. Kudo, and K. Y. Liu, "Reaction mechanism of the olivine-type $Li_x(Mn_{0.6}Fe_{0.4})PO_4$ ($0 \leq x \leq 1$)," *J. Electrochem. Soc.* **148** (2001) A747–A754.

[76] G. H. Li, H. Azuma, and M. Tohda, "Optimized $LiMn_yFe_{1-y}PO_4$ as the cathode for lithium batteries," *J. Electrochem. Soc.* **149** (2002) A743–A747.

[77] A. Yamada, M. Hosoya, S. C. Chung, Y. Kudo, K. Hinokuma, K. Y. Liu, and Y. Nishi, "Olivine-type cathodes achievements and problems," *J. Power Sources* **119** (2003) 232–238.

[78] A. Yamada, Y. Kudo, and K. Y. Liu, "Phase diagram of $Li_x(Mn_yFe_{1-y})PO_4$ ($0 \leq$ x, y ≤ 1)," *J. Electrochem. Soc.* **148** (2001) A1153–A1158.

[79] Y. Reynier, J. Graetz, T. Swan-Wood, P. Rez, R. Yazami, and B. Fultz, "Entropy of Li intercalation in Li_xCoO_2," *Phys. Rev. B* **70** (2004) 174304.

[80] G. Y. Chen, X. Y. Song, and T. J. Richardson, "Electron microscopy study of the $LiFePO_4$ to $FePO_4$ phase transition," *Electrochem. Solid-State Lett.* **9** (2006) A295–A298.

[81] T. Maxisch and G. Ceder, "Elastic properties of olivine Li_xFePO_4 from first principles," *Phys. Rev. B* **73** (2006) 174112.

[82] T. Maxisch, F. Zhou, and G. Ceder, "Ab initio study of the migration of small polarons in olivine Li_xFePO_4 and their association with lithium ions and vacancies," *Phys. Rev. B* **73** (2006) 104301.

[83] S. Q. Shi, L. J. Liu, C. Y. Ouyang, D. S. Wang, Z. X. Wang, L. Q. Chen, and X. J. Huang, "Enhancement of electronic conductivity of $LiFePO_4$ by Cr doping and its identification by first-principles calculations," *Phys. Rev. B* **68** (2003) 195108.

[84] Y. N. Xu, S. Y. Chung, J. T. Bloking, Y. M. Chiang, and W. Y. Ching, "Electronic structure and electrical conductivity of undoped $LiFePO_4$," *Electrochem. Solid-State Lett.* **7** (2004) A131–A134.

[85] B. Ellis, L. K. Perry, D. H. Ryan, and L. F. Nazar, "Small polaron hopping in Li_xFePO_4 solid solutions: Coupled lithium-ion and electron mobility," *J. Am. Chem. Soc.* **128** (2006) 11416–11422.

[86] L. R. Walker, G. K. Wertheim, and V. Jaccarino, "Interpretation of Fe^{57} isomer shift," *Phys. Rev. Lett.* **6** (1961) 98.

[87] B. D. Josephson, "Temperature-dependent shift of gamma-rays emitted by a solid," *Phys. Rev. Lett.* **4** (1960) 341–342.

[88] R. V. Pound and G. A. Rebka, "Variation with temperature of the energy of recoil-free gamma-rays from solids," *Phys. Rev. Lett.* **4** (1960) 274–275.

[89] P. P. Prosini, M. Lisi, D. Zane, and M. Pasquali, "Determination of the chemical diffusion coefficient of lithium in $LiFePO_4$," *Solid State Ionics* **148** (2002) 45–51.

[90] I. Halevy, S. Salhov, A. F. Yue, J. Hu, and I. Yaar, "High pressure study of HfNi crystallographic and electronic structure," *Hyperfine Interactions* **159** (2004) 357–362.

[91] R. Forman, G. Piermarini, J. Barnett, and S. Block, "Pressure measurement made by the utilization of ruby sharp-line luminescence," *Science* **176** (1972) 284.

[92] P. Vinet, J. Ferrante, J. H. Rose, and J. R. Smith, "Compressibility of Solids," *J. of Geophys. Res.* **92** (1987) 9319–9325.